

ASSEMBLY, ELASTICITY, AND STRUCTURE OF LYOTROPIC CHROMONIC  
LIQUID CRYSTALS AND DISORDERED COLLOIDS

Zoey S. Davidson

A DISSERTATION

in

Physics and Astronomy

Presented to the Faculties of the University of Pennsylvania

in

Partial Fulfillment of the Requirements for the

Degree of Doctor of Philosophy

2017

Supervisor of Dissertation

---

Arjun G. Yodh, Professor of Physics and Astronomy

Graduate Group Chairperson

---

Ravi K. Sheth, Professor of Physics and Astronomy

Dissertation Committee

Tom C. Lubensky, Professor of Physics and Astronomy

Peter J. Collings, Professor of Physics and Astronomy

Douglas J. Durian, Professor of Physics and Astronomy

Joel S. Karp, Professor of Physics and Astronomy

ASSEMBLY, ELASTICITY, AND STRUCTURE OF LYOTROPIC CHROMONIC  
LIQUID CRYSTALS AND DISORDERED COLLOIDS

COPYRIGHT

2017

Zoey S. Davidson

*For Simone and Steven.*

# Acknowledgments

I am indebted to many people who have contributed to my graduate education and this resulting dissertation.

For his expert guidance, attention to detail, passion for physics, and warm friendship, I am *extremely* grateful to my advisor, Arjun Yodh. From his coaching me through practice talks to careful and abundant edits of my writing, I have learned much about science and science communication. His interest in diverse problems, applied and fundamental, inspires my pursuits in physics and beyond.

I have worked with amazingly talented theoretical and experimental collaborators without whom my research would not have been possible. They include Peter Collings, Matt Gratale, Adam Gross, Joonwoo Jeong, Randall Kamien, Louis Kang, Matt Lohr, Tom Lubensky, Xiaoguang Ma, Angel Martinez, Tim Still, and Chao Zhou. Among the many other students, theorists, and experimentalists I have learned much from are Blandine Barabé, Dan Beller, Jing Cai, Toen Castle, Anthony Chieco, Kevin Chiou, Alexis de la Cotte, Carl Goodrich, Analisa Hill, Martin Haase, François Landes, Max Lavrentovich, Jiachen Liu, Sam Lobel, Ricardo Mosna, Sam Schoenholz, Francesca Serra, Daniel Sussman, Lisa Tran, Fuquan Tu, Weishao Wei, Ye Xu, Jiajia Yu, and Xia Yu.

The Physics Department at Penn has been my second home for more than a decade. There have been many excellent teachers, mentors, and classmates who have helped me to this point in my research career. Joel Karp and his lab members, especially, Rony Wiener, Madhuri Kaul, and Aaron Aguilar were essential to my development from undergraduate physics major to graduate researcher. Bill Ashmanskas has been exemplary as both teacher

and student of physics. To the many students I had a chance to both teach and learn to teach – thank you! I must thank my fellow physics “first-years”, I could not have asked for better comrades in graduate school: John Briguglio, Jeff Cochran, Louis Kang, Sergey Nisnevich, Mehmet Noyan, Madeleine Phillips, Kevin Tian, Davis Varghese, and Rachel Wolf. Support from the administrative staff, including Dorothea Coleman, Raymond Hsiao, Millicent Minnick, and Enrique Vargas has been unwavering.

Finally, my friends and family – especially my parents – have been patient, loving, and supportive beyond all reasonable expectations. Thank you!

## ABSTRACT

### ASSEMBLY, ELASTICITY, AND STRUCTURE OF LYOTROPIC CHROMONIC LIQUID CRYSTALS AND DISORDERED COLLOIDS

Zoey S. Davidson

Arjun G. Yodh

This dissertation describes experiments which explore the structure and dynamics in two classes of soft materials: lyotropic chromonic liquid crystals and colloidal glasses and super-cooled liquids.

The first experiments found that the achiral LCLCs, sunset yellow FCF (SSY) and disodium cromoglycate (DSCG) both exhibit spontaneous mirror symmetry breaking in the nematic phase driven by a giant elastic anisotropy of their twist modulus compared to their splay and bend moduli. Resulting structures of the confined LCLCs display interesting director configurations due to interplay of topologically required defects and twisted director fields. At higher concentrations, the LCLC compounds form columnar phases. We studied the columnar phase confined within spherical drops and discovered and understood configurations of the LC that sometimes led to non-spherical droplet shapes. The second experiments with SSY LCLCs confined in hollow cylinders uncovered director configurations which were driven in large measure by an exotic elastic modulus known as saddle-splay. We measured this saddle-splay modulus in a LCLC for the first time and found it to be more than 50 times greater than the twist elastic modulus. This large relative value of the saddle-splay modulus violates a theoretical result/assumption known as the Ericksen inequality.

A third group of experiments on LCLCs explored the drying process of sessile drops containing SSY solutions, including evaporation dynamics, morphology, and deposition patterns. These drops differ from typical, well-studied evaporating colloidal drops primarily due to the LCLC's concentration-dependent isotropic, nematic, and columnar phases. Phase separation occurs during evaporation, creating surface tension gradients and significant den-

sity and viscosity variation within the droplet. Thus, the drying multiphase drops exhibit new convective currents, drop morphologies, deposition patterns, as well as a novel ordered crystalline phase.

Finally, experiments in colloidal glasses and super-cooled liquids were initiated to probe the relationship between structure and dynamics in their constituent particles. The displacements of individual particles in the colloids can be decomposed into small cage fluctuations and large rearrangements into new cages. We found a correlation between the rate of rearrangement and the local cage structure associated with each particle. Particle trajectories of a two-dimensional binary mixture of soft colloids are captured by video microscopy. We use a machine learning method to calculate particle “softness”, which indicates the likelihood of rearrangement based on many radial structural features for each particle. We measured the residence time between consecutive rearrangements and related probability distribution functions (PDFs). The softness-dependent conditional PDF is well fit by an exponential with decay time decreasing monotonically with increasing softness. Using these data and a simple thermal activation model, we determined activation energies for rearrangements.

# Contents

<b>1</b>	<b>Introduction</b>	<b>1</b>
1.1	Lyotropic chromonic liquid crystals . . . . .	2
1.2	Disordered colloidal glasses . . . . .	8
1.3	Outline of subsequent chapters . . . . .	10
<b>2</b>	<b>Chiral structures of achiral liquid crystals in spherical and cylindrical confinement geometries</b>	<b>11</b>
2.1	Introduction . . . . .	11
2.2	Jones Matrix Methods for Analyzing Director Configurations . . . . .	13
2.2.1	Python Code for Producing Jones Matrix Images . . . . .	14
2.3	Spherical Droplet Confinement with Planar Anchoring . . . . .	14
2.3.1	Preparation of LCLC-in-oil emulsion . . . . .	16
2.3.2	Energetics of Droplet Confined Director Configurations . . . . .	18
2.3.3	Faceted Columnar Phase Droplets . . . . .	24
2.3.4	Double Emulsions of LCLC with DSCG . . . . .	27
2.3.5	Summary of LCLC Droplet Results . . . . .	29
2.4	Cylindrical Confinement with Homeotropic Anchoring . . . . .	30
2.4.1	Preparation of Capillaries with Homeotropic Anchoring . . . . .	31
2.4.2	Mirror Symmetry Breaking and the Twisted-Escaped Radial Configuration . . . . .	32
2.4.3	Topological Defects of the Twisted-Escaped Radial Configuration . . . . .	37
2.4.4	Twisted Helical Configuration . . . . .	44
2.5	Conclusions and Future Work . . . . .	46
2.6	Appendix: Numerical Calculation of Elastic Free Energy In Droplets . . . . .	47
<b>3</b>	<b>Chiral Structures and Defects of Lyotropic Chromonic Liquid Crystals Induced by Saddle-Splay Elasticity</b>	<b>50</b>
3.1	Introduction . . . . .	50
3.2	Theoretical Background of Frank Elastic Free Energy and Saddle-Splay . . . . .	52

3.3	Experimental Methods of Measuring Escaped-Twisted Configuration . . . .	56
3.3.1	Observations of Director Fluctuations to Measure Director Configuration . . . . .	58
3.3.2	Calculation of $K_{24}$ and its Error Bar . . . . .	61
3.4	Defects in Escaped-Twisted Configuration . . . . .	64
3.5	A Possible Chemical Anchoring Effect Mimicking Saddle-Splay . . . . .	65
3.6	Conclusion . . . . .	67
<b>4</b>	<b>Deposition and Drying Dynamics of Liquid Crystal Droplets</b>	<b>69</b>
4.1	Introduction . . . . .	69
4.2	Materials and Methods . . . . .	70
4.3	Results and Discussion . . . . .	72
<b>5</b>	<b>A Machine Learning Investigation of Structure and Dynamics of Soft Colloidal Glasses</b>	<b>85</b>
5.1	Introduction . . . . .	85
5.2	Materials and Methods . . . . .	87
5.2.1	Classifying Stable and Rearranging Particles . . . . .	87
5.2.2	Machine Learning Details . . . . .	89
5.3	Results . . . . .	93
5.3.1	Interpreting Cage Structure-Softness Relationship . . . . .	99
5.4	Discussion . . . . .	101
<b>6</b>	<b>Summary and Future Directions</b>	<b>102</b>
6.1	Lyotropic Chromonic Liquid Crystals . . . . .	102
6.1.1	Surface Chemistry and Elastic Effects . . . . .	104
6.1.2	Origins of Giant Elastic Anisotropy . . . . .	105
6.1.3	LCLC Mesogen Structure Near Defects . . . . .	106
6.1.4	LCLC Optical Guiding . . . . .	107
6.2	Summary of and Future Experiments with Disordered Colloidal Glasses . .	107
6.2.1	Bridging Softness and Ensemble Properties in Disordered Colloidal Glasses . . . . .	108
6.2.2	Predicting Fracture in Sheared or Thermally Shocked Colloidal Glass	109

# List of Tables

1.1	Frank elastic modulus values of two common lyotropic chromonic liquid crystals and a typical thermotropic liquid crystal (TLC). . . . .	4
3.1	NLLS fit parameters and uncertainty from five independent flickering measurements. Upper and lower bounds reflect refitting after replacing $R$ by $R + 400$ nm and $R - 400$ nm, respectively. . . . .	62

# List of Figures

1.1	Molecules of Sunset Yellow FCF, disodium cromoglycate, and 4-cyano-4'-pentylbiphenyl . . . . .	5
1.2	Temperature and Concentration phase diagram of Sunset Yellow . . . . .	5
1.3	Assembly and deformation modes of lyotropic chromonic liquid crystals . . . . .	7
2.1	Optical microscopy images of a nematic LCLC droplet and Jones matrix calculations of the patterns in droplets between crossed polarizers. . . . .	17
2.2	Polarized Optical Microscopy (POM) images and transmitted intensity through LCLC droplet centers. . . . .	19
2.3	Polarized Optical Microscopy (POM) images and transmitted intensity through LCLC droplet centers. . . . .	23
2.4	Optical microscopy images of a columnar LCLC droplet and Jones matrix calculations of light patterns after passing through a droplet located between crossed polarizers. . . . .	25
2.5	Bright-field microscopy images of columnar LCLC droplets with facets and schematic diagrams of the Wulff construction of faceted droplets. . . . .	26
2.6	Double emulsion drops of disodium cromoglycate (DSCG) in the nematic phase. . . . .	28
2.7	Double emulsion drops of DSCG in the columnar phase. . . . .	29
2.8	Optical microscopy images and simulated patterns of nematic SSY in a cylinder between crossed polarizers with and without a full-wave plate. . . . .	34
2.9	A Twisted and Escaped Radial (TER) director configuration. . . . .	35
2.10	Optical microscopy (bright-field and POM) images of defects and simulated patterns of corresponding defects that arise when nematic SSY is placed in the cylinder. . . . .	38
2.11	Chirality of nematic SSY defects in a cylinder with TER director configuration. . . . .	39
2.12	Energetics of the chiral defects in TER director configuration. . . . .	42
2.13	Schematic diagrams of the radial and hyperbolic defect configurations of homochirality and heterochirality near the defect plane. . . . .	43
2.14	POM images of nematic SSY with a double helix of disclinations in a cylinder under polychromatic illumination. . . . .	44
2.15	POM images of nematic SSY with a double helix of disclinations in a cylinder under polychromatic illumination. . . . .	45
3.1	Coordinate system and director field diagram of escaped-twisted configuration . . . . .	53
3.2	Escaped-twisted phase diagram parameterized by elastic moduli ratios . . . . .	57

3.3	Measurement of director fluctuations in escaped-twisted configuration . . .	59
3.4	Defects and defect energetics in the escaped-twisted director configuration .	63
3.5	Scanning electron and atomic force microscopy of a broken glass capillary. .	66
3.6	Silane treated capillary with planar anchoring has an apparent lesser total twist angle. . . . .	67
4.1	A drying droplet of Sunset Yellow FCF (SSY) on a coverslip under ambient room conditions and with initial concentration of 15% by weight. . . . .	73
4.2	The drying progression of SSY droplets imaged by UHR-OCM. . . . .	74
4.3	The moving isotropic-nematic phase boundary of SSY, nematic tactoids nucleate in the biphasic bulk fluid region near the interface. . . . .	78
4.4	A drying drop of SSY on a glass slide initially with 15 % concentration by weight forms a ring of nematic phase near the contact line with director alignment tangential to the contact line. . . . .	79
4.5	An enclosed drying LCLC droplet with initial concentration of 15% SSY by weight on a glass slide is in the columnar phase near the drop edge . . . . .	80
4.6	Slowly dried drops of SSY on a glass slide show coarsening of the columnar phase as the concentration increases. . . . .	81
4.7	Profilometry results of dried droplets with varying initial weight concentrations of SSY and scanning electron microscope image of a droplet of SSY on a coverslip dried in ambient conditions. . . . .	83
5.1	Mean square displacements and self-overlap function of large and small particle species. . . . .	88
5.2	Poly(N-isopropyl acrylamide) particle trajectory and its corresponding $P_{\text{Hop}}$ values. . . . .	90
5.3	Description of support vector machine (SVM) method. . . . .	92
5.4	Distributions of residence times, softness, and residence times conditioned on softness. . . . .	94
5.5	Average particle residence times versus average softness of corresponding particle during residence time. . . . .	95
5.6	Explanation of Kramers reaction rate theory and measurement of average caging potential due to neighboring particles. . . . .	96
5.7	Local activation energy versus softness. . . . .	98
5.8	Structure features for extreme values of softness. . . . .	100

# Chapter 1

## Introduction

Between the cosmos and the subatomic lies our messy everyday world. Most biology and technology operate near room temperature and thus either fluctuate about, or are far from, equilibrium. Soft matter physics endeavors to bridge this gap between equilibrium and out-of-equilibrium physics by building understanding of highly complex systems through reductionist physical principles. Two notable examples of this include liquid crystal systems and disordered solid materials. In the former case, a purely mathematical model considering the symmetry of the underlying constituents predicts much of the physics that forms the basis a major industry (liquid crystal displays). In the latter case, the language and physics of ordered crystalline systems has gone a long way toward explaining the mechanics and failure mechanisms of disordered solids that one regularly encounters in one's daily life, though more remains! In both cases, new experiments and their findings continue to push the boundaries of the fundamental physics explanations and the technological capabilities of these and other materials studied by soft matter physicists.

My dissertation expands our knowledge of liquid crystals and disordered colloidal systems through novel experiments and analysis techniques that elucidate explanations of their interesting properties. The bulk of my dissertation is comprised of experiments that investigate the properties of lyotropic chromonic liquid crystals, including their elasticity, their self-assembly into oriented phases, and their behavior in evaporating drops [1–3]. These

experiments reveal new aspects of the rather unusual behavior of a unique type of liquid crystal: lyotropic chromonic liquid crystals. Its elastic properties frequently result in mirror symmetry breaking within the mesoscopic structures it forms. The drying dynamics and deposition character of lyotropic chromonic liquid crystal solutions also demonstrates interesting Marangoni flows, phase behavior, and dried structures by building on the classic “coffee ring” experiments. A smaller fraction of my thesis accomplishments concern recent experiments that probe rearrangements and structure in colloidal glasses, especially their analysis by machine learning methods. This new analysis technique begins to answer some open fundamental questions about glasses by establishing a relationship between the structure and the dynamics of the constituents (particles) in glassy materials.

In addition to the work explicitly discussed in this dissertation, I was fortunate to collaborate and contribute to other projects led by my talented fellow group members. Two of those published works focused on the vibrational properties of colloidal gels and glasses with varying levels of attraction [4, 5]. In the latter case, I also conducted an independent study characterizing the depletion-induced attraction forces due to cylindrically shaped surfactant micelles [6]. In yet another paper, I created and studied the properties of a new type of thermoresponsive porous membrane made from soft colloids in drying drops [7].

Finally, I have initiated and worked on several other projects that are not as yet ready for publication. This research includes depletion effects and liquid crystal phases of anisotropic colloids, application of machine learning analysis to colloidal particle packings during shear, and analysis of the fluctuations in liquid crystals near defects.

The remainder of this introductory chapter will introduce the primary topics to be discussed in this thesis and related experiments. The chapter concludes with an outline of the subsequent chapters of this dissertation.

## **1.1 Lyotropic chromonic liquid crystals**

Liquid crystals are phases of matter that exhibit properties associated with both liquids and crystals. This mixture of properties results from the order and underlying symmetries

in the constituents comprising these materials. Of particular interest in this dissertation are the nematic and columnar liquid crystal phases. In the nematic liquid crystal phase, the constituents, known as mesogens, are anisotropic in shape<sup>1</sup>. In the nematic phase, these rod-like mesogens are orientationally ordered/aligned along a “director” axis over large distances within the sample, but the mesogens exhibit translational disorder, *i.e.*, they lack the spatial periodicity found in crystals [8]. The nematic liquid crystal is a viscous liquid that flows and conforms to the shape of its container. The columnar liquid crystal phase is slightly more ordered than the nematic phase. The cylinder-like mesogens stack up to form flexible columns, and the liquid phase is comprised of many such columns packed together. The columnar phase will also conform to the shape of its container; however, it is typically more viscous than a nematic phase, and in addition to orientational order, the columns exhibit periodic spatial order in two dimensions [9]. Typically, the columnar phase is composed of columns of the mesogens arranged in a triangular lattice.

Applications of liquid crystal materials are likely to be far more numerous than the electronic displays with which they are most closely associated with today [10]. While the liquid crystal field originated from studies of a common biological molecule over a century ago [11], the majority work in the field has focused on synthetic-oil based molecules called thermotropic liquid crystals (TLC), which are generally biologically incompatible. The comparatively less studied aqueous lyotropic liquid crystals are particularly attractive as simple models (especially colloidal rods) that permit rigorous testing of theory among other surprises[12–16], and they have also generated some recent interest for their potential for creating patterned structures with a diverse range of liquid crystal phases near room temperature [17, 18]. This thesis is largely concerned with a yet less studied system, lyotropic chromonic liquid crystals (LCLCs), which are less studied among lyotropic systems and, as a class, tend to exhibit unusual properties not typically found in TLC or the other lyotropic phases of rods or amphiphilic molecules that produce liquid crystal phases [19]. For example, one particularly striking feature of the LCLC nematic phases is the large difference in

---

<sup>1</sup>They are often approximated as prolate spheroids or cylinders.

Table 1.1: Bulk and saddle-splay elastic moduli of Sunset Yellow FCF (SSY), disodium cromoglycate (DSCG) and of 4-cyano-4'-pentylbiphenyl (5CB), a typical thermotropic liquid crystal (TLC).

LC	$K_1$ [pN]	$K_2$ [pN]	$K_3$ [pN]	$K_{24}$ [pN]	Reference
SSY	8.1	0.8	8.7	57.4	[20]
DSCG	10.2	0.7	24.9	169	[21, 31]
5CB	5.2	2.9	6.8	$\sim 2.9$	[32, 33]

their splay, bend and twist elastic moduli [20]. The elastic moduli in thermotropic nematics tend to all be nearly equal; however, LCLC nematics have a ratio between their twist modulus and splay or bend moduli of ten or greater [20, 21]. Moreover, because the overall magnitudes of the moduli are similar to many thermotropics, it is not clear if the large ratio is because the twist modulus is so small or the splay and bend modulus are so great. The origin of these differences in twist versus splay/bend moduli are not well understood but are common to other polymer and lyotropic liquid crystals [22–24].

Much of my work in this thesis explores the structure (director configurations) of liquid crystals in confined geometries. Generally, the director configurations of confined liquid crystals reveal fundamental physics due to a delicate interplay of topology, elastic free energy, and interfacial anchoring conditions. Spherical droplets, for example, offer a simple and highly symmetric confining container for liquid crystals. Droplets of TLCs and corresponding manipulation of their director configurations are actively studied in part because of their demonstrated value in display technologies and other applications ranging from biosensors to microlasers [25–27]. Likewise, TLCs in hollow cylinders have exhibited a broad range of fundamental effects and have made it to the table as a possible component in fiber optic communications technology [28–30]. Significant fundamental and technological progress has been made with TLCs confined to droplets and cylinders in part because their bulk elasticity and surface anchoring phenomena are now well understood and easily controlled. The behaviors of LCLCs in droplets and cylinders (and even in rectangular structures) are far less studied than those of TLCs.

LCLCs are composed of plank-like organic salt molecules that self-assemble in water

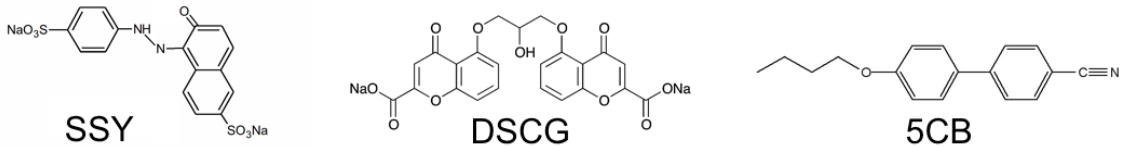


Figure 1.1: Molecules of Sunset Yellow FCF (SSY), disodium cromoglycate (DSCG), and 4-cyano-4'-pentylbiphenyl (5CB).

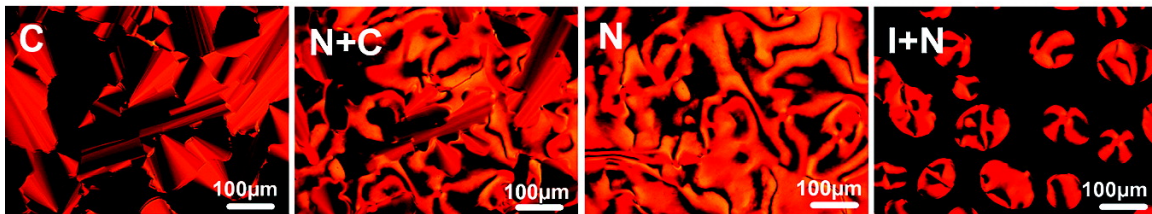
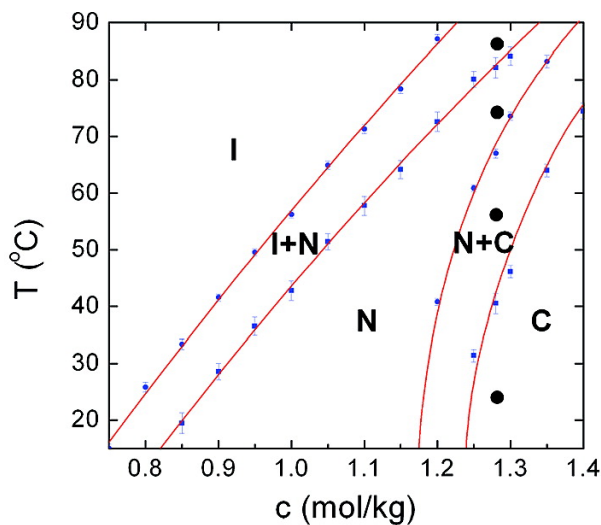


Figure 1.2: Phase diagram and polarizing microscope textures of SSY water solutions. The error bars represent the difference between the data taken on heating (upper end of the bar) and cooling (lower end of the bar). The filled circles at the vertical line indicate the temperatures at which the textures were taken. Reprinted with permission from H.-S. Park, S.-W. Kang, L. Tortora, Y. Nastishin, D. Finotello, S. Kumar, and O. D. Lavrentovich, *J. Phys. Chem. B* 112, 16307 (2008). Copyright (2008) American Chemical Society.

into column-like assemblies via noncovalent electrostatic, excluded volume, hydrophobic, and  $\pi - \pi$  stacking interactions. As noted above, these macromolecular assemblies, in turn, form the mesogens of nematic or columnar phases. The phase behavior thus depends on both temperature and concentration as in Fig. 1.2. A variety of organic molecules such as dyes, drugs, and biomolecules form LCLCs [34–37]. Other basic properties of LCLCs, including aggregate size distribution and formation dynamics, bulk elasticity, and surface anchoring are neither fully characterized nor understood and are the subject of exciting ongoing research [21, 38–40]. Only recently, for example, have measurements of fundamental properties, such as the Frank-Oseen elastic constants, been made, and even these studies were only carried out in two LCLCs: Sunset Yellow FCF (SSY) and disodium cromoglycate (DSCG) [20, 21]. Nevertheless, these investigations revealed unusual concentration and temperature dependences of the splay and bend moduli, as well as a twist modulus that is unusually small compared with the other two. The LCLC experiments I report herein were all carried out with SSY.

In **Chapter 2**, I will present the results of experiments that explore the elastic anisotropy of LCLCs, and its consequences for structure, when the nematic phase is confined to spherical and cylindrical containers. Interestingly, although the primary chromonic molecules, and mesogens they form, are themselves achiral, the small twist elastic modulus of the LCLCs promotes formation of twisted structures, which are necessarily chiral. In spherical confinement, the LCLC forms a highly twisted bipolar structure; through a diameter halfway between its poles, the director rotates more than  $180^\circ$ . In a cylindrical capillary with homeotropic anchoring, the director forms a twisted escaped radial configuration; the director has a twist handedness as it bends towards the capillary axis from the confining wall. The LCLC chiral degeneracy, lack of a preferred handedness, produces new kinds of energetically preferred defect structures when domains of opposite handedness meet. Finally, in agreement with experiment, I present numerical simulations that find a twisted helical configuration as the ground state structure of the LCLC confined to a cylinder with homeotropic anchoring.

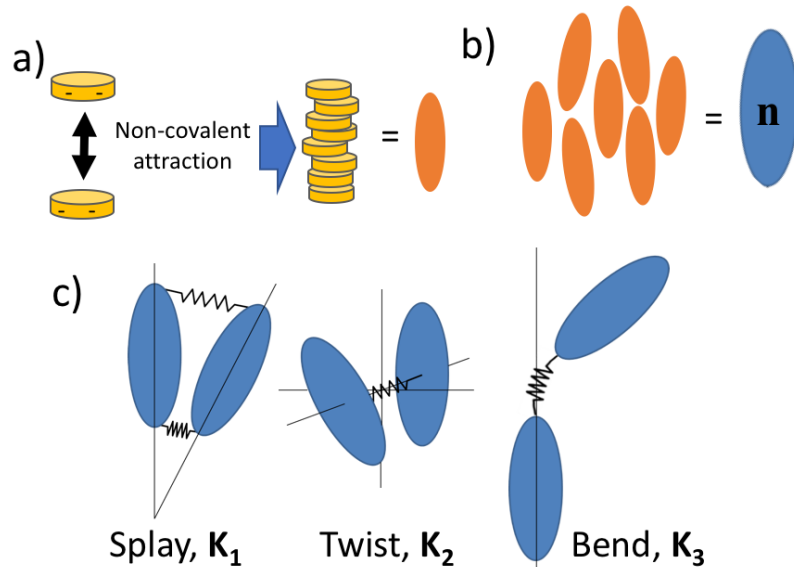


Figure 1.3: (a) Lyotropic chromonic liquid crystals (LCLC), such as Sunset Yellow FCF, form from assemblies of charged molecules (yellow disks) which become the mesogens of the nematic phase (orange ellipses). (b) The orientations of these mesogens are coarse grained to form the director field  $\mathbf{n}$  (blue ellipsoids). (c) Geometric constraints may impose deformations on the LCLC director field. These deformations can be broken into the three “typical” elastic deformations of splay ( $K_1$ ), twist ( $K_2$ ) and bend ( $K_3$ ).

**Chapter 3** presents measurements and consequences of the saddle-splay modulus,  $K_{24}$ , in SSY. The measurements are carried out in the cylindrical cavities with planar boundary conditions. The simplest configuration for this type of situation is one where the director is uniformly parallel to the cylinder axis throughout the cavity. This is not what I observe. The measurements reveal that surface elastic forces (mimicking saddle-splay) can promote a deformed ground state. This result further suggests that the common zero deformation ground state assumption underlying the so-called “Ericksen inequalities” may not always be appropriate. Briefly, Ericksen made the assumption that a stable ground state of a nematic LC would have zero deformation, and this assumption predicted an upper bound for the saddle-splay modulus, *i.e.*, the saddle-splay modulus is twice the twist modulus (or less) in a nematic LC. In this chapter, I discuss the effects of the saddle-splay modulus on the cylindrically confined LCLC and introduce the methods for measuring it in SSY. I thus measured the value of  $K_{24}$  in a LCLC for the first time, which revealed that its ratio to

the twist and bend moduli violates the Ericksen inequality. I will also further discuss the possible existence of a chemical surface interaction that mimics the effects of a large saddle-splay modulus, and I will describe preliminary attempts to discern the impact of chemical effects on the measurements of  $K_{24}$ .

SSY forms LCLC phases in water. This fact suggested a qualitatively different and novel study with LCLCs. Specifically, the SSY solutions offer the possibility to investigate the deposition of an anisotropic, LC-forming material during droplet evaporation. In **Chapter 4**, I discuss these experiments. In particular, I describe processes and unique phenomena that occur during the evaporation of SSY solutions. Within drying drops, different phases form in different regions of the drying drop, and unusual Marangoni flows arise due to concentration gradients and the resulting surface tension gradients. Among other things, these studies of the SSY drying process showed that surface tension increased with increasing SSY concentration. Furthermore, I observed an ordered yet hydrated crystalline phase that appears at higher concentrations than that of the columnar phase. The intermediate crystalline phase leads to domain walls and visual textures within the drying LCLC drop that appear similar to a columnar phase. My characterization of the whole process takes the study of coffee-rings beyond the realm of simple colloids.

The results noted above suggest and inform future work on lyotropic chromonic liquid crystals, including applications. For example, recent research has demonstrated the ability to make anisotropic elastic hydrogels from modified DSCG molecules and other chromonic mesogens. Combining these new mesogens and the confinement effects described in this dissertation may result in novel and useful colloidal structures and materials. In the concluding **Chapter 6**, I will discuss some preliminary experiments along these lines, as well as possible new avenues of research for LCLCs.

## 1.2 Disordered colloidal glasses

The structural properties and failure mechanisms of glasses are of immense interest to materials scientists, and the underlying physics of the characteristics common to disordered

systems of atomic, molecular, polymer, and colloidal glasses remains elusive [41, 42]. Of particular interest in this context are the constituent dynamics in glasses and in their super-cooled liquid precursors. Though mean field theory, which assumes uniform local structure, captures some characteristic features of glassy dynamics, the relationship between structure and dynamics is not understood [43, 44]. The liquid-to-solid transition in glassy materials shows barely discernible changes in constituent structure, unlike crystallization. Furthermore, glassy solids have not been found to exhibit flow and premelting associated with structural defects as in crystalline solids [41, 42].

Localized particle rearrangements have been observed in glassy materials (in experiment and simulation) and are associated with applied stress and temperature increases [45–47]. It has been suggested these rearrangement sites are similar to the structural defects in crystals that promote flow and premelting [48–50]. Studies of localized dynamics of rearrangement sites have revealed connections between low-frequency vibrational modes and localized flow [51–54], and indirect correlations between local structure and dynamics of super-cooled liquids have been established in a few cases [55, 56]. However, only recently has there been success in identifying robust structural features that promote localized rearrangement sites [57, 58]. Using a new scalar field called “softness” derived from a machine learning approach, localized structures in glassy systems can be correlated with localized dynamics.

Studies of model colloidal systems have revealed a great deal about traditional atomic and molecular materials. For example, colloidal particles as model atoms are small enough to undergo Brownian motion yet large enough to track with optical microscopy. The colloidal suspensions used in this work are soft materials composed of poly(N-isopropylacrylamide) (PNIPAM) hydrogel particles suspended in water [59]. These soft colloids serve as a model system to answer the above fundamental questions about super-cooled liquids and glassy solids. Within a single sample most particles tend to spend the majority of the time within a cage created by neighboring particles. However, rearrangements such as cage-breaking motions occur over a large range of time and length scales. **Chapter 5** describes initial investigations into the phenomena; in particular, I use machine learning methods to

characterize the local structure of particles in an aqueous suspension of a glassy colloidal monolayer, and then to connect the heterogeneity of time and length scales in the localized dynamics of disordered colloidal packings to local structure. I find that, indeed, cage structure is predictive of particle dynamics; cage rearrangements follow Arrhenius behavior when conditioned on structure. This suggests further experiments may be able to predict failure locations in sheared glassy colloidal systems like flow defects and premelting in crystalline materials.

### 1.3 Outline of subsequent chapters

The remainder of this thesis is organized as follows. In **Chapter 2**, I examine the combined effects of confinement and the giant anisotropy of the elastic deformation modes in nematic liquid crystals in spherical and cylindrical containers. In the case of spherical confinement, I also examine the columnar phase and the effect confining surface tension has on the structures. **Chapter 3** further examines the role of confinement in LCLC structures with the added effect of surface forces mimicking saddle-splay. In this case, the boundary conditions and cylindrical geometry make the role of saddle-splay surface elasticity explicit and readily enables its measurement. **Chapter 4** presents a series of LCLC solution evaporation and deposition (coffee-ring) experiments. **Chapter 5** introduces an analysis procedure using machine learning to study structural and dynamic properties of colloidal glasses. This procedure, originally developed for analysis of simulations of glasses and super cooled liquids, makes significant headway towards answering open questions about rearrangements and structure in glasses and super-cooled liquids. Finally, in the short **Chapter 6**, I summarize the primary observations of my thesis and suggest future studies to explore open questions concerning, for example, details of the assembly of LCLCs and the rearrangement dynamics in colloidal glasses.

## Chapter 2

# Chiral structures of achiral liquid crystals in spherical and cylindrical confinement geometries<sup>1</sup>

### 2.1 Introduction

The emergence of chirality from achiral systems poses fundamental questions about which we have limited mechanistic understanding [60–71]. A handedness is established when the achiral (mirror) symmetry of a system is broken, and such materials with particular handedness commonly exhibit distinct and useful properties [63, 70–73] that have proven relevant for applications ranging from chemical sensors [26, 74, 75] to photonics [76–78]. Thus considerable effort has been expended to control handedness in materials to date, for example, by chiral separation of racemic mixtures or chiral amplification of small enantiomeric imbalances [60, 69, 79–81]. Recently, and in a different vein, identification and elucidation of pathways by which achiral building blocks spontaneously organize to create chiral structures has become an area of active study. Examples of these pathways include packing with multiple competing length scales [66, 69, 70, 82, 83], reconfiguration via mechanical insta-

---

<sup>1</sup>This chapter is adapted from references [1] and [2].

bilities of periodic structures [79, 84, 85], and helix formation of flexible cylinders via inter- and intra-cylinder interactions [86, 87]. In addition, systems with broken mirror symmetry often consist of domains of matter with opposite handedness, and therefore these systems give rise to novel defects that separate different chiral domains.

Liquid crystals (LCs) are soft materials composed of anisotropic mesogens that provide remarkable examples of mirror symmetry breaking arising from elastic anisotropy [1, 88–99]. In essence, it is possible for a LC to minimize elastic free energy by organizing its achiral units into chiral structures such as helices and chiral layers that incorporate twist deformation [68, 69]. The elastic free energy describing nematic liquid crystal deformations depends on so-called splay, twist, bend and saddle-splay elastic moduli, and when twist deformation is comparatively easy, twisting can relieve strong splay and/or bend deformation and lead to production of equilibrium chiral structures [88, 92–95, 100]. Similarly, saddle-splay deformation can stabilize chiral structures [101–103].

Elasticity-driven mirror symmetry breaking is perhaps most readily manifested in *confined* LCs [1, 90–99, 101], wherein surface anchoring imposes a preferred angle for LC mesogens at the interface of the confining container boundary. Topological defects enforced by boundary conditions can play a key role in the symmetry breaking too, because energetically costly deformations are often concentrated in the vicinity of the defects [1, 94, 95]. A simple example of this phenomenon is found in spherical LC droplets with planar anchoring; here two surface point defects, called Boojums, cause the director to adopt a twisted bipolar configuration in which energetically cheap twist deformations relieve strong splay deformations near the Boojums.

In this thesis, we study mirror-symmetry-broken configurations of nematic LCs confined to spherical droplets with planar anchoring and confined to cylindrical capillaries with homeotropic anchoring (*i.e.*, perpendicular surface alignment) on the cylinder walls. Interestingly, *achiral* nematic LCs with comparatively small twist elastic moduli relieve bend and splay deformations by introducing *twist deformations*. In the resulting twisted-bipolar droplets and twisted- and escaped-radial (TER) configurations in cylinders, the LC director

configuration reduces splay and bend distortions via introduction of significant twist distortions. While the nematic director configurations of LCs confined within droplets [104] and cylinders [105] has been explored previously, the present experiments re-examine this phenomenology using a much less common liquid crystal material that twists very easily, *i.e.*, lyotropic chromonic liquid crystals.

Lyotropic chromonic liquid crystals (LCLCs) are composed of organic, charged, and plank-like mesogens that self-assemble/disassemble in water into columnar aggregates via non-covalent electrostatic, excluded volume, hydrophobic, and  $\pi$ - $\pi$  stacking interactions.[10, 36, 37, 106] The aggregates, in turn, assemble into nematic or columnar phases, depending on temperature and concentration. A variety of organic molecules such as dyes, drugs, and biomolecules form LCLCs [10, 34, 36–38, 106–111]. Far less is known about the fundamental science and applications potential of LCLCs than the more studied thermotropic liquid crystals (TLCs) that are the basis of commercial display technologies. Indeed, many basic properties of LCLCs, including aggregate size distribution and formation dynamics, bulk elasticity, and surface anchoring, are neither fully characterized nor understood and are the subject of exciting ongoing research. Only recently, for example, have measurements been made of fundamental properties, such as the Frank-Oseen elastic constants [20, 112], of any LCLC, and these measurements have revealed unusual concentration and temperature dependences of the splay and bend moduli and a twist modulus that is unusually small compared to the other two.

## 2.2 Jones Matrix Methods for Analyzing Director Configurations

In order to characterize the director configurations in the droplets and capillaries, polarization optical microscopy (POM) images of samples under monochromatic illumination must be compared to simulations of polarized light transport through simulated samples (and polarizers). The well-known method to carry out this comparison uses so-called Jones cal-

culus with  $2 \times 2$  matrices [113, 114]. This approach permits computation of the change to light polarization and transmission as it traverses the sample and the other optical elements in its path.

Specifically, in our case, the volume of a “simulated” LCLC droplet or capillary was divided into volume elements (voxels) on a three-dimensional grid, and the LC director orientation was assigned to each voxel. In practice, the LC director was computed from a 3D director field model in the case of droplets [104, 114, 115], or using numerically calculated configurations in the case of cylinders [116]. A Jones matrix for each voxel was calculated using the LCLC’s known (or estimated) ordinary and extraordinary indices of refraction at the wavelength of the illumination light. Then, simulated plane waves were projected through the input polarizer, through the simulated sample, and through the analyzer; corresponding Jones matrices of the optical components and the voxels along the beam path were multiplied sequentially to derive an exit Jones vector at each pixel. The squared norms of the exit Jones vectors represent the transmitted intensities at each pixel and comprise a 2D intensity profile of the transmitted light. This profile was then compared to observation. Note that for this calculation, the effects of refraction, reflection, and diffraction by the interfaces are assumed to be negligible; it is known that this approximate calculation produces reasonable simulations for large confinement volumes with modest birefringence [104].

### **2.2.1 Python Code for Producing Jones Matrix Images**

An implementation in Python of the Jones calculus method is included in the supplemental information of this dissertation.

## **2.3 Spherical Droplet Confinement with Planar Anchoring**

Confined liquid crystals (LC) provide a unique platform for technological applications and for study of LC properties, such as bulk elasticity, surface anchoring, and topological defects. In our work, lyotropic chromonic liquid crystals (LCLCs) are confined in spherical droplets

and cylindrical capillaries, and their director configurations are investigated using bright-field and polarized optical microscopy. As a result of the unusually small twist elastic modulus of the nematic phase of LCLCs, the confined director configurations of this phase exhibit mirror symmetry breaking through twisted director configurations. Further, in the LCLC columnar phase, the hexagonal ordering of columns and the resultant strong suppression of twist and splay (but not bend) deformation, create droplets of this phase which adopt a concentric director configuration wherein the columns circle around a central bend disclination line and, at sufficiently high mesogen concentration, induce the drop to exhibit surface faceting. Our observations of all director configurations are consistent with Jones matrix calculations and are understood theoretically to be a result of the giant elastic anisotropy of LCLCs.

The director configurations of confined liquid crystals exhibit a rich phenomenology, the physics of which is determined by a delicate interplay of topology, elastic free energy, and anchoring conditions at the boundaries [96, 101, 104, 117–125]. Droplets present arguably the simplest and most symmetric confining container for liquid crystals. Droplets of thermotropic liquid crystals (TLCs) and manipulation of their director configurations, for example, are actively studied, in part because of their demonstrated use as core materials in display technologies [104, 126] and their potential applications ranging from biosensors [25, 26] to microlasers [27]. Significant fundamental and technological progress has been made with thermotropic liquid crystal droplets, because their bulk elasticity and surface anchoring phenomena are now well understood and easily controlled.

Here, we explore the behavior of aqueous LCLCs droplets suspended in a background oil phase. In contrast to TLCs, LCLC bulk elasticity and surface anchoring phenomena are not well understood. Thus the droplets provide an excellent platform for the study of basic LCLC properties because of their highly symmetric finite-volume confining geometry and, usually, due to their uniform boundary conditions. Our study investigates droplets similar to those in “classic” thermotropic LCs for which bulk elasticity and anchoring are easily characterized. Droplet size is comparatively more easily controlled in the water-in-

oil emulsions than in systems at nematic-isotropic coexistence studied in previous work [96, 100, 127, 128]. In particular, the water-in-oil emulsion system permits independent control of the continuous background phase into which one can add chemicals such as surfactants and through which one can regulate LCLC concentration to create isotropic, nematic, and columnar LCLC phases within the same drop.

In this thesis we investigate configurations of Sunset Yellow FCF LCLCs in surfactant-stabilized spherical water droplets. The experiments reveal a variety of unusual droplet types arising from the LCLCs' very small twist modulus and room-temperature columnar phase, and from planar anchoring of LCLC aggregates at the oil-water interface of a droplet. In the nematic phase, the director adopts a mirror-symmetry-breaking twisted-bipolar configuration with an extraordinarily large twist revealed by polarized optical microscopy (POM). These droplets provide an extreme example of an exotic structure that can be produced by the combination of geometric frustration and giant elastic anisotropy. In droplets of the columnar phase, which occurs at higher mesogen concentration, columns wrap in concentric circles around a central director disclination line while retaining their lattice structure. Interestingly, the lattice structure causes surface faceting of the soft container as the mesogen concentration is further increased.

### **2.3.1 Preparation of LCLC-in-oil emulsion**

Sunset Yellow FCF (SSY) was purchased from Sigma-Aldrich at a purity of 90%; it was then further purified using a published precipitation method [38, 40, 110]. Briefly, the SSY is well dissolved in deionized water at  $\sim 20\%$  (wt/wt) in a large centrifuge tube with spare volume. Pure ethanol was used to precipitate out the solution before centrifuging. That process was repeated  $3\times$ . The last time, SSY was dissolved in deionized water and poured into a petri dish and then placed in an oven to dry at  $60^\circ\text{C}$  for 24 hours. Note, since trace water left in dried SSY can affect the reported concentrations, it is advisable to place dried SSY in vacuum prior to preparing samples. The resultant SSY was dissolved in deionized water ( $18.2\text{ M}\Omega\text{ cm}$ ) to make a solution of a known concentration and phase. Hexadecane

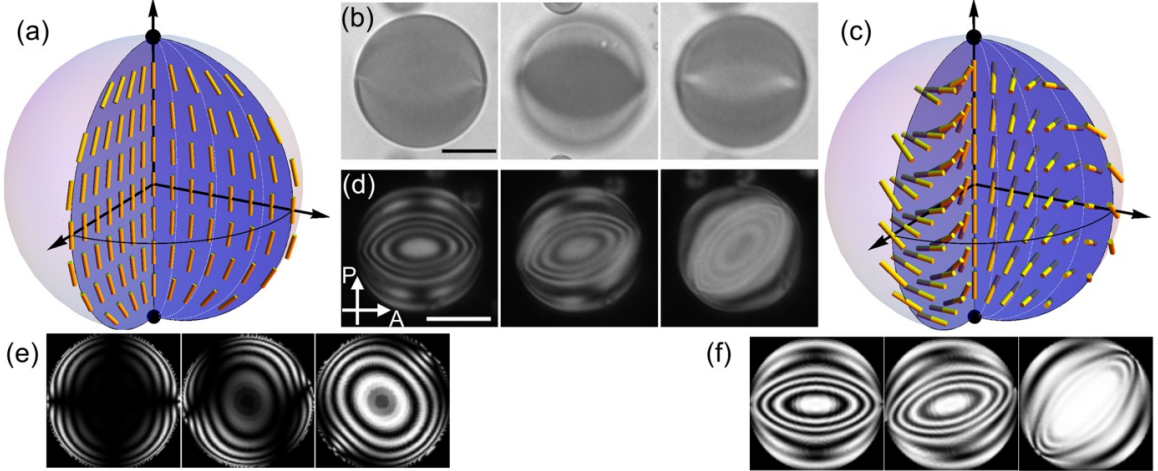


Figure 2.1: Optical microscopy images of a nematic LCLC droplet and Jones matrix calculations of the patterns in droplets between crossed polarizers. Scale bar: 20  $\mu\text{m}$ . (a) Bright-field microscopy images of the nematic droplet in different focal planes. (b) Polarized optical microscopy (POM) images of a droplet between a crossed polarizer (P) and analyzer (A); the pass axis directions are shown as white arrows. Each column shows a droplet at a different rotation angle. (c) and (d) Corresponding POM patterns simulated by Jones matrix calculations of light propagating through the droplet of (c) a bipolar configuration and (d) a twisted bipolar configuration. (e) and (f) Schematic diagrams of (e) the bipolar configuration and (f) the twist bipolar configuration. Black dots represent the defects at the droplet surface and short yellow arrows represent LC directors.

(99%, Sigma-Aldrich) and Sorbitan monooleate (Span 80, Fluka) were used as received. Span 80 was dissolved in hexadecane and used as a nonionic surfactant for the LCLC-in-oil emulsion.

The aqueous nematic SSY solution (31.0 wt%) was dispersed in hexadecane with a non-ionic surfactant (Span 80, 2.0 wt%) by pipetting and shaking. The volume fraction of SSY solution in hexadecane was approximately 1%, and the resulting nematic droplets had surface-tension stabilized spherical shapes with diameters ranging from 1  $\mu\text{m}$  to 100  $\mu\text{m}$ . A rectangular capillary with open ends (0.2 mm in height and 2 mm in width, VitroCom) was filled with this emulsion solution. While in the capillary, water in the droplet undergoes a slow evaporation through the oil phase leading to an increase of SSY concentration in the droplet and an eventual phase transition from the nematic to the columnar phase.

### 2.3.2 Energetics of Droplet Confined Director Configurations

We use cylindrical coordinates to parameterize the droplet director field with the droplet center at  $z = 0$ . The usual director configuration for thermotropic nematics confined to a sphere with tangential boundary conditions is the bipolar configuration [93, 104, 119], shown in Fig. 2.1(e); in such droplets two surface defects, called Boojums, arise and are located at the North and South Poles, and the director has no azimuthal component. Our LCLC droplets exhibit instead a chiral twisted bipolar configuration in which the director develops an azimuthal component in passing from the bipole axis connecting the Boojums; this behavior is most clearly observed in the out-of-focus images of Fig. 2.1(a), to the droplet surfaces as shown in Fig. 2.1(f).

To investigate this configuration more deeply, we derived sets of POM images of the droplet while rotating the sample (Fig. 2.1(b)). In Fig. 2.1(b), two surface defects in the droplet are approximately in the same plane, parallel to the substrate, an observation that is checked by examining the symmetry of the images under rotation. In order to determine whether the resultant structure is bipolar or twisted bipolar, we compare experimental observations to Jones matrix simulations. The patterns observed in the POM images differ significantly from the simulated POM images of the bipolar configuration (Fig. 2.1(c)); notice, for example, that the center of the droplet does not darken when the bipole axis is oriented parallel to either the polarizer or analyzer. By contrast, the patterns observed in the POM images are well described by a twisted bipolar configuration. Fig. 2.1(d) shows the Jones matrix simulation of the optical pattern of a twisted bipolar configuration that exhibits, among other features, a disconnected bright ellipse similar to that observed in Fig. 2.1(b) and in thermotropic chiral nematic droplets [129]. Schematics of the bipolar and twisted bipolar director configurations are shown in Fig. 2.1(e) and (f), respectively. In Fig. 2.1(e) and (f), the black dots correspond to the surface defects, and the short yellow arrows represent LC directors.

The twist angle  $\alpha_0$  of the director [Fig. 2.2(a)] at the equatorial surface relative to the bipole axis provides a quantitative characterization of the twisted bipolar structure.

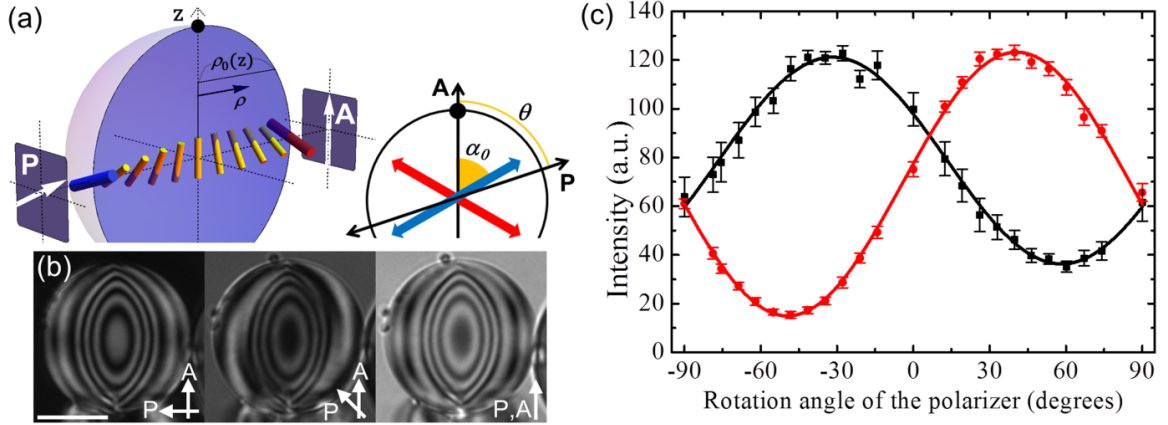


Figure 2.2: Intensity of transmitted light through the centers of droplets. (a) Schematic diagram of the twisted bipolar configuration between polarizer (P) and analyzer (A). Black dots represent the Boojums at the droplet surface, and the line connecting them is the bipole axis. The direction of the analyzer (A) is parallel to the bipole axis connecting two defects.  $\theta$  is defined by the angle between the polarizer (P) and the analyzer (A). Short yellow rods show LC directors along a chord through the center of the droplet only. Thick red and blue rods represent the entrance and exit LC directors, respectively.  $\rho$  is the radial coordinate in a cylindrical coordinate system with the  $z$ -axis along the bipole axis, and  $\rho_0(z)$  is the maximum value of  $\rho$  in a droplet at a given  $z$ . The inset on the right side shows the projection view through polarizer and analyzer, and defines  $\alpha_0$  as the angle between meridional lines and the entrance LC director at the surface of the droplet. (b) Polarized optical microscopy images of the droplet located between the polarizer (P) and analyzer (A) with directions shown as white arrows. Scale bar: 20  $\mu\text{m}$ . (c) Intensity of the transmitted light through the center of the droplet as a function of the angle between the polarizer and the analyzer. Black and red symbols are data from two representative droplets, and the solid curves are best fits to the data using equation (1). The error bars are the standard deviations of intensities over the central region of which the diameter is 10% of the droplet diameter.

Physically, it is determined by the ratios  $K_1/K_2$  and  $K_1/K_3$  of the splay modulus to the twist and bend moduli, respectively. According to Williams [94] and to Lavrentovich and Sergan [95], a director pattern in a spherical LC droplet with planar anchoring can break mirror symmetry when  $K_2$  is sufficiently small compared to  $K_1$  and  $K_3$ , *i.e.*, when  $K_3/K_1 \leq 2.32(1 - K_2/K_1)$ ; the twisted bipolar configuration has been observed in TLC droplets satisfying this condition [95, 115, 130]. The nematic SSY satisfies this condition for the twisted bipolar configuration [20], and the Williams' model predicts that these nematic SSY droplets should have a twist angle  $\alpha_0$  greater than  $80^\circ$ [94].

To estimate  $\alpha_0$ , we measured the transmitted light intensity under crossed polarizers through the centers of the twisted bipolar droplets. As in a thermotropic chiral nematic droplet with low chirality [129], it is reasonable to assume the twist angle,  $\alpha(\rho)$ , changes linearly with the distance  $\rho$  from the bipole axis (*i.e.*, the radial coordinate in a cylindrical coordinate system with the  $z$  axis along the bipole axis); *i.e.*,  $\alpha(\rho) = \alpha_0\rho/\rho_0(z)$  (Fig. 2.1(f)). Here  $\rho_0(z)$  is the maximum value of  $\rho$  in a droplet at a given  $z$ . Given the remarkable similarity in the optical patterns of the nematic LCLC droplet and a thermotropic chiral nematic droplet with low chirality [129], this assumption is reasonable. Specifically, along the diameter at  $z=0$ , the twist angle changes linearly on a path from surface to surface along a chord through the origin from  $+\alpha_0$  (red arrow) to  $-\alpha_0$  (blue arrow), passing through zero at the bipole axis (Fig. 2.2(a)). The central region can readily be approximated as the well-known planar twisted nematic cell often used in liquid crystal displays [130].

Figure 2.2(b) and (c) plot the intensity transmitted through this central region as a function of the angle of polarizer with respect to the fixed analyzer. The measured intensity reported in Fig. 2.2(c) is the average intensity over this central region (*i.e.*, a cylinder through the center of the droplet with a diameter  $\sim 10\%$  of the droplet diameter). The direction of the pass-axis of the analyzer is set parallel to the bipole axis that connects the two surface defects (Boojums). To determine  $\alpha_0$ , these intensity data are fit to equation (2.3.1) below, which is approximately equal to the transmitted light intensity through a corresponding planar twist cell as a function of the angle  $\theta$  of the entrance polarizer [130],

$$I = I_0 (\cos^2(\theta + 2\alpha_0) + \sin^2 X \sin(2\theta + 2\alpha_0) \sin^2 \alpha_0). \quad (2.3.1)$$

Here  $X^2 = (2\alpha_0)^2 + (\Gamma/2)^2$ ,  $\Gamma = 2\pi \Delta n d/\lambda$ , where  $\lambda$  is the wavelength of the illuminating light (*i.e.*, 650 nm),  $\Delta n$  (*i.e.*, -0.08)[38] is the difference in index of refraction for light polarized parallel versus perpendicular to the director, and  $I_0$  ( $I$ ) represents the intensity of the illumination (transmitted) light. For our droplets, the droplet diameter,  $d$ , is greater than 30  $\mu\text{m}$ , and the expected  $\alpha_0$  is on the order of 1 radian; thus, it is reasonable to assume that the droplets are in the Mauguin regime in which the polarization of the light follows the director as it traverses the medium. Equation (2.3.1) assumes the polarization guiding Mauguin regime. The solid lines in Fig. 2.2(c) are best fits to the data.

Surprisingly, the measurements suggest that the nematic LCLC droplets have a very large twist angle, *i.e.*,  $\alpha_0 > 90$  degrees. The average of  $|\alpha_0|$  over 18 different droplets was  $114.8 \pm 4.4^\circ$ . Note that twist angles greater than  $90^\circ$  were not reported experimentally in refs. [104] and [95, 115, 131], nor are they predicted by the largely accepted Williams' model (35). Additionally, the sign of the fitted  $\alpha_0$  implies a certain handedness of chirality; both signs were observed in the droplet sample. Based on the number ratio between positive and negative twist angles (*i.e.*, 7:11) across all droplets, it appears that there is no preferred handedness of chirality in these systems (*i.e.*, within our statistical error). Interestingly, these droplets look remarkably similar to thermotropic chiral nematic droplets with a half-pitch less than a diameter of the droplet, *i.e.*, droplets in which  $\alpha_0$  is greater than  $90^\circ$  [129]. Our model of the twisted bipolar droplet is independent of the droplet size. To test for a size dependence, we searched for correlations between  $\alpha_0$  and the size of the droplet for droplets with diameters in the range of 30 to 80  $\mu\text{m}$ , but we found none.

Lastly, in order to understand this large mirror symmetry breaking in droplets at a fundamental level, we carried out a numerical calculation of elastic free energy based on a simplified director field model. To this end, we followed Xu and Crooker [115, 129] and assumed a simplified director field for the twisted bipolar configuration  $\mathbf{n}_{tb} = \mathbf{n}_b \cos(\alpha) + \mathbf{n}_c \sin(\alpha)$ , which combines the bipolar configuration  $\mathbf{n}_b$  and the concentric configuration  $\mathbf{n}_c$ .

For the droplet calculations, we employ the director field models for the bipolar configuration and the concentric configuration used by Ding and Yang [114].

Assuming a linearly changing  $\alpha(\rho) = \alpha_0\rho/\rho_0(z)$ , we numerically calculate the elastic free energy of each deformation mode and compute their sum as a function of  $\alpha_0$  as shown in Fig. 2.3(a). Note that the splay energy exhibits a minimum at  $\alpha_{\min} \sim 130^\circ$ , which sets an upper bound on  $\alpha_0$ , while the elastic free energy of the twist and bend deformations increase monotonically with  $\alpha_0$ . Therefore, the total elastic free energy has its minimum at non-zero  $\alpha_0$ . For example, for  $K_2/K_1 \sim 0.09$  and  $K_3/K_1 \sim 0.91$  in a 31.5% (wt/wt) SSY solution [20], the twist angle is expected to be  $\alpha_0 \sim 90^\circ$ . At higher concentrations, because  $K_1$  and  $K_1/K_2$  and  $K_1/K_3$  increase [20], the  $\alpha_0$  of the minimum elastic free energy increases and can surpass  $90^\circ$ . This effect is shown in Fig. 2.3(b) for  $K_2/K_1 \sim 0.07$  and  $K_3/K_1 \sim 0.67$ , wherein the droplet has  $\alpha_0 \sim 100^\circ$ . In practice, the evaporation of water from the droplet into the background oil phase increases the SSY concentration in the droplet from its initial value of 31.0% (wt/wt), thereby increasing  $K_1$ . It is thus reasonable for  $\alpha_0$  to reach values greater than  $90^\circ$ . Note, however, the untwisted bipolar configuration ( $\alpha_0 = 0$ ) is preferred at sufficiently large values of  $K_2/K_1$  as shown in Fig. 2.3(b), which is consistent with the Williams condition for the twisted bipolar configuration.

To conclude this section we explore the spatial dependence of the elastic free energy in the region around the defect. Indeed, it is the behavior in the vicinity of the defect that dominates the determination of the twist angle  $\alpha_0$ . Fig. 2.3(c) plots the total elastic free energy of each  $z/R$  integration range where the  $z$  axis is along the bipole axis and  $R$  is the radius of the droplet. With this notation, when  $z/R = 0.8 - 1$ , the integration volume is a spherical cap near the defect, and when  $z/R = 0.0 - 0.2$ , the integration volume is a thin disk near the droplet equator. Remarkably, we see that most of the elastic free energy is concentrated in the region around the defect where splay is largest. Figures 2.3(d) and (e) summarize the contributions of splay, twist, and, bend to the energy densities of the bipolar ( $\alpha_0 = 0$ ) and twisted bipolar ( $\alpha_0 = 90$ ), respectively. In both cases, splay in the vicinity of the boojum dominates the energy. This energy, however, decreases with increasing twist

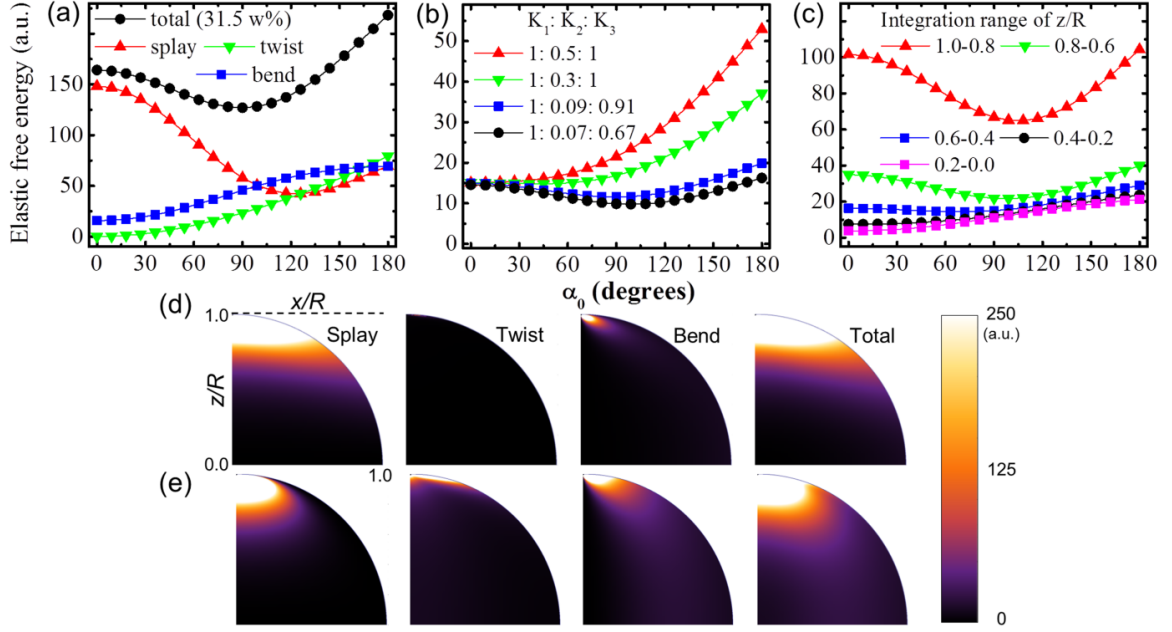


Figure 2.3: Numerically calculated elastic free energy of the twisted bipolar configuration as a function of twist angle,  $\alpha_0$ . (A) Splay, twist, bend elastic free energies, and their sum, for the twisted bipolar configuration droplet of 31.5% (wt/wt) SSY solution with  $K_1 : K_2 : K_3$  equal to 11:1:10. (B) Same calculation of total elastic free energy of a twisted bipolar configuration droplet but with different  $K_1 : K_2 : K_3$ . (C) Total elastic free energy of different integration ranges of  $z/R$  in a droplet. (D) Elastic free-energy density of each deformation mode and their sum in the first quadrant of the droplet's cross-section for  $K_1 : K_2 : K_3$  equal to 11:1:10 for the bipolar configuration ( $\alpha_0 = 0^\circ$ ) and (E) for the twisted bipolar configuration ( $\alpha_0 = 90^\circ$ ). Note that splay deformation in the region around the defect dominates the free-energy density but decreases substantially with twist angle  $\alpha_0$ .

angle, while the twist and bend energy increase slowly. The equilibrium value of  $\alpha_0$  is determined by the balance between these two effects.

### 2.3.3 Faceted Columnar Phase Droplets

To study LCLC droplets in the columnar phase [132], the concentration of SSY in the droplet was increased by evaporation of water through the oil phase. As a result, the liquid crystal in the droplets experienced a phase transition from nematic to columnar phase through the coexistence region. The columnar phase droplets exhibit a concentric director configuration as shown in Fig. 2.4(a). The director encircles a bend disclination line defect along the bipole axis. Fig. 2.4(b) shows a sequence of POM images of the droplet at different rotation angles, along with corresponding Jones matrix calculations (Fig. 2.4(c)) of the concentric configuration [114]. The director field model of the concentric configuration is shown in Fig. 2.4(d); here the short yellow arrows and the thick black line correspond to the LC directors and the line defect, respectively, and the dotted white lines indicate the 2D triangular lattice of the columnar phase in the droplet. Note that both the POM images and Jones matrix calculation in the concentric configuration are quite different from those of the twisted bipolar configuration (Fig. 2.1(b) and (d)). Although both patterns appear as nested ellipses, the ellipses of the concentric configuration are sharper near the ends of the major axis, *e.g.*, compared to those of the twisted bipolar configuration. In addition, a droplet in the concentric configuration has low transmittance through crossed polarizers when the line defect is parallel to either the polarizer or the analyzer.

This concentric configuration is also a result of the large elastic anisotropy of the columnar phase. The lattice structure of the 2D hexagonal columnar phase strongly suppresses twist and splay but not bend deformation. Therefore, it is natural for the columnar droplet with planar anchoring to take on the concentric configuration in which only bend deformation exists. Further, as shown in Fig. 2.4(d), this configuration can maintain 2D hexagonal ordering throughout the droplet except at the core line defect. Such a configuration, which is curved on a large scale even though the lattice of the columnar mesogens is not deformed,

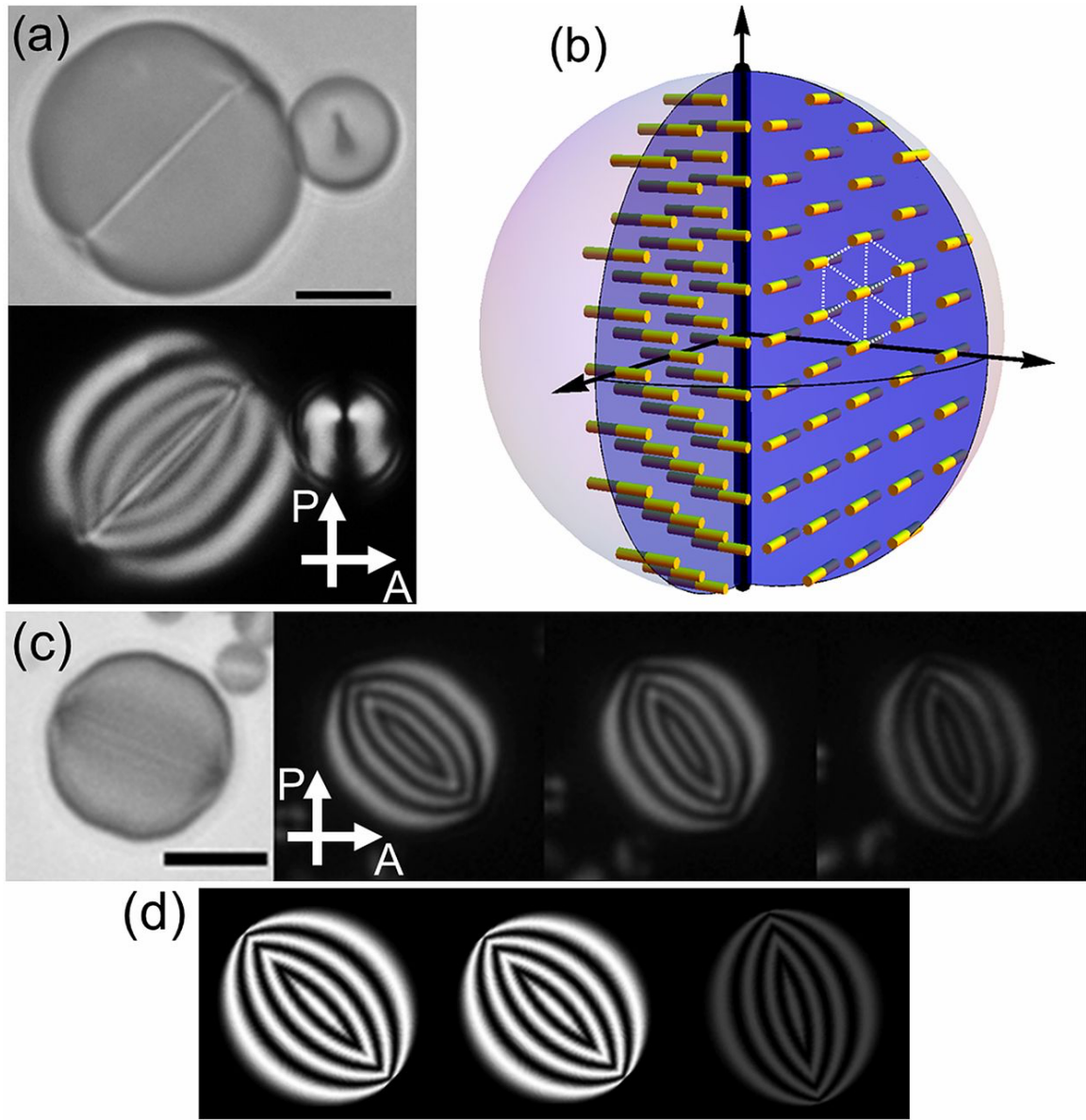


Figure 2.4: Optical microscopy images of a columnar LCLC droplet and Jones matrix calculations of light patterns after passing through a droplet located between crossed polarizers. Scale bar, 10  $\mu\text{m}$ . (A) Bright-field microscopy image (Upper) and POM image (Lower) for columnar phase droplets between a crossed polarizer (P) and analyzer (A) with pass-axis directions shown as white arrows. (B) Schematic diagram of the concentric configuration; the short yellow rods and the thick black line indicate the LC directors and the line defect, respectively. The hexagon of dotted white lines depicts the 2D hexagonal ordering of columns in the columnar phase. (C) Bright-field microscopy image and a sequence of POM images as a function of droplet orientation. (D) Results of Jones matrix calculations of droplet patterns for a concentric configuration.

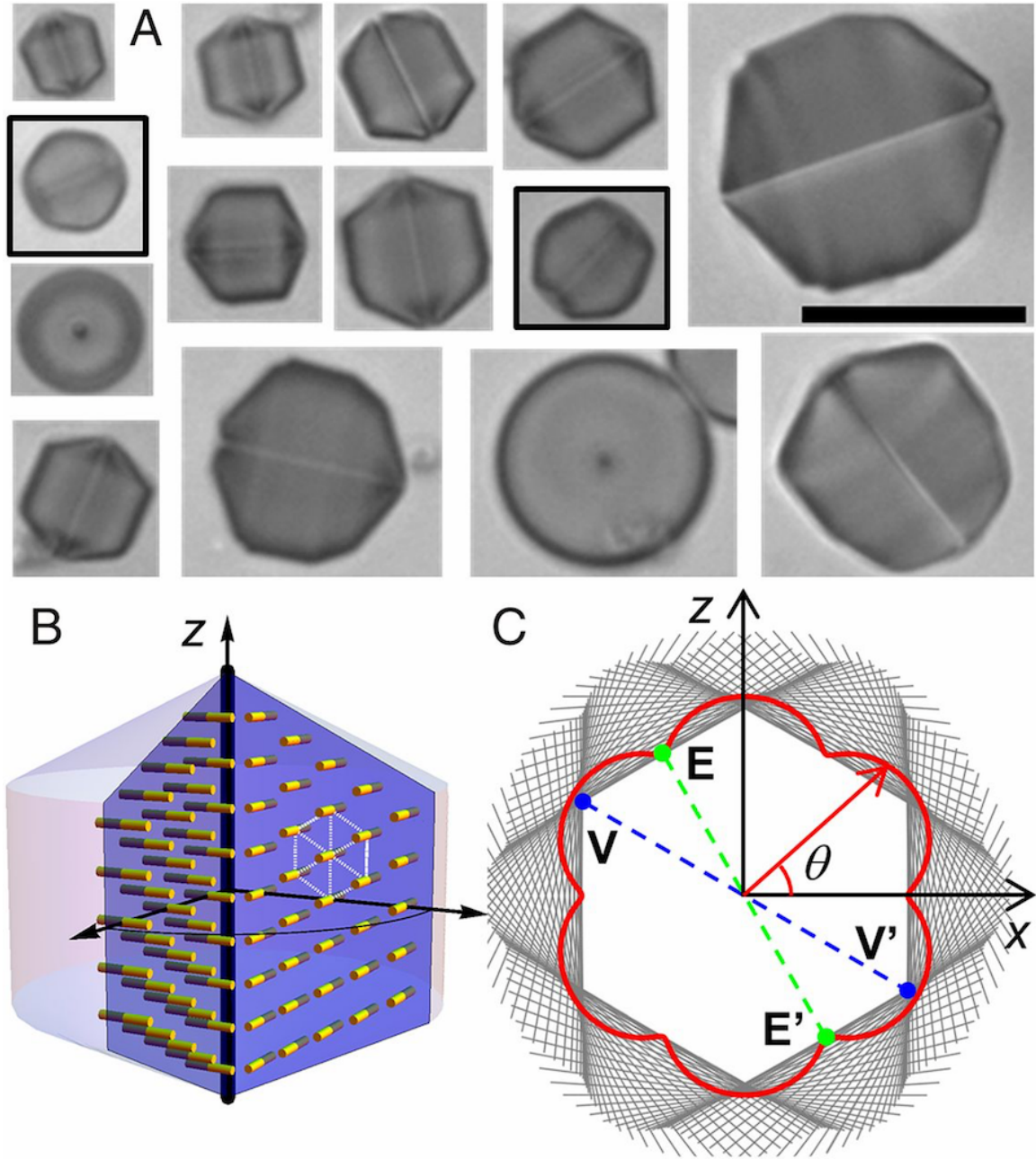


Figure 2.5: Bright-field microscopy images of columnar LCLC droplets with facets and schematic diagrams of the Wulff construction of faceted droplets. (A) Bright-field microscopy images. Scale bar, 30  $\mu\text{m}$ . The circular image with a black dot at its center is obtained when the droplet is viewed along the line defect. (B) Schematic diagram of the concentric configuration with facets; the short yellow rods and the thick black line indicate the LC directors and the line defect, respectively. The hexagon of dotted white lines depicts the 2D hexagonal ordering of columns in the columnar phase. (C) Wulff construction of hexagonal crystal. A polar plot (red curve) represents a sixfold interfacial tension of the columnar phase in the plane of 2D hexagonal ordering ( $xz$  plane). The Wulff construction of the polar plot predicts hexagonal crystal shown as the inner envelope of normal lines (gray straight lines) to the polar plot.  $V(E)$  and  $V'(E')$  represent opposite vertices (centers of opposite edges) and dashed lines connecting them are the rotation axes of the faceted droplets.

is called a developable domain [9, 133]. Thus the observed concentric configuration corresponds to a spherical developable domain, and the central disclination line defect is its 1D singularity. In contrast to the behavior in the nematic phase, the line defect cannot have an escaped structure, because splay deformation is not allowed.

At the very highest concentrations studied, columnar phase droplets exhibit an even more remarkable behavior, developing facets in the soft droplet surface that can be described by the Wulff construction [134, 135]. As shown in Fig. 2.5(a) and (b), the columnar droplets develop facets as the LCLC concentration increases. The droplets maintain rotational symmetry about the core line defect. For smaller droplets, the cross section containing the line defect more closely resembles a hexagon as shown in Fig. 2.5(a). This hexagonal shape can be understood using the Wulff construction to describe the equilibrium shape of a crystal in terms of its anisotropic interfacial energy. In the 2D-Wulff construction, we start with a polar plot of the interfacial energy as a function of orientation and then draw lines normal to the radial direction everywhere on the polar plot. The inner envelope of these normal lines describes the equilibrium shape of a crystal that minimizes total interfacial energy [134, 135]. Specifically, in the cross section containing the line defect shown in Fig. 2.4(e), the columnar phase is a 2D crystal with hexagonal ordering. Assuming the anisotropic interfacial energy has the 6-fold symmetry shown in the polar plot of the interfacial tension in Fig. 2.5(c), then the Wulff construction of this 6-fold interfacial tension leads to the hexagonal crystal (Fig. 2.5(d)). Presumably, the irregular facets in larger droplets may result from polycrystalline domains or non-uniform evaporation of water from the droplet.

### 2.3.4 Double Emulsions of LCLC with DSCG

Though disodium cromoglycate (DSCG) and SSY are the most common forms of LCLC and both are readily available, they have very different properties [21, 106]. For instance, DSCG forms its nematic and columnar phase at much lower concentrations than SSY and has even larger ratios of splay and bend to twist elastic modulus. To further explore these differences, we performed preliminary experiments with DSCG LCLC in double emulsions. Double

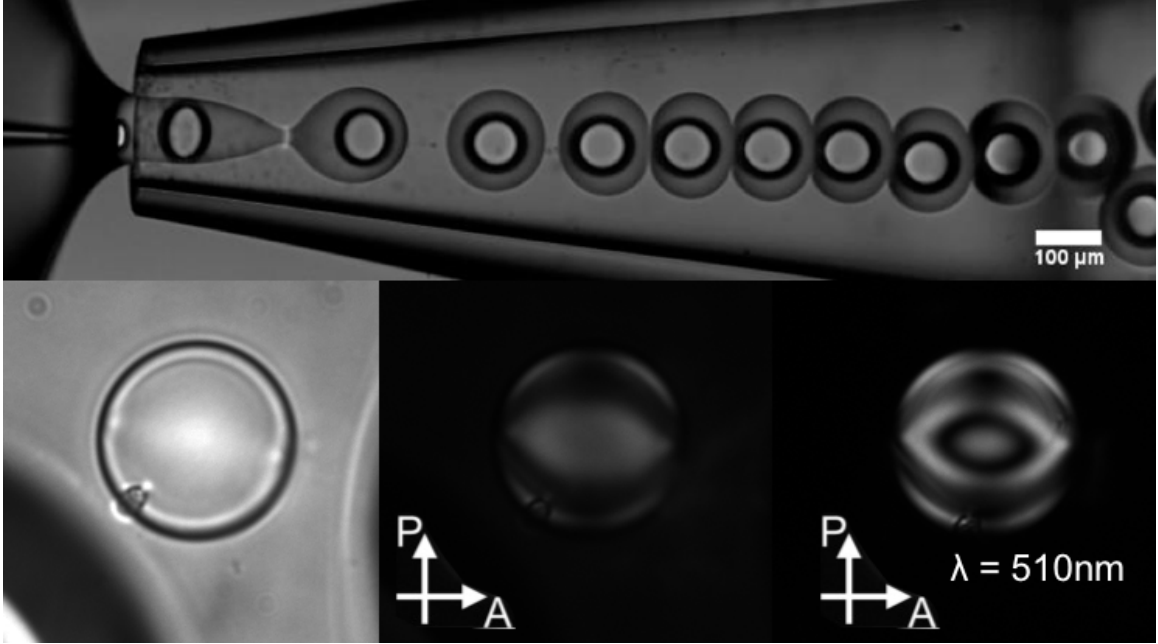


Figure 2.6: Double emulsion drops of disodium cromoglycate (DSCG) are produced in the isotropic phase. After salt is added to the outer continuous phase, the inner DSCG drops transition to the nematic phase. The director configuration is a twisted bipolar structure similar to that found in SSY though  $\alpha_0$  was not determined here.

emulsions of a water-oil-water (continuous-shell-inner) type allow for the concentration and dilution of the inner most phase through osmosis by control of the salinity in the continuous outer phase. Droplets of DSCG at an initial concentration of 5 % wt/wt were produced by concentric capillary flow in a chloroform and Span 80 (2 % wt/wt) mixture [136]. The outer most phase had a 1% wt/wt concentration of polyvinyl alcohol and the salt (NaCl) concentration was varied to affect the inner droplet phase. Drops had an initial diameter of 100 μm as in Fig. 2.6. The outer phase was gradually replaced with a 1 M NaCl solution. In these conditions, the inner drops rapidly expel water and the LCLC mixture enters the nematic phase (Fig. 2.6). As with SSY, DSCG droplets in the nematic phase also form twisted bipolar structures. However, at higher concentrations in the columnar phase, an different droplet shape emerges.

As the salt concentration in the continuous phase is further increased, the concentration of the inner droplets of DSCG further increases as well. The inner droplets of DSCG enter the columnar phase and quickly became non-spherical (Fig. 2.7). The columnar phase can

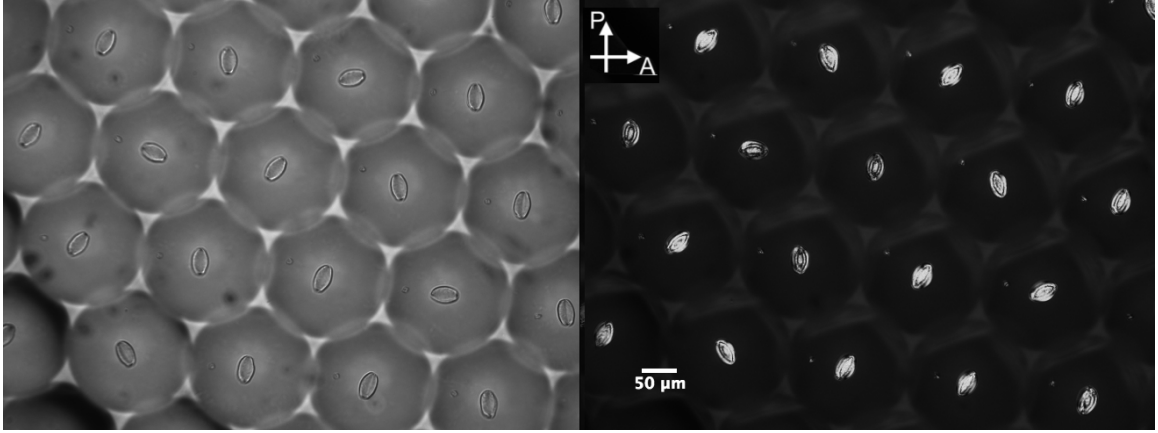


Figure 2.7: Double emulsion drops of DSCG in the columnar phase. The director configuration must be a concentric structure similar to that in SSY because only bend deformations are possible in the columnar phase. However the unusual shape of the drops implies the packing of DSCG columns in the columnar phase is somewhat different than the triangular lattice that gives rise to faceted drops with a hexagonal cross section as in SSY.

only be deformed with bend; it does not permit splay or twist deformations. The unusual ellipsoidal shape of the droplets indicates that, as in the case of SSY faceted droplets, the DSCG nematic elastic energy must be greater than the surface tension energy. The droplets shape is again determined by a Wulff construction, but in the case of DSCG, the underlying interfacial tension polar plot must have a different shape, possibly oblique. X-ray and neutron studies of columnar phase DSCG have found varying configurations of the columns [137–139]. Further experiments with double emulsion droplets of DSCG are necessary to understand the interplay between the columnar phase structure and surface tension.

### 2.3.5 Summary of LCLC Droplet Results

We have made lyotropic chromonic liquid crystal droplets with planar anchoring and studied their director configurations as a function of LCLC concentration. In nematic droplets, a very small twist elastic modulus produces an unprecedentedly large mirror symmetry breaking that can be understood theoretically using simple elastic free energy models with large elastic anisotropy. Interestingly, despite their lack of chirality, the nematic LCLC droplets have a chiral twisted bipolar configuration similar to those observed in droplets of liquid crystals with intrinsic chirality. Columnar LCLC droplets, by contrast, exhibit a concentric

director configuration with a central disclination defect, corresponding to a spherical developable domain with a 1D singularity. Additionally, because of 2-D crystalline ordering of the columnar phase, the columnar droplets at the highest concentrations develop facets resulting in a hexagonal shape. In the future we should be able to utilize the advantages of this emulsion system to study configurations with different boundary conditions and in various classes of external field. As in the present investigation, we expect the resultant configurations to shed new light on our understanding of the delicate interplay between bulk elasticity and surface anchoring phenomena in LCLCs. Furthermore, the unique shapes and configurations formed, and the broken mirror symmetry, may offer new possibilities for control and application materials based on complex colloids.

## 2.4 Cylindrical Confinement with Homeotropic Anchoring

In this section, we introduce novel mirror-symmetry-broken configurations of nematic LCs in a cylindrical confinement geometry, and we explore the energetics of the configurations and their defects. This general class of configuration has been investigated in cylinders [105, 140–144]. However, the present system differs significantly from earlier work. The configurations we report on have homeotropic boundary conditions, and their chirality is not of molecular origin, *i.e.*, handedness is not derived from chiral mesogens nor dopants.

Our mirror symmetry breaking experiments in cylinders employ Sunset Yellow FCF (SSY), a lyotropic chromonic liquid crystal (LCLC) with small twist elastic constant, in polymer-coated capillaries. SSY is composed of columnar aggregates of organic, plank-like molecules in water. A polymer coating on the inner surface of the hollow cylinders induces homeotropic anchoring (director perpendicular to the surface) of the aggregates on the cylinder surfaces via noncovalent interactions [145]. The polymer coating is conformal and is derived by chemical vapor deposition which permits homeotropic alignment on curved cylinder surfaces. Again we note that besides their biocompatibility [146, 147], the LCLCs are known for their very small twist modulus compared to splay and bend moduli. This mechanical property renders LCLCs susceptible to spontaneous mirror symmetry breaking

[20, 21].

The nematic phase of SSY was found to exhibit two different configurations in the cylinder: one twisted- and escaped-radial (TER) or twisted-escaped-radial, and the other with a double helix of disclinations. The samples also exhibited a variety of chiral defects originating from symmetry breaking. In this thesis, we investigate their structure and energetics using polarized optical microscopy (POM), numerical calculations of director configurations based on elastic free energies, and Jones-matrix-simulated optical textures. The new chiral director configurations and defects provide qualitatively new examples of mirror symmetry breaking arising from elastic anisotropy, and demonstrate the consequences of a delicate interplay between anisotropic elasticity, boundary conditions, chirality and topological defects.

The mirror symmetry breaking experiments in polymer-coated capillaries are carried out using Sunset Yellow FCF (SSY), a lyotropic chromonic liquid crystal (LCLC) with small twist elastic constant. As noted above, besides the new director configurations, a rich phenomenology of defects also arises from the degenerate bend/twist deformations of the TER configuration, including a non-singular domain wall separating domains of opposite twist handedness but the same escape direction, and singular point defects (hedgehogs) separating domains of opposite escape direction. We demonstrate the energetic preference for singular defects separating domains of opposite twist handedness compared to those of the same handedness. We also report remarkable chiral configurations with a double helix of disclination lines along the cylindrical axis.

#### **2.4.1 Preparation of Capillaries with Homeotropic Anchoring**

The hollow cylinders were made from glass capillaries. Borosilicate glass capillaries were obtained from Vitrocom, and their inner diameters ranged from 50  $\mu\text{m}$  to 200  $\mu\text{m}$ . Parylene-N polymer films were deposited by chemical vapor deposition using a commercial parylene coater (PDS2010, Specialty Coating Systems) [145]. In this process, 0.5 – 2 g of [2.2]paracyclophane was deposited under vacuum conditions ( $\sim 55$  mTorr) onto every exposed surface

of the capillary. The temperatures for vaporization, pyrolysis and deposition of parylene-N were 160°C, 650°C, and 20°C, respectively.

Sunset Yellow FCF (SSY) was purified as described in 2.3.1. The purified SSY was then dissolved in deionized water (18.2 M $\Omega$  cm) in order to make nematic SSY solutions whose concentration ranged from 29.0% (wt/vol) to 31.5% (wt/vol). Vacuum suction was applied to one end of the capillaries in order to fill the interior of the parylene-coated capillaries with the nematic SSY solutions (LC was introduced into the system from the other end of the capillary). The capillaries were then placed on glass microscope slides and sealed with epoxy glue to prevent water evaporation. We covered the sample with an ITO-coated glass, and the gap between the ITO-coated glass slide and the glass substrate was filled with index matching oil ( $n = 1.474$  at wavelength = 589.3 nm). The oil and the capillaries therein could be electrically heated by the ITO-coated glass; its temperature was measured by a thermocouple submerged in the oil. A PID circuit (CNi32, Omega) controlled the sample temperature between 23°C and 65°C with a stability of  $\pm 0.1^\circ\text{C}$ .

#### **2.4.2 Mirror Symmetry Breaking and the Twisted-Escaped Radial Configuration**

Polarized optical microscopy (POM) images of nematic SSY in capillaries with homeotropic boundary conditions exhibit features that are subtly different from those in the POM images of samples in the well-known escaped-radial (ER) configuration [148–150]. In the bright-field microscopy image Fig. 2.8A, a flickering speckle pattern follows the LC director field of the escaped-radial configuration; such anisotropic speckle patterns result from thermal fluctuations of the LC directors and accompanying fluctuations of the local extraordinary index of refraction [149, 150].

The LC directors are radial near the capillary wall and bend along the radius to be parallel to the cylindrical axis near the sample center; the choice between two degenerate directions of bend deformation determines the escape direction. The center of the escaped-radial configuration appears extinguished under perpendicularly crossed polarizers when

either a polarizer or an analyzer is oriented parallel to the cylindrical axis. The extinguished intensity arises in this case because all LC directors along the central beam path lack an azimuthal component [ $\alpha(r, \phi, z) = 0$ ] (see Fig. 2.9A for angle definitions). In Fig. 2.9A,  $\beta(r, \phi, z)$  is the angle between the  $z$  unit-vector ( $\hat{z}$ ) and an LC director ( $\mathbf{n}$ ) at  $(r, \phi, z)$ ;  $\alpha(r, \phi, z)$  is the angle between the  $r$  unit-vector ( $\hat{r}$ ) and the x-y projection ( $\mathbf{n}_{xy}$ ) of the director at  $(r, \phi, z)$ . Thus the bright central region of the nematic SSY, shown in Fig. 2.8B, indicates the director configuration is different from common escaped-radial (ER) configurations. Furthermore, Fig. 2.8D and 2.8E, POM images with a full-wave plate inserted into the beam path, reveal the existence of two different director configurations with the same escape direction.

Because nematic SSY has a small twist elastic modulus compared to splay and bend moduli, it adopts a twisted- and escaped-radial (TER) configuration (or twisted-escaped radial) in cylinders with homeotropic boundary conditions. In contrast to the escaped-radial configuration with no azimuthal component, [ $\alpha(r, \phi, z) = 0$ ], the TER configuration has both non-zero  $\alpha(r)$  and  $\beta(r)$  with azimuthal symmetry. For example, Fig. 2.9B shows numerically calculated  $\alpha(r/R)$  and  $\beta(r/R)$  for the 31.5% (wt/vol) SSY at 25.0 °C; here  $R$  is the cylinder radius, and the ratio between splay, twist, and bend moduli is  $K_1 : K_2 : K_3 = 1 : 0.09 : 0.94$  [20]. Notice that  $\beta(r/R)$  exhibits considerable deviation from  $2 \arctan(r/R)$ , the analytic solution of the escaped-radial (ER) configuration when  $K_1 = K_3$ . (Note also that the conditions  $\alpha(r/R = 1) = 0^\circ$  and  $\beta(r/R = 1) = 90^\circ$  indicates that the directors satisfy the homeotropic boundary condition, and the condition  $\beta(r/R = 0) = 0^\circ$  corresponds to directors pointing parallel to the cylindrical axis at the center of the cylinder.)

The TER configuration is depicted in Figs. 2.9C and 2D. Because of the non-zero twist, encoded by non-zero  $\alpha(r)$ , the configuration is chiral and can be either right-handed or left-handed. For instance, the configuration of Fig. 2.9C and 2.9D is right-handed according to the convention of the handedness of helices; *i.e.*, the streamlines formed by the directors trace out right-handed helices. Finally, note that the simulated optical textures based on these numerically calculated profiles, shown in Fig. 2.8, match the experiments quite well.

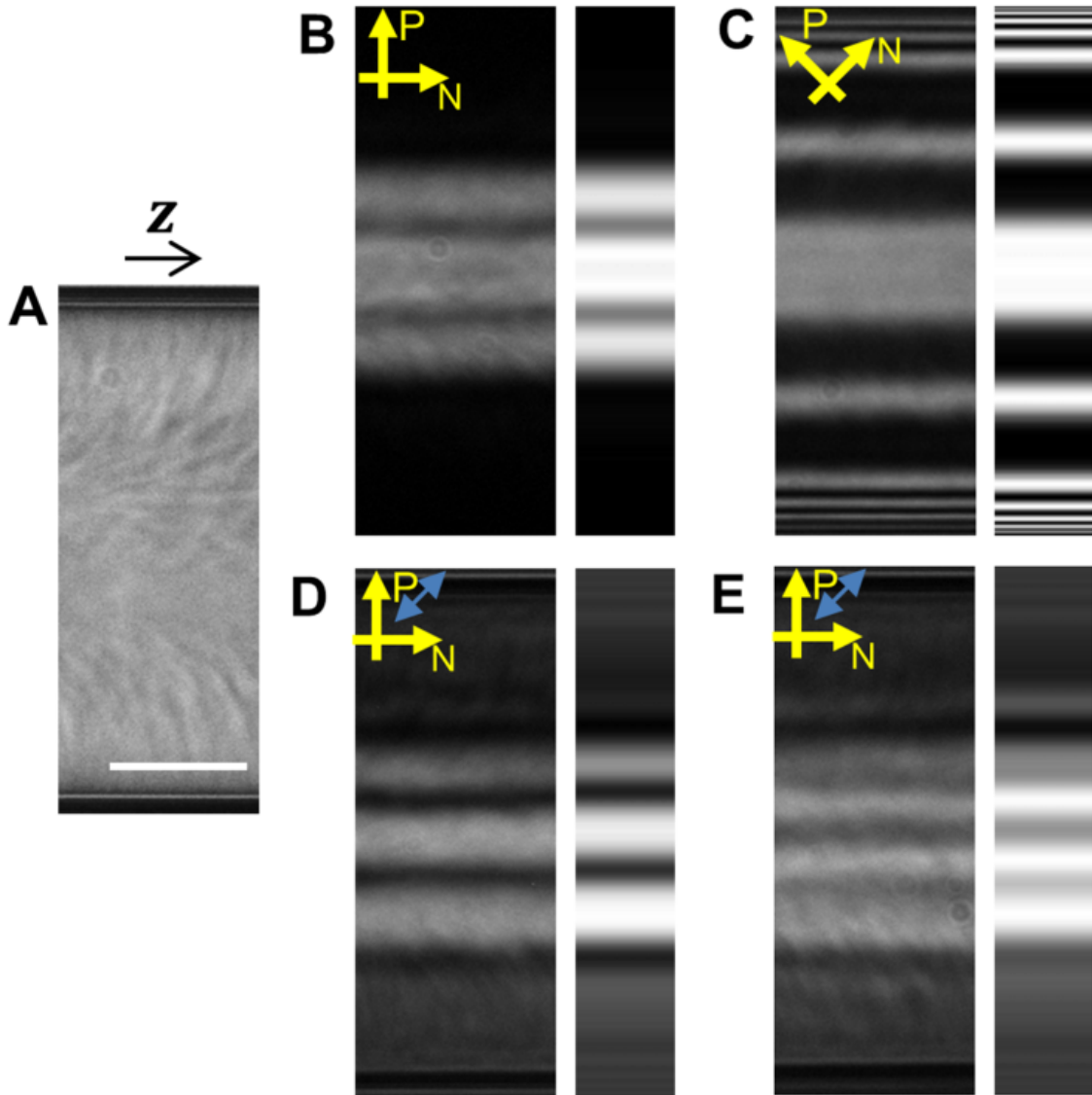


Figure 2.8: Optical microscopy images and simulated patterns of nematic SSY in a cylinder between crossed polarizers with and without a full-wave plate;  $z$  is parallel to the cylindrical axis of the capillary. The concentration and temperature of SSY are 31.5% (wt/wt) and 25.0 °C, respectively. (A) A bright-field microscopy image of nematic SSY with a TER director configuration escaping toward  $z < 0$ . Notice the directional texture resulting from thermal fluctuations of the LC directors. In (B-E), (Left) POM images of the TER director configuration under monochromatic illumination (wavelength = 650 nm) and (Right) corresponding POM patterns simulated by Jones matrix calculations of a director-field model between a polarizer (P) and an analyzer (N) with and without a full-wave plate are shown; the pass axis directions of the polarizers are shown as single-headed yellow arrows, and the slow axis of the wave plate is shown as a double-headed blue arrow. The escape directions are identical, and the twists in (D) and (E) are left- and right-handed, respectively. (Scale bar: 25  $\mu\text{m}$ ).

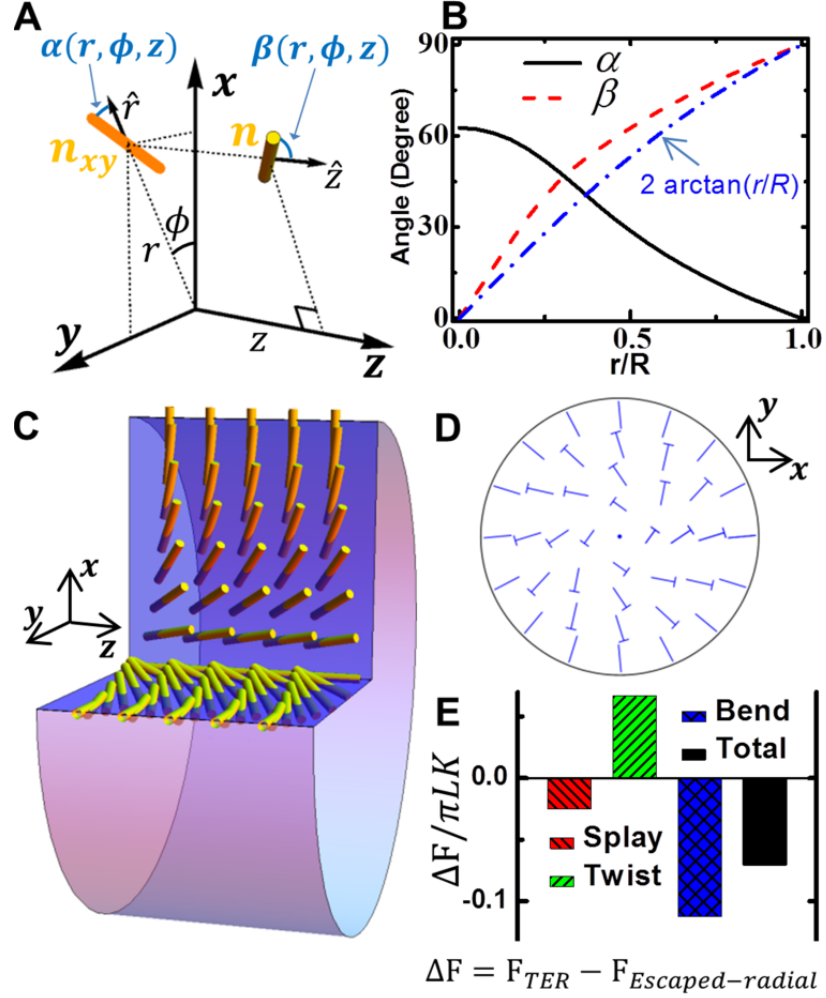


Figure 2.9: A TER director configuration. (A) A cylindrical coordinate system  $(r, \phi, z)$  is used to describe the TER director configuration, where  $z$  is parallel to the cylindrical axis;  $\beta(r, \phi, z)$  is defined by the angle between the  $z$  unit vector ( $\hat{z}$ ) and an LC director ( $\mathbf{n}$ ; an orange rod) at  $(r, \phi, z)$ , and  $\alpha(r, \phi, z)$  is defined by the angle between the  $r$  unit vector ( $\hat{r}$ ) and the  $x - y$  projection ( $\mathbf{n}_{xy}$ ) of the director at  $(r, \phi, z)$  (Eq. 2). (B) Numerically calculated profiles of  $\alpha$  and  $\beta$  in the TER director configuration as a function of  $r/R$  when  $K_1 : K_2 : K_3 = 1 : 0.09 : 0.94$  [*i.e.*, the elastic moduli values for 31.5% (wt/wt) SSY at 25.0 °C].  $R$  is the radius of the cylindrical confinement. The blue dash-dot curve corresponds to  $2 \arctan(r/R)$ , which is the dependence of  $\beta$  on  $r/R$  of the escaped radial configuration without twist ( $\alpha = 0$ ) when  $K_1 = K_3 = K$  and  $K_2$  is greater than the critical value  $K_2^c \approx 0 : 27K$ . C and D provide schematic diagrams of a right-handed TER director configuration. In C (the perspective view), yellow rods represent LC directors. Here, the directors escape to the west. In D (the cross-sectional view), the directors are shown as nails with heads that come out of the page. (E)  $\Delta F$  represents the splay, twist, and bend elastic energies and their sum in the TER configuration ( $F_{TER}$ ) minus the corresponding parameters in the twistless escaped radial director configuration ( $F_{Escaped-radial}$ ). ( $\Delta F$  is the energy difference between configurations for each parameter and their sum.)  $L$  is the cylinder length.

The TER configuration lowers the elastic free energies of the escaped-radial configuration by introducing a twist deformation with degenerate right- or left-handedness. Specifically, our numerical calculations suggest that with  $K_1 = K_3 = K$ , the total elastic free energy of the TER configuration becomes smaller than that of the escaped-radial configuration when  $K_2 < K_2^c \approx 0.27K$ . Thus, as shown in Fig. 2.9E, the TER configuration has less splay, bend, and total elastic free energies than corresponding energies in the escaped-radial configuration at the expense of increased twist elastic free energy. The two different directions of the twist deformation, *i.e.*, the handedness, have the same elastic free energy and have been observed experimentally with no noticeable preference for either handedness. In other words, the mirror symmetry of the confined achiral nematic SSY is spontaneously broken because of its very small twist modulus compared to the other moduli. Chiral structures are thus generated from a liquid crystal with achiral mesogens.

We note that while one might be tempted to consider these experiments as a simple extension of our experiments in spherical drops (described earlier in this chapter), the energetics of mirror symmetry breaking in cylinders are quite different from the energetics in the recently reported spherical droplets of nematic LCLCs [1]. In the case of spherical droplets with planar anchoring, two topological point defects called Boojums play a critical role in mirror symmetry breaking. Energetically cheap twist deformation cancels out strong splay elastic free energy near the defects in order to achieve the well-known twisted bipolar configuration; twist deformation, however, increases bend elastic free energy. In the cylinder work, singular defects do not play a role in the formation of TER configurations. Moreover, as shown in Fig. 2.9E, the twist deformation cancels both splay and bend elastic free energies, and the contribution from bend cancellation is much greater than the one from splay cancellation. For instance, if the bend modulus increases while the other moduli are fixed, the twist angle in the TER configuration increases, while the twist angle in the twisted bipolar configuration decreases. The latter effect occurs because the twist deformation increases bend elastic free energy in the twisted bipolar configuration.

### 2.4.3 Topological Defects of the Twisted-Escaped Radial Configuration

The two degenerate escape directions and the two degenerate senses of handedness (right/left) in the TER configuration lead to three possible types of defects for these systems: radial point defects, hyperbolic point defects, and non-singular domain walls separating regions opposite handedness. Singular point defects (hedgehogs) have been observed previously in the common escaped radial configuration without twist, and they are located in regions where the escape direction changes [148–153]. Fig. 2.10 shows experimental and simulated images of our system, which possesses twist. In Fig. 2.10 A and B, a singular radial (hyperbolic) defect is found to arise when the two opposite escape directions (*e.g.*, toward  $z > 0$  or  $z < 0$ ) of the TER configuration converge (diverge). The flickering speckle patterns in the bright-field images in Fig. 2.10 provide clues that help us identify the type of defect. The radial and hyperbolic defects always appear in pairs because of the conservation of topological charge enforced by the boundary condition; indeed, annihilation of defects by merging of adjacent pairs was occasionally observed.

In addition to these singular defects, we observed a nonsingular defect with no change in the escape direction, which is shown in Fig. 2.10C; it is a domain wall across which the handedness of the twist changes (*e.g.*, from left to right). In Fig. 2.10, the POM images and corresponding simulation images clearly show a modulation of the LC directors as a result of handedness inversion. A POM image with a full-wave plate is shown in Fig. 2.11C, and it shows the handedness inversion; notice that the right- and left-end regions in Fig. 2.11C differ, despite the same escape direction, and they match Fig. 2.8 D and E, respectively. A pair of domain walls will also undergo annihilation by merging, and such annihilations were often observed experimentally.

The escape direction changes sign in passing from one side of a hedgehog to the other in the common escaped-radial (ER) configuration without twist. In TER configurations, the twist direction can change as well. All of the hedgehogs we observed in the TER system were heterochiral, *i.e.*, they exhibited a handedness inversion in which twist direction changed from one side of the defect to the other. Interestingly, we never observed a homochiral

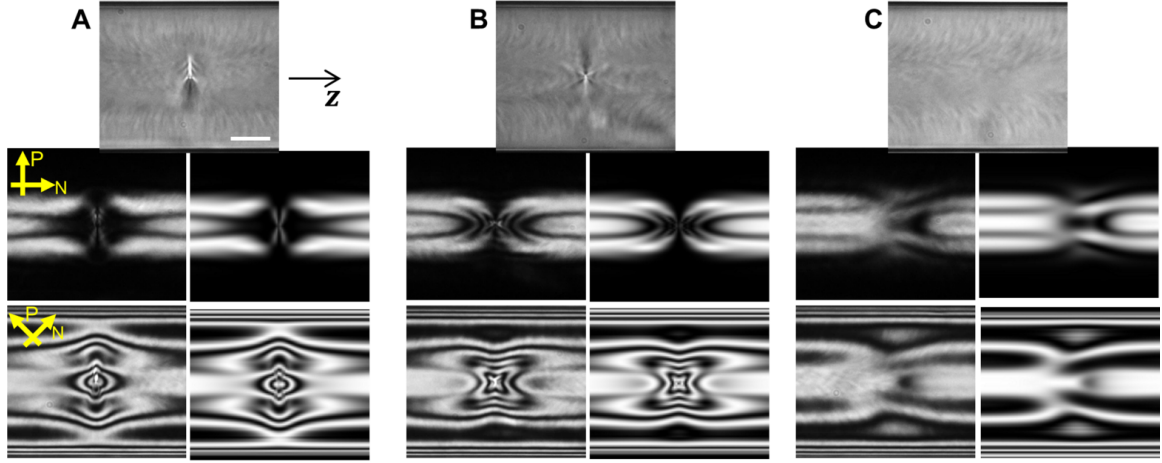


Figure 2.10: Optical microscopy (bright-field and POM) images of defects and simulated patterns of corresponding defects that arise when nematic SSY is placed in the cylinder;  $z$  is parallel to the cylindrical axis of the capillary. The concentration and the temperature of the SSY are 31.5% (wt/wt) and 25.0 °C, respectively. The pass axis directions of the polarizer (P) and analyzer (N) are shown as yellow arrows. (Top) Bright-field microscopy images and (Middle and Bottom) POM images with two different directions of crossed polarizers of (A) a radial defect, (B) a hyperbolic defect, and (C) a twist domain wall. Middle Left and Bottom Left show the experimental images taken under monochromatic illumination (wavelength = 650 nm), and Middle Right and Bottom Right correspond to POM patterns simulated by Jones matrix calculations of director-field models. (Scale bar: 25  $\mu\text{m}$ .)

hedgehog bounded by domains of the same handedness. This absence was surprising, especially considering the degeneracy of both the handedness and escape direction in the TER configuration. Fig. 2.11A and 4B show representative images of the observed radial and hyperbolic defects under crossed polarizers and a full-wave plate. Notice, their right- and left-end regions do not match after a 180-degree rotation of either region, which indicates that the regions have the opposite handedness.

Why are singular defects of the same handedness absent? To explore this question, we studied how defects form in response to changes in temperature and thermodynamic phase of SSY in the capillary. To this end, the temperature of 31% (wt/vol) nematic SSY in the capillary was increased to 52°C in order to melt the LC into the fully isotropic phase. Then the temperature was slowly decreased, and the sample evolved through the isotropic-nematic coexistence phase to 38°C, the point at which the SSY became a fully nematic phase. The coexistence phase is shown in Fig. 4D, wherein we observe cylindrical nematic LC domains

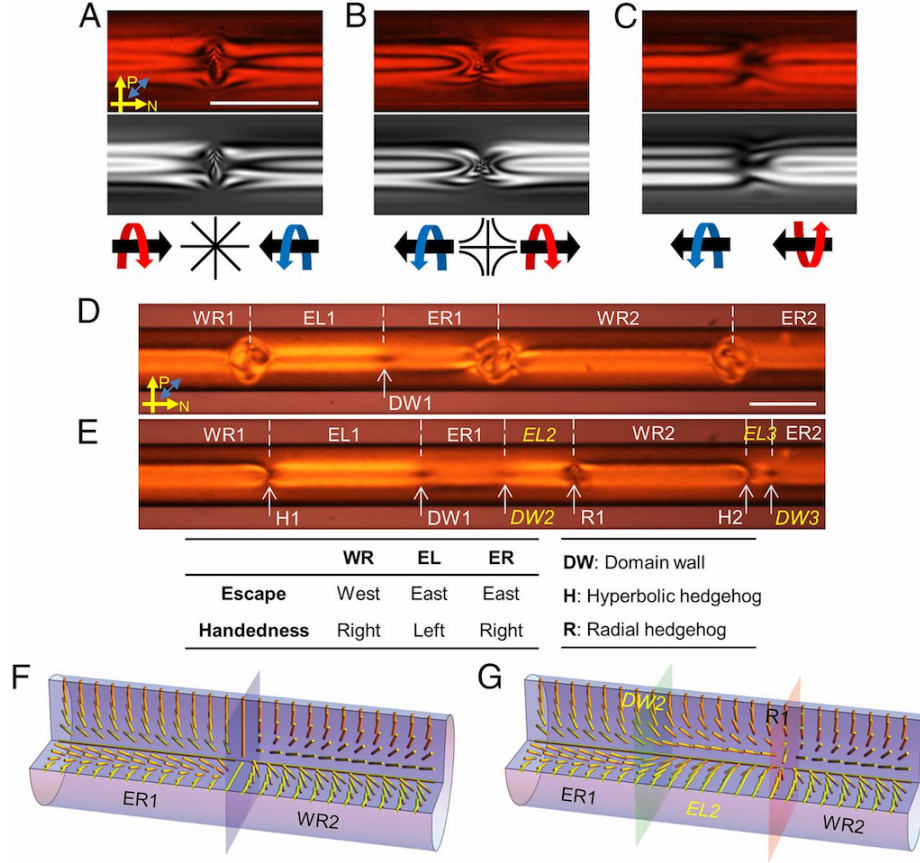


Figure 2.11: Chirality of nematic SSY defects in a cylinder. The pass axis directions of a polarizer (P) and an analyzer (N) are shown as single-headed yellow arrows, and the slow axis of the wave plate is shown as a double-headed blue arrow. (Top) POM images taken between crossed polarizers and a full-wave plate under monochromatic illumination (wavelength = 650 nm), (Middle) the corresponding simulated POM patterns, and (Bottom) schematic diagrams of (A) a radial defect, (B) a hyperbolic defect, and (C) a domain wall. The concentration and temperature of the SSY are 31.5% (wt/wt) and 25.0 °C, respectively. In the schematic diagrams, thin black lines depict director configurations around the singular defects. Thick straight arrows and rotating arrows represent escape directions and handedness, respectively (blue, left-handedness; red, right-handedness). (D and E) POM images of 31% (wt/wt) SSY in a capillary at (D) 40 °C and (E) 38 °C under polychromatic illumination. White dashed lines separate nematic domains, and each nematic domain is labeled with the escape direction of the LC directors [*i.e.*, to the east (E) or west (W)], the handedness of the twist is labeled right-handed (R) or left-handed (L), and the number indicates whether the domain is first, second, third, etc. for each type of domain starting from the left. East (west) corresponds to a direction toward  $z > 0$  ( $z < 0$ ) (Fig. 2.8). For example, the WR1 domain is the first (*i.e.*, 1; starting from the left) right-handed domain for which LC directors escape toward the west direction. Hyperbolic defects (Hs), radial defects (Rs), and domain walls (DWs) are labeled in a similar way and marked by white single-headed arrows. The table specifies the meanings of the abbreviations. Note that three isotropic-phase droplets separate the nematic domains in D, where SSY is in a nematic-isotropic coexistence phase. (F and G) Schematic diagrams of (F) a radial defect of the same handedness and (G) a radial defect of the opposite handedness with a domain wall. Yellow rods represent LC directors, and the labels correspond to those in D and E. (Scale bar: 100  $\mu\text{m}$ .)

of finite length separated by spherical domains of isotropic phase. By applying a slow cooling rate of approximately  $0.5^{\circ}\text{C}/\text{min}$  and providing enough relaxation time ( $\sim 5$  min) for the sample at each measurement temperature<sup>2</sup>, we ensured that each separated nematic domain adopted its own equilibrium configuration. As a result, the nematic domains in Fig. 2.11D have TER configurations with independent escape directions and independent twisting handedness. For clarity we label each nematic domain with the escape direction of the LC directors, *i.e.*, to the East (E) or to the West (W); we label the handedness of the twist as right-handed (R) or left-handed (L); and we use a numerical index as an identifier. East (West) corresponds to the escape direction toward  $z > 0$  ( $z < 0$ ) in Fig. 2.9A and C. The WR1 domain, for example, is the first (*i.e.*, 1, starting from the left) right-handed domain for which LC directors escape toward the West. Hyperbolic defects (H), radial defects (R), and domain walls (DW) are labeled in a similar way.

Our observations of defect formation demonstrates that heterochiral hedgehogs are favored over homochiral ones. As the temperature was decreased into the coexistence regime, the nematic domains grew to replace the isotropic domains. Eventually, as shown in Fig. 2.11E, when the isotropic domains disappeared, the nematic domains merged and formed defects according to the escape directions and twisting handedness of the merging domains. For example, the WR1 and EL1 domains in Fig. 2.11E formed a hyperbolic defect, H1, because the WR1 domain escaped towards the West and the EL1 domain towards the East. Additionally, the handedness of the twist deformation changed across the H1 defect; the WR1 domain is right-handed and the EL1 domain is left-handed, and this handedness inversion is consistent with observations in Fig. 2.11B. By contrast, the ER1 and WR2 domains did not create a radial defect of the same handedness, shown as Fig. 2.11F; rather they created a heterochiral radial defect (R1) and a domain wall (DW2) shown in Figs. 2.11E and 2.11G. This domain wall creation also arose between WR2 and ER2 domains as shown in Fig. 2.11E.

---

<sup>2</sup>When the cooling rate was fast, thermally induced flow aligned the nematic SSY and initially led to formation of a single nematic domain without twist and without singular defects. Thereafter, the mirror symmetry of the domain was broken, and many domain walls at random positions were created but still no singular defects; in this case, the sample had only one escape direction.

Numerical calculations of chiral defects' equilibrium director configurations and their elastic free energies reveal that the heterochiral singular defects are energetically favored over homochiral ones. In Figs. 2.10 and 2.11 A-C, these numerically computed director configurations and their associated optical textures calculated by Jones matrices successfully reproduced optical textures of all three types of defects. Furthermore, the numerical calculations enabled us to compare the elastic free energies of the defects in Fig. 2.12A. Specifically, we calculated differences ( $\Delta F_1$  in Fig. 2.12A) between the total elastic free energy of each defect ( $F_{\text{Defect}}$ ) and that of the TER configuration ( $F_{\text{TER}}$ ); these free energy differences are normalized by  $\pi RK$ , where  $R$  is the radius of the cylinder and  $K$  is the splay modulus. In addition, we calculated the difference in energy ( $\Delta F_2 = F_{\text{Heterochiral+Domainwall}} - F_{\text{Homochiral}}$ ) between the combination of a heterochiral defect and a domain wall and an isolated homochiral defect. Fig. 2.12B illustrates the results of this calculation along with the individual contributions to this energy difference from splay, twist, and bend distortions.

Notice, the combined energy of a heterochiral defect and a domain wall is lower than the energy of an isolated homochiral defect. Thus, an isolated homochiral radial (hyperbolic) defect can lower its energy by splitting into a heterochiral radial (hyperbolic) defect and a domain wall, in the process lowering its splay elastic free energy with a only a slight decrease in its twist energy and a slight increase in its bend energy. As shown in Fig. 2.13, this splay energy cancellation can be understood visually by studying the director in the planes of the singular defects. These results explain why singular defects choose to be heterochiral, creating an additional domain wall if necessary to satisfy the boundary conditions, and why a domain wall between two heterochiral defects is energetically stable and does not combine with either of the defects to create a homochiral one. Note also, although the hyperbolic defect costs less energy than the TER configuration does, the sum of the energies of a radial-hyperbolic defect pair is always greater than the energy of the TER configuration, as expected.

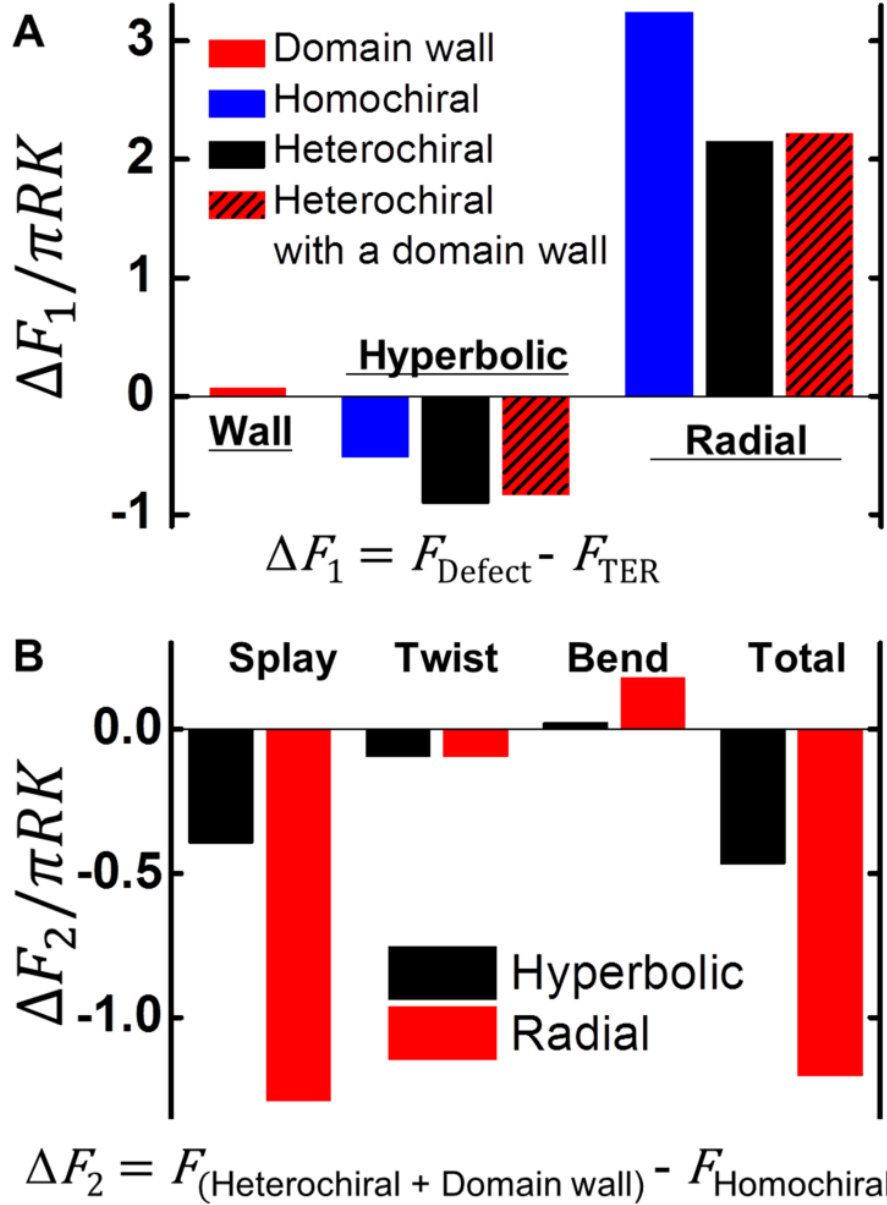


Figure 2.12: Energetics of the chiral defects. Elastic free energies ( $F$ ) are normalized by  $\pi R K$  to be unitless;  $R$  is the radius of the cylinder.  $K = K_1$  with  $K_1 : K_2 : K_3 = 1 : 0.09 : 1$ , which approximates the elastic constants of 31.5% (wt/wt) SSY at 25.0 °C. (A) Differences ( $\Delta F_1$ ) between the normalized total elastic free energy of each defect ( $F_{\text{Defect}}$ ) and the TER configuration ( $F_{\text{TER}}$ ). (B) Differences ( $\Delta F_2$ ) between the normalized splay, twist, bend elastic free energies, and their sum of a heterochiral hyperbolic (radial) defect with a domain wall ( $F_{\text{Heterochiral}+\text{Domainwall}}$ ) and a homochiral hyperbolic (radial) defect ( $F_{\text{Homochiral}}$ ).

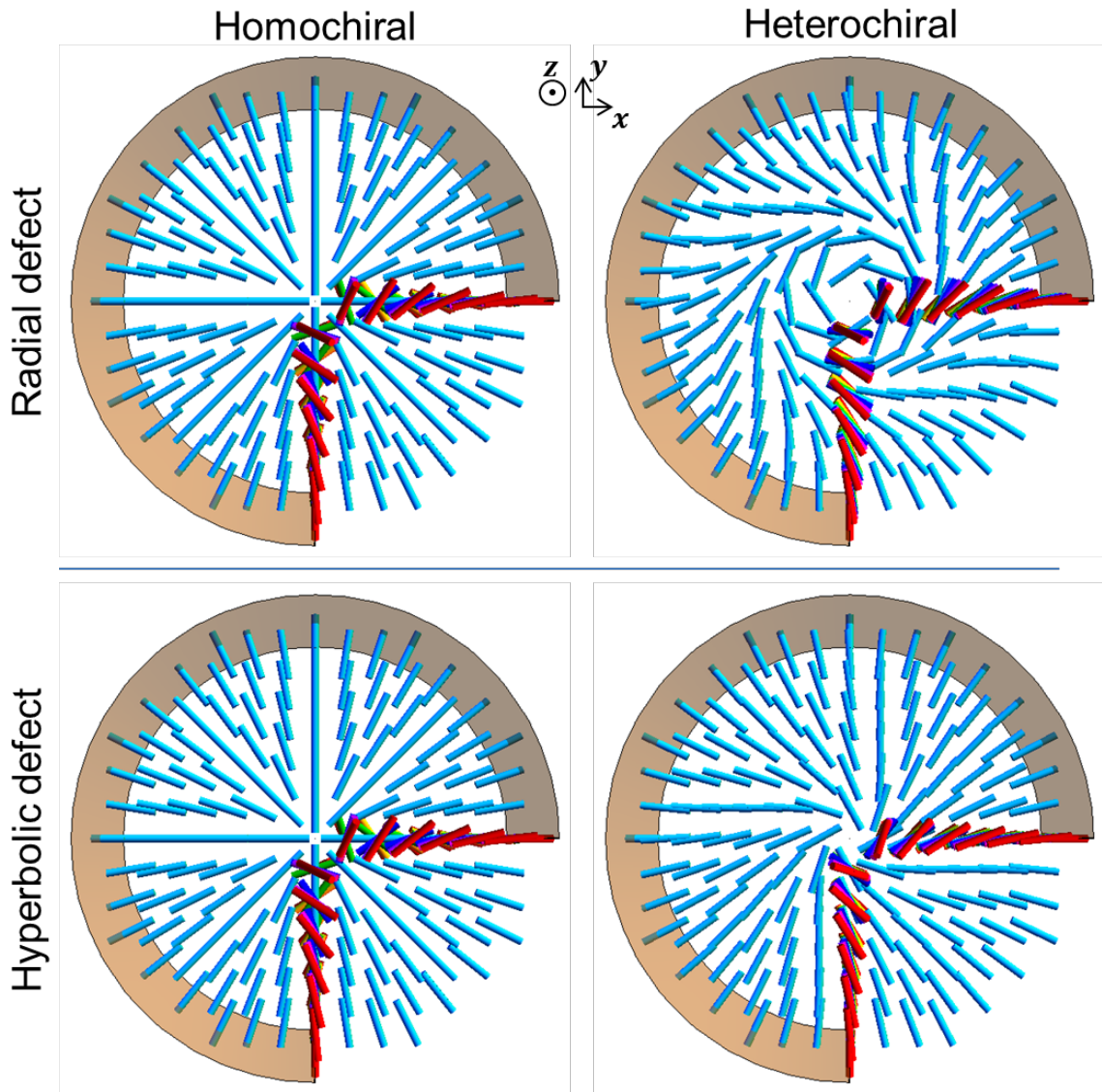


Figure 2.13: Schematic diagrams of the (Upper) radial and (Lower) hyperbolic defect configurations of (Left) homochirality and (Right) heterochirality near the defect plane. Colored rods correspond to nematic directors, and the directors in the defect plane ( $z = 0$ ) are shown in the all quadrants. Clearly, homochiral defects exhibit pure splay deformation within their defect planes, whereas heterochiral defects replace the costly splay deformation within the defect plane with some bend deformation. The overlapping directors on the positive  $x$  axis and the negative  $y$  axis show how the directors twist along the  $z$  axis passing through the defect plane ( $z = 0$ ), where different colors represent different  $z$  positions. The heterochiral defects have less twist deformation (*i.e.*, more parallel directors) than the homochiral defects.

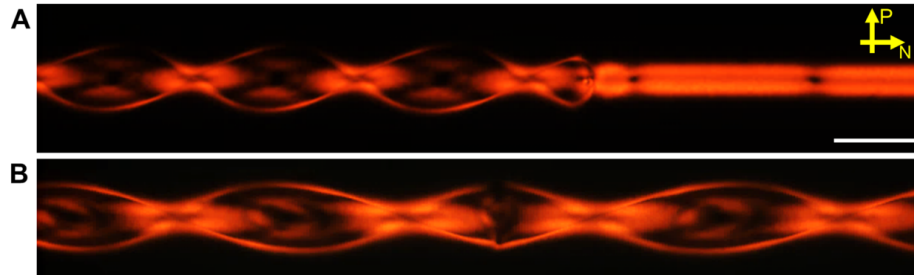


Figure 2.14: POM images of nematic SSY with a double helix of disclinations in a cylinder under polychromatic illumination. The concentration and temperature of the SSY are 30.0% (wt/wt) and 23 °C, respectively. Yellow arrows correspond to the pass axis directions of the polarizer (P) and the analyzer (N). (A) A twisted planar-polar configuration (left side) replacing the TER configuration (right side). Two dark spots in the TER configuration correspond to domain walls. (B) A domain wall (center of the image) between two double helices with opposite chirality. (Scale bar: 100  $\mu\text{m}$ .)

#### 2.4.4 Twisted Helical Configuration

Lastly, we report on an exotic chiral director configuration with a double helix of disclinations. These configurations were observed in the same nematic SSY LC samples confined to the cylinder. As shown in Fig. 2.14A, the TER configuration on the right side is replaced by a double helix of disclinations slowly growing from the left side at an approximate speed of 500  $\mu\text{m}$  per hour. After injection of nematic SSY into capillaries, all nematic SSY samples had the TER configuration at 25 °C (with or without heating and cooling through the isotropic phase). This TER configuration was stable at least for a day in most capillaries. While the sealed capillaries were stored at room temperature, the double helices nucleated at arbitrary positions in the capillaries, albeit often at their ends, and they then started to grow. Because both right-handed and left-handed helices are allowed, domain-wall-like defects shown in Fig. 2.14B sometimes formed. The approximate range of the pitch of the helices was from five to ten times the cylinder diameter. Because the pitch varied considerably even within a single capillary, it was difficult to characterize the pitch and to find a relation to its capillary size and the properties of nematic SSY.

We suggest that this configuration with a double helix is a twisted planar-polar configuration schematically shown in Fig. 2.15. We hypothesize that a planar-polar configuration, with homeotropic boundary conditions and two straight surface disclinations parallel to the

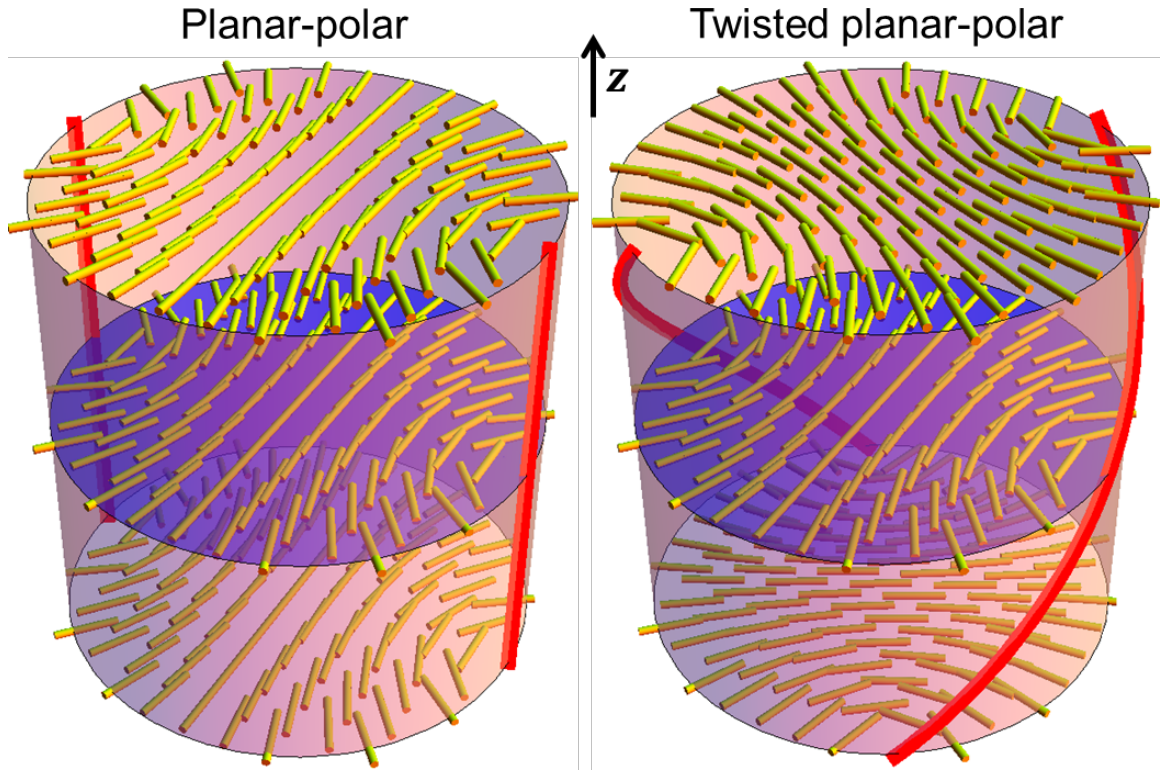


Figure 2.15: POM images of nematic SSY with a double helix of disclinations in a cylinder under polychromatic illumination. The concentration and temperature of the SSY are 30.0% (wt/wt) and 23 °C, respectively. Yellow arrows correspond to the pass axis directions of the polarizer (P) and the analyzer (N). (A) A twisted planar-polar configuration (left side) replacing the TER configuration (right side). Two dark spots in the TER configuration correspond to domain walls. (B) A domain wall (center of the image) between two double helices with opposite chirality. (Scale bar: 100  $\mu\text{m}$ .)

cylindrical axis, can twist to lower its elastic free energy (again due to the small twist modulus of nematic SSY). Note that a similar configuration was reported in the chiral nematic phase near its transition point to smectic-A phase [144], while this double helix of disclinations exists in an achiral nematic phase far from any phase transition points. It appears implausible that changes in SSY took place during storage to cause these transitions, *e.g.*, a slight increase in concentration despite sealing of the capillaries, or a degradation of the homeotropic alignment layer. Indeed, heating and cooling of all the nematic SSY samples recovered the TER configuration, but this was eventually followed by another conversion to the twisted planar-polar configuration with a double helix.

Although suggestive, at this time we cannot determine whether this configuration with

a double helix is a true ground state for nematic SSY in a cylinder; further investigation is required. According to Crawford et al. [154], the energetics of this transition could be related to the saddle-splay modulus ( $K_{24}$ ) of nematic SSY and a finite anchoring strength of the alignment layer. For instance, a weak anchoring strength permits considerable deviation from a radial orientation near the cylindrical capillary wall and can, therefore, facilitate formation of surface disclinations as we see in the twisted planar-polar configuration with a double helix. Another possibility may be that the SSY molecules at the parylene surface are trapped in a metastable state before relaxing to an orientation that promotes the double helix configuration. The saddle-splay modulus of nematic SSY and the anchoring strength at the SSY-parylene interface are not known, and we expect that characterization of these properties will be essential for understanding the twisted planar-polar configuration with a double helix.

## 2.5 Conclusions and Future Work

We have explored spontaneous mirror symmetry breaking and rich phenomena involving chiral defects in the achiral nematic LCLC, SSY, confined to spherical droplets with planar anchoring and cylindrical capillaries with homeotropic anchoring. Despite the absence of intrinsic chirality, nematic SSY produces twisted- and escaped-radial (TER) configurations with two degenerate directions for both twisting and escape. These configurations were explained theoretically using elastic free-energy models that include the giant elastic anisotropy of nematic SSY. In the case of capillaries, these degeneracies lead to chiral defects: domain walls separating domains of opposite twist handedness, and radial and hyperbolic hedgehogs. Interestingly, the radial and hyperbolic defects separate only domains of opposite handedness, and our numerical calculations of elastic free energies reveal their energetic selection. Lastly, in the same system, we report another remarkable mirror-symmetry-broken configuration with a double helix of disclinations which could be the true ground-state of the system. We presume that the helix formation also results from the very small twist elastic modulus compared to the other moduli, and that the energetics of the

transition from the TER configuration to the twisted planar-polar configuration is closely related to the saddle-splay modulus and a finite anchoring strength, but more investigation is needed.

Further study of LCLCs in a cylindrical geometry will enable us to investigate unexplored properties of LCLCs such as the saddle-splay modulus [29, 155], and also to develop applications utilizing chiral structures. For example, we should be able to study chiral amplification by splitting the chiral degeneracy or by imprinting a certain handedness [156, 157]. In a different vein, application of various classes of external fields, or addition of a small amount of chiral dopant, might induce a “sergeants and soldiers” type of behavior wherein a small energetic preference for one handedness over another tips the balance [60, 69, 79, 80]. Finally, defect-free configurations of a single handedness may have applications for reconfigurable optical components and devices with optical rotatory power.

## 2.6 Appendix: Numerical Calculation of Elastic Free Energy In Droplets

We numerically integrated the elastic free-energy density  $f$  of the model director field  $\mathbf{n}_{tb}$  over a droplet using Mathematica. The radius of the droplet is normalized to 1. It is known that the saddle-splay term related to  $K_{24}$  does not contribute to the energetics of the LC droplet with a strong planar anchoring condition. The energy  $F$  and energy density  $f$  are

$$F = \int_0^{2\pi} d\phi \int_{-1}^1 dz \int_0^{\sqrt{1-z^2}} \rho df \quad (2.6.1)$$

$$f = \frac{1}{2} \left\{ K_1 (\nabla \cdot \mathbf{n}_{tb})^2 + K_2 (\mathbf{n}_{tb} \cdot \nabla \times \mathbf{n}_{tb})^2 + K_3 (\mathbf{n}_{tb} \times \nabla \times \mathbf{n}_{tb})^2 \right\} \quad (2.6.2)$$

We follow Xu and Crooker [129] and Xu et al. [115] by assuming a simplified director field for the twisted bipolar configuration  $n_{tb}$  that combines the bipolar configuration  $n_b$  and the concentric configuration  $n_c$  through  $n_{tb} = n_b \cos(\alpha) + n_c \sin(\alpha)$  and  $\alpha = \alpha_0 \rho / \rho_0$ , where  $\rho$

is a radius in cylindrical coordinates, the  $z$  axis is along the bipole axis, and  $\rho_0 = \rho(1-z^2)^{1/2}$  is the maximum value of  $\rho$  for a given  $z$ . Then, we use the director field models for the bipolar and concentric configurations of Ding and Yang [114]. This is the same simplified director field for the twisted bipolar configuration used in the Jones matrix calculation. The model director fields are described by Eq. 2.6.3 in the cylindrical coordinates  $(\rho, \phi, z)$ .

$$n_b = \left\{ -\frac{z\rho}{\sqrt{z^2\rho^2 + (1-z^2)^2}}, 0, \frac{1-z^2}{\sqrt{z^2\rho^2 + (1-z^2)^2}} \right\} \quad (2.6.3)$$

$$n_c = \{0, 1, 0\} \quad (2.6.4)$$

$$n_{tb} = \left\{ -\frac{z\rho \cos \frac{\alpha_0\rho}{\sqrt{1-z^2}}}{\sqrt{z^2\rho^2 + (1-z^2)^2}}, \sin \frac{\alpha_0\rho}{\sqrt{(1-z^2)^2}}, -\frac{(1-z)^2 \cos \frac{\alpha_0\rho}{\sqrt{1-z^2}}}{\sqrt{z^2\rho^2 + (1-z^2)^2}} \right\} \quad (2.6.5)$$

To evaluate the free energy of the twisted bipolar configuration, we used  $z \rightarrow -z$  symmetry to reduce the region of integration and introduced a change of variables from cylindrical coordinates  $\rho$  and  $z$  to variables  $s$  and  $v$  defined via  $\rho^2 = s^2(1-(1-v^2))$  and  $v = (1-z^2)^{1/2}$ .  $v = 0$  corresponds to the North Pole site of the upper-half plane Boojum. The expressions for the splay and bend energy densities in terms of these variables are clearly analytic throughout the region of integration, allowing easy numerical evaluation of the total splay and bend energies shown in Fig. 2.3. The twist energy density on the other hand diverges as  $v \rightarrow 0$ .  $f_{\text{twist}} \sim 2\pi s^2 \alpha_0^2 / v$ , leading to a logarithmic energy singularity near  $z = 1$  that requires the integration range to be limited to  $0 < z < 1 - \Delta z_{\text{cutoff}}$ . The total twist energy is then

$$F_{\text{twist}} = -\frac{1}{2} K_2 \alpha_0^2 \ln \sqrt{1 - (1 - \Delta z_{\text{cutoff}})^2} + F_{\text{twist}|_{\text{regular}}}, \quad (2.6.6)$$

where  $F_{\text{twist}|_{\text{regular}}}$  is the nonsingular part of the energy, which can be evaluated numerically. To derive the results shown in Fig. 2.3, we used  $\Delta z_{\text{cutoff}} = 0.001$  when the normalized radius is 1. For example, this 0.1%  $z$  cutoff corresponds to 20 nm in a droplet of 40  $\mu\text{m}$  diameter; 20 nm is known to be of the same order of the persistence length of the SSY aggregate [20]. We also checked that  $\alpha_0$  at the minimum elastic free energy is not significantly sensitive to

this cutoff to the singular part of the twist elastic free energy. For example, changing from 0.1 to 1.0%  $z$  cutoff increases  $\alpha_0$  by only about  $5^\circ$ .

## Chapter 3

# Chiral Structures and Defects of Lyotropic Chromonic Liquid Crystals Induced by Saddle-Splay Elasticity<sup>1</sup>

### 3.1 Introduction

The elastic properties of nematic liquid crystals (LCs) are crucial for liquid crystal display applications [130, 158], and they continue to give rise to unanticipated fundamental phenomena [1, 2, 10, 159–162]. Three of the bulk nematic LC deformation modes, splay, twist and bend, are well known and have associated elastic moduli  $K_1$ ,  $K_2$  and  $K_3$ , respectively. These moduli have been intensely studied because they are easy to visualize, and because it is possible to independently excite the modes via clever usage of sample geometry [21, 163, 164], LC boundary conditions [90, 165], and external fields [20, 166]. As a result, these moduli have been measured for a variety of thermotropic and lyotropic LCs [20, 21, 32, 167–169].

---

<sup>1</sup>This chapter is adapted from reference [3].

By contrast, a much less studied fourth independent mode [28, 170, 171] of elastic deformation in nematic LCs can exist; it is called saddle-splay. Saddle-splay is hard to visualize and to independently excite [171, 172]. Moreover, the energy of this deformation class can be integrated to the boundary, so that the mode does not appear in the Euler-Lagrange equations, and with fixed boundary conditions (*i.e.* a fixed orientation of the nematic director at boundaries), the saddle-splay energy will have no effect on the LC director configuration. Even with free boundary conditions, the saddle-splay energy will not affect the bulk LC configuration unless the principal curvatures of the surface are different, *i.e.*, saddle-splay effects are not expected for spherical or flat surfaces. Thus, although much progress in understanding saddle-splay has been made [173, 174], especially with thermotropic nematic LCs, unambiguous determination of saddle-splay energy effects on liquid crystal configurations and measurement of the saddle-splay elastic modulus,  $K_{24}$ , remain difficult [33].

While the bulk elastic constants described above strongly influence LC director configurations, LC boundary conditions at material interfaces also influence bulk structure. Indeed, considerable effort has gone into development of surface preparation techniques to produce particular bulk director configurations [39, 165, 175–179]. The saddle-splay term integrates to the boundary and effectively imposes boundary conditions at free surfaces favoring director alignment along the direction of most negative surface curvature for positive  $K_{24}$  [102] and outwardly pointing surface normals<sup>2</sup>. For this effect to be present, the director cannot be held perpendicular to the surface (*i.e.*, the boundary conditions cannot be homeotropic), as was the case in our prior work [2]. The potential role of saddle-splay effects in determining bulk director configurations by spontaneous symmetry breaking has been appreciated [69, 101, 154, 165] but has been difficult to fully characterize; generally, molecular surface forces can impose preferred boundary conditions that are hard to disentangle from effects due to  $K_{24}$  [140, 151]. As a result, the measurements of  $K_{24}$  to date have wide confidence intervals [29, 101, 155] and even vary in sign [29]. Finally, additional

---

<sup>2</sup>This was corrected in an erratum [180].

factors that have complicated assignment of saddle-splay effects are the so-called Ericksen inequalities [181] that require  $0 < K_{24} < 2K_2$  and  $K_{24} < 2K_1$ . These inequalities were derived assuming spatially uniform gradients of the director. They do not, however, apply in geometries such as ours in which the director gradients are not uniform.

In this contribution, we investigate director configurations of the nematic lyotropic chromonic liquid crystal (LCLC) Sunset Yellow (SSY) confined within cylindrical glass capillaries with degenerate planar boundary conditions as initially reported in references [182–184]. Our study employs a combination of polarized optical microscopy, measurements of director-field thermal fluctuations, and Frank-free-energy calculations to rationalize the observed structures. Importantly, we show that a large  $K_{24}$  leads to an escaped-twist (ET) ground state, which exhibits a classic double-twist configuration. Note, chiral symmetry breaking in the ET configuration is fundamentally different from symmetry breaking in other LCLC systems with uniform principal curvatures [1], or with homeotropic boundary conditions [2]. In the previous work, spontaneous twist deformation arises because  $K_2$  is much smaller than  $K_1$  and  $K_3$ ;  $K_{24}$  played no role in the energetics. In the present work,  $K_{24}$  is important in the energetics, and comparison of theory and experiment enables us to measure  $K_{24}$  for the first time in a LCLC. We find a value of  $K_{24}/K_2 = 55.0$ , which strongly violates the Ericksen inequalities. Finally, we observe and characterize chiral hedgehog point defects separating chiral domains of opposite handedness. Interestingly, the presence of point defects rather than smooth domain walls also provides precise quantitative information about  $K_{24}$  that is consistent with our other conclusions.

## 3.2 Theoretical Background of Frank Elastic Free Energy and Saddle-Splay

Before discussing the experimental results, we formulate the theoretical problem. We assume the achiral nematic LCLC is described by a Frank free energy, *i.e.*,

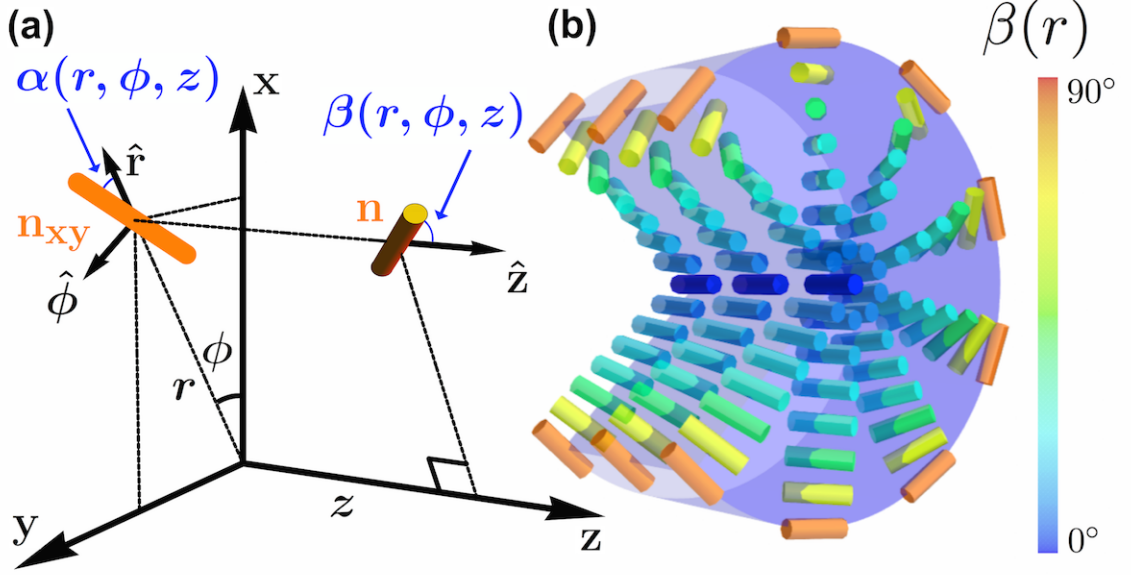


Figure 3.1: **(a)** Coordinate system used for director configuration and defect energy calculations. The director  $\mathbf{n}$  is described by the angle  $\alpha$  between the director projection  $\mathbf{n}_{xy}$  and  $\hat{\mathbf{r}}$ , and by the angle  $\beta$  between  $\mathbf{n}$  and the capillary axis, which is parallel to  $\hat{\mathbf{z}}$ . **(b)** 3D cutaway view of the capillary and the ground state director field using  $K_2/K_3 = 0.1$ , and  $K_{24}/K_3 = 4.6$ , which approximates the Frank moduli of 30 % wt./wt. SSY at 25°C. Notice the large twist angle at the capillary surface close to 90°.  $\alpha$  is independent of position and  $\beta$  depends on only the radial coordinate  $r$ . This configuration has right-handed chirality.

$$F = \int d^3\mathbf{x} \left[ \frac{1}{2}K_1 (\mathbf{n} \cdot \nabla \cdot \mathbf{n})^2 + \frac{1}{2}K_2 (\mathbf{n} \cdot \nabla \times \mathbf{n})^2 + \frac{1}{2}K_3 (\mathbf{n} \times \nabla \times \mathbf{n})^2 - \frac{1}{2}K_{24} \nabla \cdot (\mathbf{n} \times \nabla \times \mathbf{n} + \mathbf{n} \nabla \cdot \mathbf{n}) \right], \quad (3.2.1)$$

where  $\mathbf{n}$  is the nematic director. Equation (3.2.1) explicitly includes the saddle-splay term with modulus  $K_{24}$ , which can in principle be mimicked by a surface anchoring term that is coupled to surface curvature; thus we consider a saddle-splay term that combines the two effects [185]. This possibility is explored below in section 3.5. A Rapini-Papoular type surface anchoring term with in-plane anisotropy [28, 140] is excluded and discussed later in the text.

The LC is contained inside a capillary of radius  $R$  and cylindrical coordinates are used

to parameterize its director field,  $\mathbf{n}$ , with  $\hat{\mathbf{z}}$  along the capillary axis (see Fig. 3.1), *i.e.*,

$$\mathbf{n} = \cos \alpha \sin \beta \hat{\mathbf{r}} + \sin \alpha \sin \beta \hat{\boldsymbol{\phi}} + \cos \beta \hat{\mathbf{z}}. \quad (3.2.2)$$

To determine the configuration of the ground state, we assume the director depends only on  $r$  and minimize the Frank free energy with respect to  $\alpha(r)$  and  $\beta(r)$ . Note, the director  $\mathbf{n}$  is therefore characterized by the angle  $\alpha$  between the director projection  $\mathbf{n}_{xy}$  and  $\hat{\mathbf{r}}$ , and by the angle  $\beta$  between  $\mathbf{n}$  and the capillary axis, which is parallel to  $\hat{\mathbf{z}}$ . Degenerate planar anchoring conditions at the capillary surface prevent the director from having an  $\hat{\mathbf{r}}$ -component, so  $\alpha(r = R) = \pi/2$ . Cylindrical symmetry sets  $\beta(r = 0) = 0$ . Both  $\alpha(r = 0)$  and  $\beta(r = R)$  are free to vary, but stationarity of the free energy provides the boundary conditions:  $\partial_r \alpha(r = 0) = 0$  and  $R \partial_r \beta(r = R) = (\frac{K_{24}}{2K_2} - \frac{1}{2}) \sin 2\beta(r = R)$ .

With these boundary conditions, the Euler-Lagrange equations of the Frank free energy give [140]

$$\alpha(r) = \frac{\pi}{2}; \quad (3.2.3)$$

$$\beta(r) = \arctan \frac{2\sqrt{K_2 K_{24}(K_{24} - 2K_2)}r/R}{\sqrt{K_3}[K_{24} - (K_{24} - 2K_2)r^2/R^2]}. \quad (3.2.4)$$

This ET solution exists for  $K_{24} > 2K_2$  and has right-handed chirality, *i.e.*, the director streamlines form right-handed helices. A mirror-image solution  $\beta(r) \rightarrow \pi - \beta(r)$  exists with the same energy. Notice that the radial position  $r$  is scaled by the cylinder radius  $R$  and that  $K_1$  does not appear because this configuration has no splay.

If  $K_{24} < 2K_2$ , then only the trivial  $\beta(r) = 0$  solution exists, which corresponds to the simple parallel-axial configuration [154]. As  $K_{24}$  surpasses  $2K_2 \equiv K_c$ , which is exactly the upper bound found by Ericksen, the system spontaneously breaks mirror symmetry, and an ET configuration of one handedness grows continuously from the trivial solution.  $\beta_1 = \beta(r = R)$  is plotted in Fig. 3.2. Prior work with thermotropic LCs has found this ET configuration when an azimuthal anchoring condition dominates the behavior of  $\beta_1$  at the

capillary surface through a chemical or mechanical treatment of the surface [140, 148, 151]. Note that  $\beta(r)$  (Eq. 3.2.4) can only be approximated by a linear twist model [102] for certain ratios of elastic constants. For LCs whose elastic moduli do not satisfy these ratios, such as SSY (our case!), then polarized optical microscopy textures are strongly affected by the nonlinear behavior of  $\beta(r)$ ; *i.e.*, the linear twist approximation is poor.

The normalized free energy of the ET configuration is readily calculated to be

$$\begin{aligned} \frac{F}{\pi L} = & - (K_{24} - 2K_2) \\ & + \frac{\sqrt{K_2 K_3}}{\sqrt{K_3 - K_2}} \arctan \frac{\sqrt{K_3 - K_2}(K_{24} - 2K_2)}{\sqrt{K_2}(K_3 + K_{24} - 2K_2)}, \end{aligned} \quad (3.2.5)$$

where  $L$  is the length of the capillary. Notice that as  $K_{24}$  increases beyond  $2K_2$ , the free energy decreases continuously from 0, thereby confirming that the ET configuration as a ground state is preferred over the uniform configuration whenever it can exist;  $K_{24} = 2K_2$  marks a second-order phase transition line. The key to this energetic stabilization is the saddle-splay term:

$$\frac{F_{24}}{\pi L} = -K_{24} \sin^2 \beta_1. \quad (3.2.6)$$

As noted by Ref. [102], which uses the same surface normal convention,  $F_{24}$  accounts for the coupling of the nematic director to the surface curvature tensor and favors director alignment in the direction of most negative curvature for  $K_{24} > 0$  [180]. In our case, this is the azimuthal direction along the circumference of the capillary. Alternatively, we can understand this from considering the saddle-splay term of equation 3.2.1, which can be rewritten as a surface term using the divergence theorem:

$$F_{24} = -\frac{K_{24}}{2} \int d\mathbf{S}^2 (\mathbf{n} \times \nabla \times \mathbf{n} + \mathbf{n} \nabla \cdot \mathbf{n}). \quad (3.2.7)$$

The second term in 3.2.7 is 0 because of the planar boundary conditions. The remaining

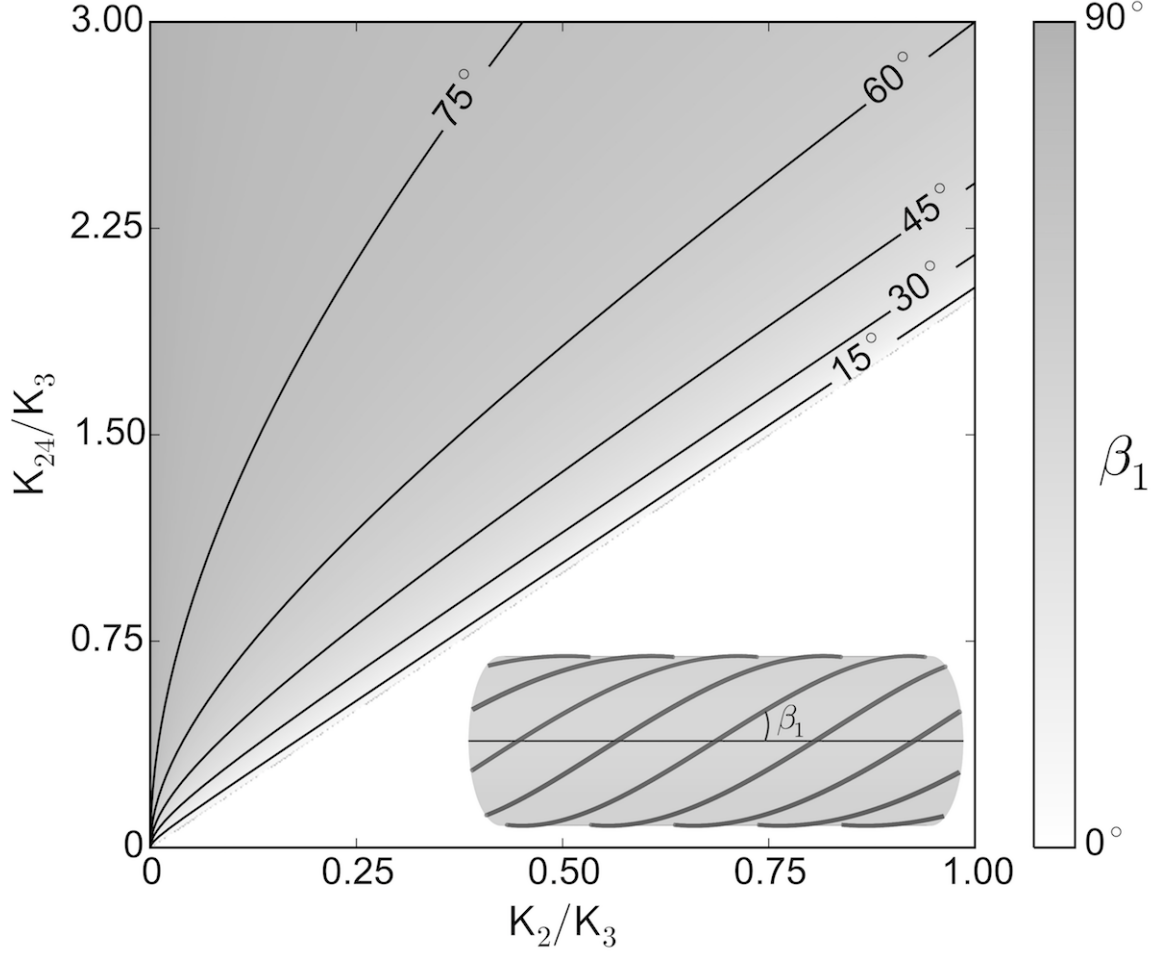


Figure 3.2: Phase diagram of  $\beta_1$ , the angle between the nematic director and capillary axis at the capillary surface, as a function of elastic moduli ratios of saddle-splay ( $K_{24}$ ) to twist ( $K_2$ ) and bend ( $K_3$ ). Inset: an example capillary with streamlines indicating a surface director field at angle  $\beta_1$  with left-handed chirality.

term,

$$F_{24} = -\frac{K_{24}}{2} \int dS^2 (\mathbf{n} \times \nabla \times \mathbf{n}), \quad (3.2.8)$$

has a form similar to the bend term of Frank elastic energy. For positive  $K_{24}$  and because of the leading negative sign, a maximal bend at the capillary surface minimizes the saddle-splay energy contribution. Thus, the saddle-splay free energy stabilizes the ET configuration despite introducing bulk director distortion. We also have verified that both the ET and the deformation-free solutions are stable whenever they are preferred ( $K_{24} > 2K_2$  and  $K_{24} < 2K_2$ , respectively); that is, their stability matrices have positive eigenvalues.

### 3.3 Experimental Methods of Measuring Escaped-Twisted Configuration

Our experimental investigations again used nematic SSY, a LCLC with relatively low twist modulus  $K_2/K_3 \approx 0.1$  [20]. Briefly, five SSY samples were loaded into five different capillary tubes with diameters  $100 \mu\text{m} \pm 10\%$ , from VitroCom (CV1017-100). The sealed samples were illuminated between cross-polarizers by 10nm-bandpass-filtered 660 nm LED light at high (160x) magnification, enabling small depth of field and high spatial resolution imaging. Images were captured by a Uniq UP680-CL video camera, and a piezo-objective positioner was moved to image focal planes within the samples in  $1 \mu\text{m}$  intervals.

The capillaries without surface treatment were loaded with SSY and sealed to prevent evaporation. A critical experimental question for any saddle-splay study concerns possible structure on the cylinder interfaces that could induce a preferred anchoring direction. To this end, we examined the inner capillary surfaces using atomic force microscopy (AFM) and scanning electron microscopy (SEM), and we compared the inner capillary surfaces to glass rubbed with a fine abrasive foam; the capillaries had no discernible grooved structures as arises on rubbed glass. Since SSY is known to exhibit natural planar anchoring on smooth glass surfaces [176], our observations of the capillary surface strongly suggest that degenerate planar boundary conditions are present on the inner surfaces of the cylinders and any anisotropic Rapini-Papoular type anchoring effect would be small (see section 3.5) [28, 140]. We also considered alignment caused by flow during capillary filling. Loading capillaries with the LCLC in either the nematic or the isotropic phase resulted in the same type of director configurations. Further, since the filling flow is nearly perpendicular to the final alignment found at the capillary surface, flow alignment appears unlikely. Finally, we considered the possibility that a layer of molecules adsorbed to the capillary surface sets an easy axis at the capillary surface during or shortly after filling. We exclude this possibility by cycling the filled capillary between nematic and isotropic phase and observing that the director at the capillary surface retains no memory from cycle to cycle. Further

considerations of an anchoring effect can be found in section 3.5 below.

### 3.3.1 Observations of Director Fluctuations to Measure Director Configuration

We measure the director angle,  $\beta(r)$ , directly by observing a flickering speckle pattern and its direction in the LC. The pattern originates from director field temporal fluctuations and accompanying fluctuations in the ordinary and extraordinary refractive indices which cause scattering [173]. These types of fluctuations of the director field have been exploited previously to measure the viscoelastic ratios of liquid crystals [21, 163, 164]. Our work follows Ref. [164], which proposed using videos of LC flickering to discern local orientation of the director field. Flickering shape and direction depend on the local director field configuration and LC viscoelastic anisotropy and polarizer orientations.

The experimentally measured  $\beta(r)$  for one of the five LCLC samples studied is shown in Fig. 3.3c. It is well fit by the calculated expression (Eq. 4). The fitting provides experimental values for ratios of the twist-to-bend and saddle-splay-to-bend elastic constants. The twist-to-bend ratio is in close agreement with prior measurements [20].

Since  $K_{24}/\sqrt{K_3K_2} \sim \tan(\beta_1)$  when  $K_{24} \gg K_2$ , the fit values become increasingly sensitive to experimental uncertainties as  $\beta_1 \rightarrow \pi/2$ . The fit value of  $K_{24}/K_3$ , for example, is sensitive to the uncertainty of the measured capillary radius,  $R$ . For the data in Fig. 3.3c, the capillary was measured to have a diameter of 90.6  $\mu\text{m}$  to within  $\approx \pm 0.4 \mu\text{m}$ . This relatively small uncertainty, however, leads to the comparatively large uncertainty we give for our estimate of  $K_{24}/K_3$ , *i.e.*,  $K_{24}/K_3$  has a mean value averaged across experiments of 6.6 with bounding interval [3.8, 9.4]. A discussion of the method for calculating error is in section 3.3.2 below. By contrast,  $K_2/K_3$  is a relatively stiff parameter in the fit; it has a mean value averaged across experiments of 0.12 and a standard deviation  $\sigma_{K_2/K_3} = 0.04$ .

To carry out the flickering measurements, the sealed sample capillary was placed on an indium tin oxide (ITO) coated slide. The ITO slide was attached to a proportional-integral-derivative temperature controller used to maintain sample temperature. The sample was

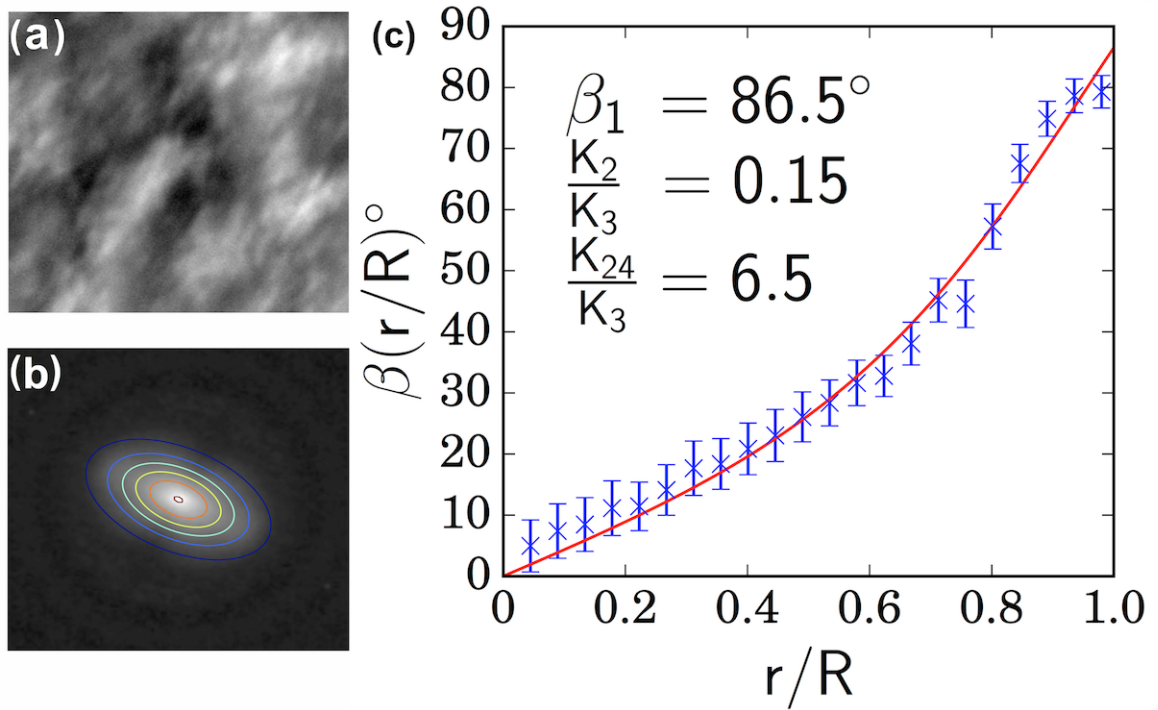


Figure 3.3: (Color online) Representative flickering measurements of 30% wt./wt. SSY in a 90.6  $\mu\text{m}$  capillary at 25°C. **(a)** Single frame from a movie cropped to a 20 $\mu\text{m}$  square and after background subtraction (see main text). **(b)** Averaged FFT of a movie containing many images of fluctuations and contour plot of a 2D Gaussian fit to the averaged FFT. The long axis of the fit is perpendicular to the dominant fluctuation direction and yields a measurement of  $\beta$  for the image slice. **(c)** Fit of Eq. (3.2.4) to  $\beta(r)$  obtained by fluctuation measurements along the capillary radius. Error bars are the standard deviations in degrees of the angle found for the 2D gaussian fits as in **(b)**. A nonlinear least-squares fit of the parameters  $K_2/K_3$  and  $K_{24}/K_3$  gives estimates of the elastic constant ratios (6.5 and 0.15, respectively) for the sample. Across all measurements the average  $K_{24}/K_3 = 6.6$  and has a bounding interval [3.8, 9.4].

then coated with index matching oil before being sandwiched between the slide and the oil-objective. The sample was typically illuminated between crossed-polarizers by quasi-monochromatic light from a 660 nm LED light (ThorLabs LED4D067) that was passed through a 660 nm band pass filter (FWHM = 10 nm) in a Köhler configuration. The condenser diaphragm was narrowed to maximize contrast and parallel illumination.

Images were captured in black and white by a Uniq UP680-CL video camera; the camera gain and shutter speed were adjusted to maximize dynamic range and fluctuation contrast. We use 160x total magnification for narrow depth of focus and high spatial resolving power of director field fluctuations. A piezo-objective-positioner enabled us to precisely move the image plane radially through the capillary; at each position (*i.e.*, for each image plane position) we record movies of the director field fluctuations. The image planes are obtained at one micron intervals. Movies were cropped to a narrow region of 10% of the capillary diameter. At each image plane, we determined the time-average of the video image sequence; then we subtracted the time-average from every frame in order to resolve only the fluctuations. An example of a single frame (with subtraction) is in main text figure 3.3a.

A Hann-windowed fast Fourier transform was computed for the subtracted image associated with every frame. The time-average of these subtracted images was then used to derive the dominant direction of scattering; the latter was accomplished by fitting a two-dimensional Gaussian to the averaged Hann-windowed fast Fourier transform (see figure 3.3b). The dominant direction so-determined is perpendicular to the local nematic director in the sample plane [173]. Repeated measurements at different depths in the capillary gives us  $\beta(r)$

### 3.3.2 Calculation of $K_{24}$ and its Error Bar

The flickering experiment was performed five times (see table 3.1) in five different capillaries with diameters ranging from 88  $\mu\text{m}$  to 99  $\mu\text{m}$ . The value of  $K_{24}/K_3$  is a fitting parameter in the nonlinear least squares fit (NLLS) to  $\beta(r/R)$  (see Eq. (4) of main text). In each experiment a sequence of  $\beta_i$  are determined at image slice position,  $r_i$ , in the capillary. Note

also, the  $r_i$  of each experiment are scaled to the measured value of the capillary radius,  $R$ , of the particular experiment. The capillary radii were measured using a 100x magnification with a wider field-of-view so that the whole capillary was captured in each image. The diameter at mid-plane was determined from the image by comparison to a standardized micrometer scale. Uncertainties arose due to the finite pixel size and our limited ability to choose the image plane that corresponded to the capillary diameter (as opposed to a capillary chord). Together these sources of error led to an experimental uncertainty in the capillary radius of  $\pm 400$  nm.

Error propagation due to uncertainties in capillary radius are somewhat unusual for these experiments. For example, if  $R$  of a particular flickering data set is replaced by a slightly larger radius (*e.g.*,  $R + 400$  nm), then the extrapolated angle  $\beta_1$  will increase, and since  $K_{24}$  is proportional to  $\tan(\beta_1)$ , a measurement error due to a slightly larger capillary  $R$  results in a substantial (positive) shift in the best-fit value of  $K_{24}/K_3$  when  $\beta_1$  is nearing  $\pi/2$ . On the other hand, if  $R$  is replaced by a slightly smaller radius (*e.g.*,  $R - 400$  nm), then the measurement error produces a comparatively smaller (negative) shift in the best-fit value of  $K_{24}/K_3$ . The measurement error bars are thus asymmetric about the mean.

The  $K_{24}/K_3$  data for each capillary are presented in Table 3.1. The three columns correspond to  $K_{24}/K_3$  obtained using our best estimate of  $R$  for each experiment (first column), and  $K_{24}/K_3$  obtained using the smallest (second column) and largest (third column)  $R$  due to the limited measurement resolution.

$K_{24}/K_3$	Lower Bound $K_{24}/K_3$	Upper Bound $K_{24}/K_3$
6.48	4.74	10.32
8.07	3.6	28.59
10.5	4.37	24.3
3.75	2.54	7.21
4.03	3.13	5.681

Table 3.1: NLLS fit parameters and uncertainty from five independent flickering measurements. Upper and lower bounds reflect refitting after replacing  $R$  by  $R + 400$  nm and  $R - 400$  nm, respectively.

The average and standard deviation of our data derived using the best estimate of  $R$  is

$\overline{K_{24}/K_3} = 6.6$ ; the standard deviation is  $\sigma_{K_{24}/K_3} = 2.8$  giving a bounding interval [3.8, 9.4]. These are the numbers we report in the main text.

Of course, the distributions may not be symmetric, and there are many other ways to estimate  $K_{24}/K_3$ . Therefore, as a check, we computed  $\overline{K_{24}/K_3}$ , etc., using several different statistical models. A second model used a weight for each experiment set by  $K_{24}/K_3$  divided by the difference between the upper and lower bounds for  $K_{24}/K_3$ ; a third model used a weight for each experiment equal to the difference between the upper and lower bounds for  $K_{24}/K_3$ ; a fourth model computed the means of each the three columns in the table above to define the error interval; a fifth model employed the log-transform of the data in the table. All of these models gave means and error-intervals that were overlapping with the simplest approach. If we average the results from all of these methods to generate a method-averaged mean and error interval, then we obtained  $\overline{K_{24}/K_3} = 5.8$  and a bounding interval of [3.5, 10.0].

The parameter  $K_2/K_3$  is a relatively much stiffer parameter with respect to both the NLLS fit and the capillary size, so across measurements we simply calculate an average value  $\overline{K_2/K_3} = 0.12$  with  $\sigma_{K_2/K_3} = 0.04$ . Thus we find  $K_{24}/K_2 \approx 55.0$ .

### 3.4 Defects in Escaped-Twisted Configuration

We also observed hedgehog defects associated with the ET configuration. In long capillaries, we typically observed ET domains of opposite handedness separated by chiral point defects. These defects were qualitatively proposed in Ref. [151]. We observed annihilation of neighboring defects, indicating that they carry opposite topological charge. The presence of nematic director singularities are apparent in Fig. 3.4a; bright-field microscopy reveals dark spots from scattered light along the center of the capillary. Once found, we image the point defect under crossed-polarizers with the same illumination described above. We compare these experimental textures with those simulated numerically using Jones matrices. The comparison requires a test director configuration, which we calculate using Eqs. 3.2.1 and 3.2.2. For configurations in the presence of defects, however, the director depends on

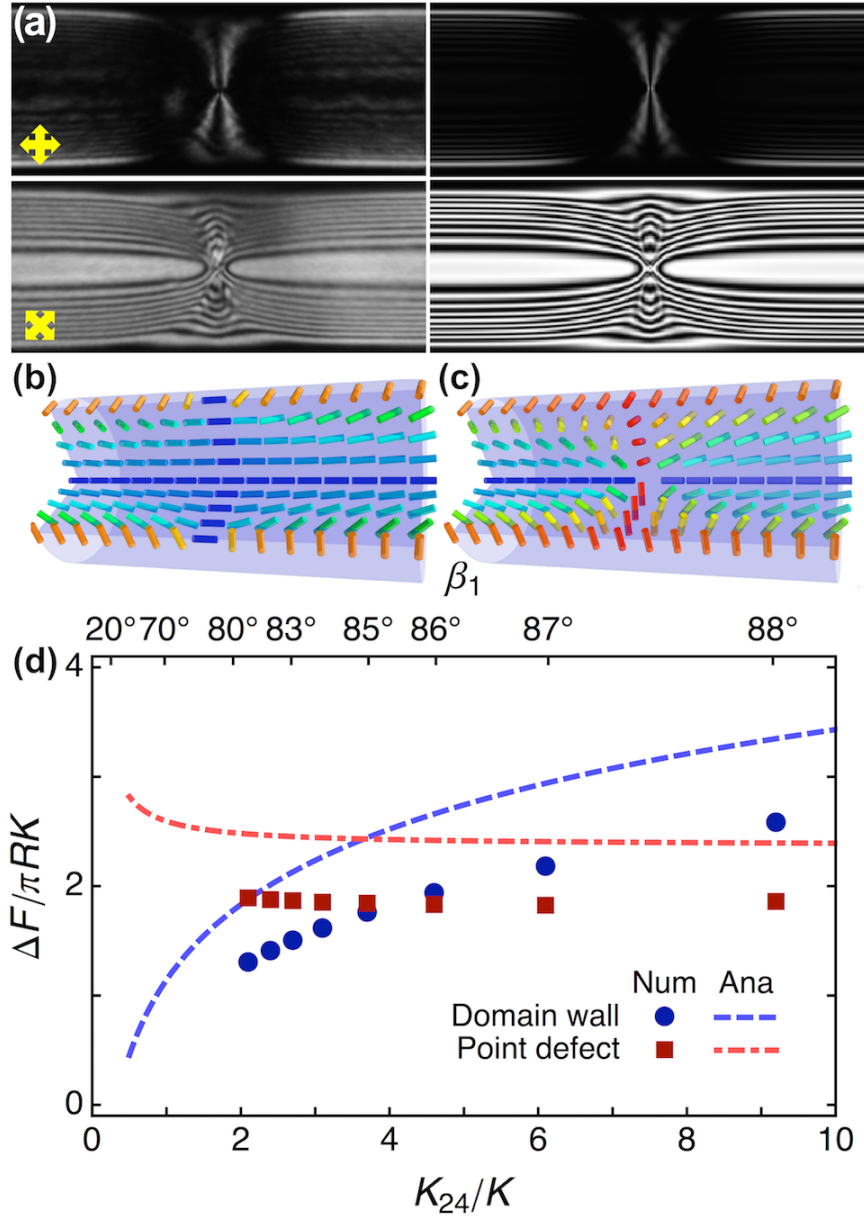


Figure 3.4: (Color online) (a) Left, cross-polarized quasi-monochromatic optical images of singular point defects bordering ET regions of opposite handedness in 90  $\mu\text{m}$  capillary. Yellow arrows indicate the polarizer pass axis directions. Right, images reconstructed using Jones matrix calculations from numerically computed director fields of defects. (b) A 3D cutaway view of a capillary with opposite-handedness ET regions separated by a wall defect. (c) 3D cutaway view of a capillary with opposite-handedness ET regions separated by a point defect as imaged and simulated in (a). In both (b) and (c) the director field represents an LC with  $K_2/K = 0.1$  and  $K_{24}/K = 4.6$ , where  $K_1 = K_3 \equiv K$  and the color scale is the same from Fig. 3.1b. (d) Energies of the point and domain wall defects relative to the ET energy as a function of either  $K_{24}/K$  or equivalently  $\beta_1$ , with  $K_2/K = 0.1$ . Points indicate numerical calculations and lines indicate analytical approximations; the latter have higher energy than the former but demonstrate similar qualitative behaviors.

both  $r$  and  $z$ ; the boundary conditions at  $z \rightarrow \pm\infty$  bring the director configuration back to ET configurations with opposite handedness. To arrive at an optimized guess, we solve the Euler-Lagrange equations numerically with a relaxational technique. The configurations that emerge are very similar to what one gets if one takes the standard radial and hyperbolic hedgehogs and simply rotates all directors by  $\pi/2$  about the  $z$ -axis. This simple operation, which is guaranteed to preserve hedgehog charge, automatically produces opposite chirality on opposite sides along  $z$  of the hedgehog defect regardless of the sign ( $\pm 1$ ) of its charge. The topological charges of successive hedgehogs necessarily alternate in sign. Using  $K_1 = K_3 \equiv K$ ,  $K_2/K = 0.1$  and  $K_{24}/K = 4.6$ , numbers which are consistent with our measurements in the ET ground state, we observed remarkable agreement between experimental and theoretical textures (Fig. 3.4a).

In principle, smooth domain walls can also separate domains of opposite handedness, in which the escaped-twist configuration continuously untwists from one domain to the wall mid-plane and then continuously re-twists with opposite handedness into the other domain (see Fig. 3.4b). In this case, throughout the mid-plane, the director would align along the capillary axis. However, in SSY, we have never experimentally observed such a domain wall structure. Defect energetics provide an explanation for this observation which has an interesting consequence. Again, we numerically calculate the configurations of both domain walls and point defects to obtain their energies. For these calculations, we fix  $K_2/K = 0.1$  in accordance with [20] and our fluctuation experiments, and we allow  $K_{24}$  to vary. As shown in Fig. 3.4d, point defects (domain walls) have lower energy than domain walls (point defects) for  $K_{24}/K \gtrsim 4$  ( $K_{24}/K \lesssim 4$ ). Using  $K_3 = K = 6.5$  pN from [20] and  $R = 50$   $\mu\text{m}$ , a typical dimensionless energy difference of  $\Delta F/\pi RK = 0.1$  corresponds to  $\Delta F = 2.5 \times 10^4 k_B T$ , where  $T = 298$  K is the experimental temperature. If  $K_{24}$  is greater than the crossover value  $\approx 4K$ , then, according to theory, one should not expect to observe smooth domain walls. Thus, both our observations of defects (or lack thereof) and our energy analysis set  $K_{24}/K = 4$  as an approximate lower bound, in agreement with our fluctuation-measured value of  $K_{24}/K = 6.6$  [3.8, 9.4]. This ratio of saddle-splay modulus

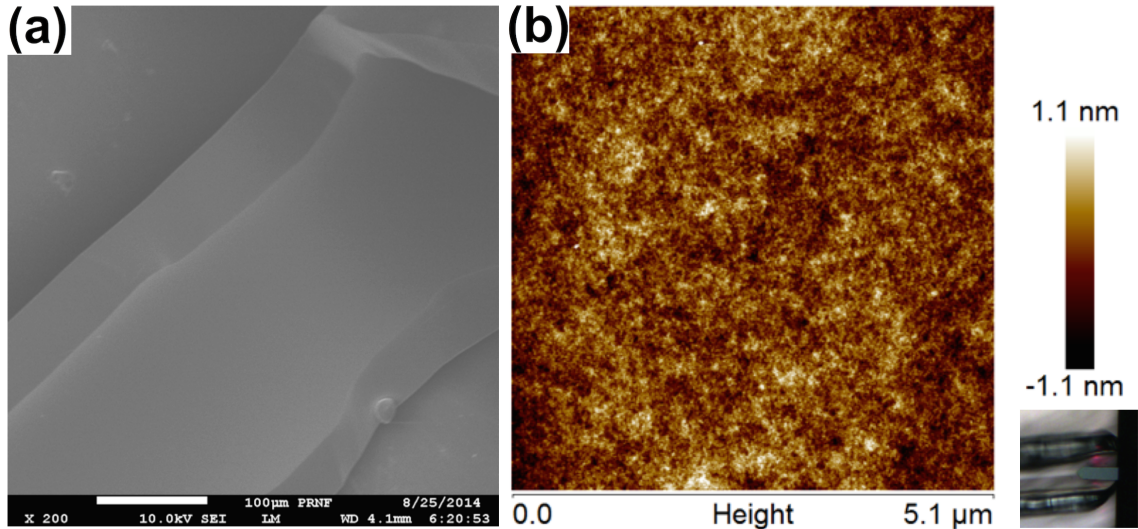


Figure 3.5: (a) SEM of a broken glass capillary with silver sputter coating shows no aligning features. (b) AFM height map of a broken capillary shows a smooth surface to within  $\pm 1.1$  nm with surface roughness 0.3 nm (RMS) after subtraction of overall curvature. Inset is a video still of AFM cantilever inside a capillary.

to the splay or bend modulus far exceeds previous measurements of saddle-splay made in TLCs, and when compared to the twist modulus, this measurement violates the Ericksen inequality relation by more than a factor of 20.

### 3.5 A Possible Chemical Anchoring Effect Mimicking Saddle-Splay

In this subsection, we consider other effects that might induce the same phenomenology that we have observed and assigned to saddle-splay. We first exclude the possibility that some kind of azimuthal interfacial alignment energy (Rapini-Papoular) is mimicking saddle-splay energy and affecting our measurement of  $K_{24}$ . At the capillary surface, a Rapini-Papoular energy has the form

$$F_{\text{RP}} = -W_{\phi}(\mathbf{n} \cdot \mathbf{n}_0)^2 \quad (3.5.1)$$

where  $W_{\phi}$  is an anchoring strength and  $\mathbf{n}_0$  is a preferred director orientation. Our experimental fit  $K_{24}/K \approx 6.1$  and the measurement  $K \approx 7$  pN by [20] give  $K_{24} \approx 50$  pN.

Thus, for an azimuthal alignment effect to interfere with our measurement, it must have  $RW_\phi \gtrsim 50$  pN. We expect a very small  $W_\phi$  because as discussed in the main text, examination of the capillary surface under atomic force microscopy (AFM) and scanning electron microscopy (SEM) reveal no microscopic structures that could favor anisotropic alignment (see Fig. 3.5). Anisotropic surface alignment is commonly achieved by rubbing the surface with an abrasive pad, which produces large grooves along which the surface director prefers to be oriented. We measured the surface profile of rubbed glass prepared as in Ref. [39] and found large grooves in the glass surface. This technique gives  $W_\phi \approx 3 \times 10^{-7} \text{ J m}^{-2}$  for Sunset Yellow (SSY) [39], which for a 100  $\mu\text{m}$ -capillary, would correspond to  $RW_\phi \approx 30$  pN. With no alignment structures visible, we expect our capillary to have  $RW_\phi \ll 30$  pN. Thus,  $RW_\phi$  is insignificant compared to  $K_{24}$ , and anisotropic surface alignment effects can be ignored.

Interestingly, in principle chemical interactions could produce a curvature-dependent anchoring energy,  $F_w = \frac{w}{2} \int d^2S \mathbf{n} \cdot \mathbf{L} \cdot \mathbf{n}$ ; this energy is allowed by symmetry and could arise from chemical interactions between LC molecules or mesogens and the confining surface. Here  $w$  is the anchoring strength,  $\mathbf{L}$  is the surface curvature tensor, and  $d^2S$  is the magnitude of the surface area element. In principle, changes in surface chemistry on the container surface can vary the magnitude and/or sign of  $w$ . If  $|F_w|$  is not small, then its explicit separation from saddle-splay contributions requires experiments using the same LC but in cylinders with different surface chemistry.

We have carried out preliminary measurements to explore this question. In particular Sunset Yellow in a capillary with surface chemistry modified by a silane treatment, Fig. 3.6a, displays a measured total twist angle significantly lower than in a bare glass capillary Fig. 3.6b. Furthermore, in addition to the expected point type defects there appear to be domain wall type defects in this system (Fig. 3.6c and d), which is consistent with a lesser effective value of  $K_{24}$ . Alternatively, or in addition to changing the surface chemistry-curvature coupling, it is possible the silane treatment introduces a preferred tilt angle such that the director is no longer parallel to the capillary surface. The silane surface treatment

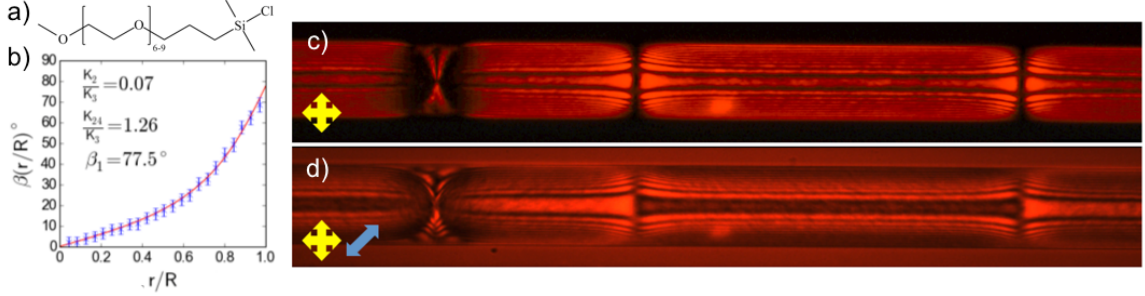


Figure 3.6: Silane treated capillary with planar anchoring has an apparent lesser total twist angle. **(a)** The chlorosilane molecule used to induce (suspected) planar anchoring. It is possible that the silane induces a tilt angle at the capillary interface. **(b)** Measurement of  $\beta(r)$  using the fluctuation methods described in section 3.3.1. **(c) and (d)** POM and waveplate images show alternating chirality domains in a silane treated capillary. The presence of domain walls in addition to point defects indicates a change in the effective saddle-splay modulus.

and its effect on SSY should be tested on flat surfaces to first isolate the possibility of a tilt angle. Further tests of surface treatments are necessary to rule out this and other possible confounding effects.

### 3.6 Conclusion

In summary, we have completed an experimental and theoretical study of a lyotropic chromonic liquid crystal, Sunset Yellow, in its nematic phase and confined in a hollow cylinder with degenerate planar boundary conditions. The escaped-twist configurations found to form in the bulk requires a large saddle-splay modulus, which we have measured for the first time in an LCLC. We also observed point defects in this system whose existence (compared to the absence of smooth domain walls) provides independent confirmation of our measured value of  $K_{24}$ . The measured ratio of  $K_{24}/K_2 \approx 60$  greatly exceeds the Ericksen inequality  $K_{24} < 2K_2$  and implies that nematic LCs can have deformed ground states in confinement. Furthermore, these results indicate that it may be possible to control confined director configurations by manipulating confining surface curvature. In the future, it will be interesting to study and manipulate these chiral configurations and investigate their formation from the isotropic phase.

## Chapter 4

# Deposition and Drying Dynamics of Liquid Crystal Droplets<sup>1</sup>

### 4.1 Introduction

Drying drops exhibit a rich phenomenology that depends on the suspended materials, convection and evaporation [186], surface tension and capillary interactions [187], contact line pinning and depinning [188], membrane stretching and bending [189], Marangoni forces [190, 191], and hydrophobicity [192, 193]. The drying phenomenon thus provides a multi-faceted testing ground for fundamental science and engineering ideas, and insights gained can influence practical applications in printing [194], genotyping [195], and other complex assembly and coating schemes [196, 197]. To date, drying experiments have probed water droplets containing relatively small concentrations of particles [198], polymers [199, 200], surfactants [201, 202], added solvents [203, 204], and salts [205, 206]. These investigations have uncovered fascinating phenomena including coffee-rings [198, 207–210], Marangoni flows [190, 203, 204, 211], electro-wetting effects [212], complex deposition patterns [205, 213], and, in a few cases, formation of concentrated phases very near the drop edge [192, 214–217].

---

<sup>1</sup>This chapter is based on a publication under review.

In this contribution, we explore the evaporation dynamics, morphology, and deposition patterns of drying lyotropic chromonic liquid crystal (LCLC) droplets. These drops differ qualitatively from most others due to their concentration-dependent isotropic, nematic, and columnar liquid crystalline phases in water. As a result, although the LCLC drop starts in its dilute isotropic liquid phase, solute concentration gradients develop and ordered liquid crystal (LC) phases arise in different parts of the drop during evaporation. The concentration profiles, and the formation and separation of liquid crystal phases, in turn, create density, viscosity and surface tension gradients that drive development of novel convective currents, drop morphologies, and deposition patterns. This phenomenology and understanding thus generated provides insight into how to manipulate and control deposition from a new class of drop, *e.g.*, drops containing organic mesogens such as dyes, drugs, and biomolecules with potential to form liquid crystal phases in solution [35, 218].

Our investigation employs a model liquid crystal drop system. It uses the dye Sunset Yellow FCF (SSY) in water whose equilibrium phase behavior and viscoelastic properties are well understood [20]. A combination of polarized optical microscopy (POM), surface profilometry, and optical coherence microscopy (OCM) permit us to dynamically probe drop morphology, heterogeneous formation of LC phases, and evolving convection currents. In contrast to evaporating DNA or carbon nanotube solutions that sometimes form LC structures very near the drop edges [214, 215, 219], the present experiments reveal formation of distinct nematic and columnar LC domains that span large portions of the drop and trigger unique “coffee-ring” phenomenology. The convective flows, the drop morphologies during evaporation, and the final deposition patterns, for example, are heterogeneous and depend strongly on contact angle, SSY concentration and evaporation rate, and the drops are affected by SSY-induced surface tension gradients in counter-intuitive ways.

## 4.2 Materials and Methods

SSY-based LCLCs are composed of organic, charged, plank-like molecules that organize in water into column-like mesogenic stacks. The internal structure of these rods depends on a

combination of non-covalent electrostatic, excluded volume, hydrophobic, and  $\pi$ - $\pi$  stacking interactions [220, 221]. The mesogen assemblies, in turn, organize into nematic or columnar LC phases, depending on temperature and concentration. Under ambient equilibrium conditions, the isotropic - nematic transition occurs at about 30% by weight and the nematic - columnar transition occurs at about 40% by weight [38]. Thus SSY concentration affects two levels of organization: mesogen assembly and LC formation. SSY was purchased from Sigma-Aldrich with 90% purity and was further purified using a precipitation method [38]. SSY solutions of various weight concentrations were prepared with deionized water ( $\rho \geq 18$  M $\Omega$ cm).

The SSY droplets were pipetted from vials containing the various initial solution concentrations and were deposited onto clean glass slides or coverslips. Initial contact angles of the drops were observed to vary depending on the SSY concentration and the substrate surface. Generally drops with comparatively high initial concentration of SSY tended to have larger contact angles than the lower concentration solutions. Evidently, SSY molecules and associated mesogens adsorbed to the air-water interface cause the *surface tension to increase* with respect to its bare value, with the largest SSY concentrations causing the largest surface tension increments. Additionally, drops at 20% SSY by weight had larger contact angles on coverslips ( $\sim 51^\circ$ ) than on glass slides ( $\sim 20^\circ$ ).

Typical droplet volumes were 0.2-0.5  $\mu$ L. Droplet evaporation was observed in both ambient and slow-drying conditions. The latter conditions were achieved by placing droplets in semi-permeable cross-linked polydimethylsiloxane (PDMS) chambers bonded to the substrate and sealed with a cover slip. Evaporation times correspondingly varied, *i.e.*, from minutes in ambient conditions to hours in the PDMS chambers. Videos of the evaporation process were captured by transmission optical microscopy with and without crossed polarizers. The use of POM readily permitted assignment of LC phase (*e.g.*, isotropic, nematic, columnar) and provided structural information (director configuration). Finally, the predominant orientation of the columns was readily determined by measuring polarized light absorption near the absorption peak of isotropic SSY,  $\lambda = 470$  nm ( $\pm 15$  nm FWHM). SSY

assemblies exhibit linear dichroism, and since their absorption is greatest for light polarized perpendicular to the liquid crystal director [38], absorption anisotropy can be utilized to assign director orientation.

Droplet drying was also visualized with a custom ultrahigh resolution spectral domain optical coherence microscopy system (UHR-OCM) [222]. OCM employs low coherence interferometry to measure reflected back-scattered signals from different depths within thick samples (droplets) [223]. For flow visualization, the SSY droplets were doped with a very dilute suspension of micron sized non-functionalized polystyrene particles; time-lapse cross-sectional OCM images were acquired over the full course of the drop drying period. Rapid scanning enabled visualization of the internal fluid flow and phase segregation in cross-sectional image planes with an axial resolution of 1.5  $\mu\text{m}$  and transverse resolution of 3.5  $\mu\text{m}$ . Image post-processing (retrieving, cropping, segmentation) was performed with customized software.

The shapes of dried deposits were studied. Droplets were left on slides to dry overnight and were examined using a Zygo New-View 7300 3D Optical Surface profilometer. The surface profilometry combines low coherence white light with a Michelson interferometer in a light microscope operating in reflection-mode to generate a surface height profile with sub-nanometer resolution. Some portions of the dried droplet surface were located at incidence angles too high for illumination light to be reflected back into the objective. The surface height map of these portions were derived by linear interpolation. Azimuthal angle averages were computed to derive mean height maps of the dried deposits. Lastly, high spatial resolution scanning electron microscopy (SEM) was used to study the deposits after sputter coating with a thin Au/Pd layer.

### 4.3 Results and Discussion

Starting from the earliest stages of the evaporation process, the drying behavior of isotropic-phase LC droplets differs from that of drying colloidal droplets (*e.g.*, coffee drops [208, 224]). Indeed, although the fluid-glass-air contact line of the LCLC-droplet was pinned and the

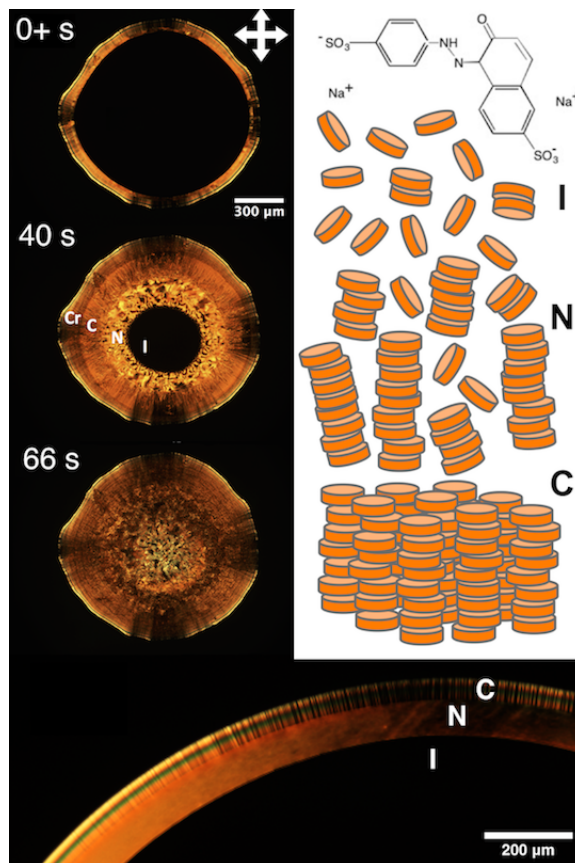


Figure 4.1: Left column, a drying droplet of Sunset Yellow FCF (SSY) on a coverslip under ambient room conditions and with initial concentration of 15% by weight; the drop is imaged with polarized optical microscopy (POM). Recording starts just after the nematic and columnar phases begin to propagate toward the drop center (within approximately 30 s of when the drop is placed on the coverslip). In the frame taken 40 s later, the four stages (including two LC phases) of the drying process are simultaneously revealed from outer edge to the drop center: crystal (Cr), columnar (C), nematic (N) and isotropic (I). Right column: molecular form of SSY salt and schematics of the I, N, and C liquid crystal phases. The highest magnification view (bottom) shows visual textures common to the I, N, and C phases viewed with POM. The darker regions in the drop approximately matching the alignment of the crossed polarizers (crossed double arrows) indicate the director of the LC phases is either parallel or perpendicular to the contact line. We later show the phases are aligned parallel to the contact line.

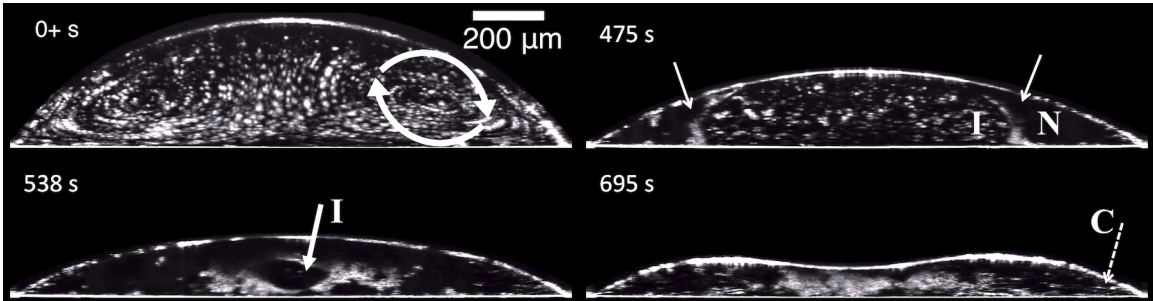


Figure 4.2: The drying progression imaged by UHR-OCM. The drop is placed inside a humidity trapping enclosure that slows its drying rate. White spots in the image are micron-diameter polystyrene particles that strongly reflect light and act as tracers of convective fluid flows and LC phase boundaries. Image capture begins within 30 s of placing the drop. In the initial drying stage, convective flows move toward the pinned contact line along the drop-air interface and move inward to the drop center along the substrate (see arrows in the frame taken at 0+ s). At later times (475 s), a phase boundary, identified by the arrows, shows that particles in the isotropic phase (I) are prevented from entering the viscous and comparatively dense nematic (N) region that is nucleating from the droplet edge; the particle concentration tends to be large at these phase boundaries. Eventually, particles are swept toward the droplet center where they form a shell around a remaining isotropic fluid bubble (arrow, 538 s), and as the region of isotropic phase shrinks to zero volume, the particles irreversibly cluster. The columnar phase first appears in the OCM images as white lines near the droplet edge (538 s). These bright lines are not caused by particles; rather, they are cuts through boundaries between domains of varying columnar orientation and thus strongly scatter light. The white lines at the edges of the drop in the last frame (695 s, dashed arrow) show the boundaries of columnar phase (C) regions.

drop had a spherical cap shape, even at the earliest time scales probed ( $\lesssim 0.3$  seconds after placing the drop on the slide), the pure radial convective flows toward the drop edge, found in the usual coffee-ring effect, are not observed [208, 224]). Rather, different and unusual convective flows are found and are described in detail below.

In the earliest drying stage, SSY concentrations throughout the drop remain below that of the isotropic-nematic phase transition, but very soon thereafter SSY mesogens are transported to the drop edge where their concentration builds up. Initially, the SSY suspension has neither translational nor orientational order, and the drop is not birefringent (it appears black when viewed through crossed polarizers). The primary geometrical characteristics that vary during this initial period are the drop height relative to the glass substrate and, to a lesser degree, the contact angle at the drop edge. The drying process begins to deviate from the common coffee-ring drop drying behavior as the SSY concentration increases near the droplet edge. Since the evaporative flux is greatest near the drop edge, convection currents in the drop carry SSY mesogens towards the contact line where the SSY concentration increases and the nematic and columnar phases initially form. As evaporation proceeds, a nematic-isotropic phase front, and later a columnar-nematic phase front, propagate radially inward.

During the whole process, texture differences arise between phases within the droplet and are visible in both bright-field and POM. These imaging modalities enable us to distinguish the birefringent nematic and columnar phases from the isotropic phase that remains near the drop center. Under ambient laboratory conditions (20 °C and 40% relative humidity), four stages of the drying process, corresponding to formation of the four complex fluid phases, can be clearly distinguished using POM as shown in Figure 4.1. Ultimately, almost<sup>2</sup> all water evaporates leaving a polycrystalline “coffee-ring” deposit of SSY.

Before emergence of the anisotropic liquid crystal phases, the drop drying phenomena differs qualitatively from most droplet evaporation studies to date. The first notable difference is the presence of convective flows along the drop-air surface toward the outer contact

---

<sup>2</sup>SSY is slightly hygroscopic.

line where the droplet remains pinned. During evaporation of a *pure water* droplet, an outward convective flow inside the drop arises because the contact line between the drop edge and the substrate remains pinned at the position of greatest evaporative flux. To compensate for the lost water near the edge, a radially outward flow is established [208]. However, in the liquid crystal droplet, the increased SSY concentration near the drop edge leads to a local *increase* in the surface tension on the drop surface, and therefore a surface tension gradient arises. The surface tension is larger at the drop edge than near the drop center. The surface tension gradient, in turn, creates a substantial Marangoni flow along the interface towards the air-droplet-glass contact line, accompanied by an inward flow towards the drop center along the droplet-glass interface. The resulting flow pattern produced by the SSY concentration-induced surface tension gradient is thus *opposite* to Marangoni flows observed in typical water-surfactant drop drying [190, 225].

Differences in flow patterns are easily visualized with UHR-OCM by adding 1  $\mu\text{m}$  polystyrene particles to the suspension. The patterns are shown in Fig. 4.2. Pure circular convective flows are seen from the earliest observed times (at  $< 0.3$  seconds) and persist until the emergence of a nematic phase. The difference in flow circulation direction compared to previous observations with surfactants arises because higher concentrations of SSY at the interface cause the surface tension to *increase* rather than decrease from its bare value. This behavior is also observed among many salts [226]. The microscopic causes of these effects in LCLC drops may be related to the unusual amphiphilic structure of SSY, which leads to assemblies of molecules that do not align like conventional surfactant amphiphiles at an interface [227].

After formation of the nematic phase, the isotropic-nematic phase boundary systematically moves toward the drop center from the drop edge. Effectively, the isotropic-nematic interface is repeatedly pinned and depinned in the process. The alternating dark and light regions of the LC phase in Fig. 4.1, and the light absorption due to linear dichroism (Fig. 4.4), indicate that the average director orientation is parallel to the glass-isotropic-nematic contact line. At higher magnification, we find that the inward moving phase boundary is a

biphasic region wherein nematic tactoids nucleate in the isotropic region and coalesce into the nematic region as in Fig. 4.3. Because the drying process is out-of-equilibrium and the system is 3D, the nucleation and coalescence behavior in the drop is different from the merging of tactoids observed during cooling of confined 2D (equilibrium) systems [228]. Here, topological defects are observed to rapidly annihilate in the continuous nematic region as the phase boundary advances.

A columnar phase nucleates along the edge of the SSY nematic-substrate contact line before the system completely dries. The texture of the columnar phase depends on the concentration and drying rate of the droplet. When drops are dried in ambient conditions, neighboring regions of columnar phase with slightly different alignment form domain walls (see Fig. 4.5a and Fig. 4.5b). On-average though, the column orientation is determined to be tangent to the contact line using the linear dichroism effect as in Fig. 4.5c and 4.5d. Boundary walls separate domains with different orientations that form during the drying process, thereby producing features visually similar to walls observed in other hexagonal columnar lyotropic and discotic systems [214, 229]. We first considered that the out-of-equilibrium rapid drying of the system and high viscosity of the columnar phase combine to create kinetically trapped columnar domains that are unable to rearrange to form regions of bend. These walls are apparent in crossed polarized images as in Fig. 4.5e and close up in Fig. 4.5f. To further clarify the origin of the columnar domains, we dried the drops extremely slowly in humidity chambers (Fig. 4.6). In this case, similar domain walls appear within the initially smooth regions of columnar phase. Based on these data and X-ray investigations, which have shown that correlations between molecules and assemblies increase with increasing concentration of the columnar phase [220, 230], we suspect that the inter-columnar correlations between molecules create domains of true three-dimensional crystals and thus domain walls are energetically preferred compared to bend deformations.

The final morphology (coffee-ring pattern) of the drop deposit can be complex and depends strongly on the initial concentration of SSY. Similar experiments with droplets confined to cylindrical wells also found a dependence on the initial concentration of solute

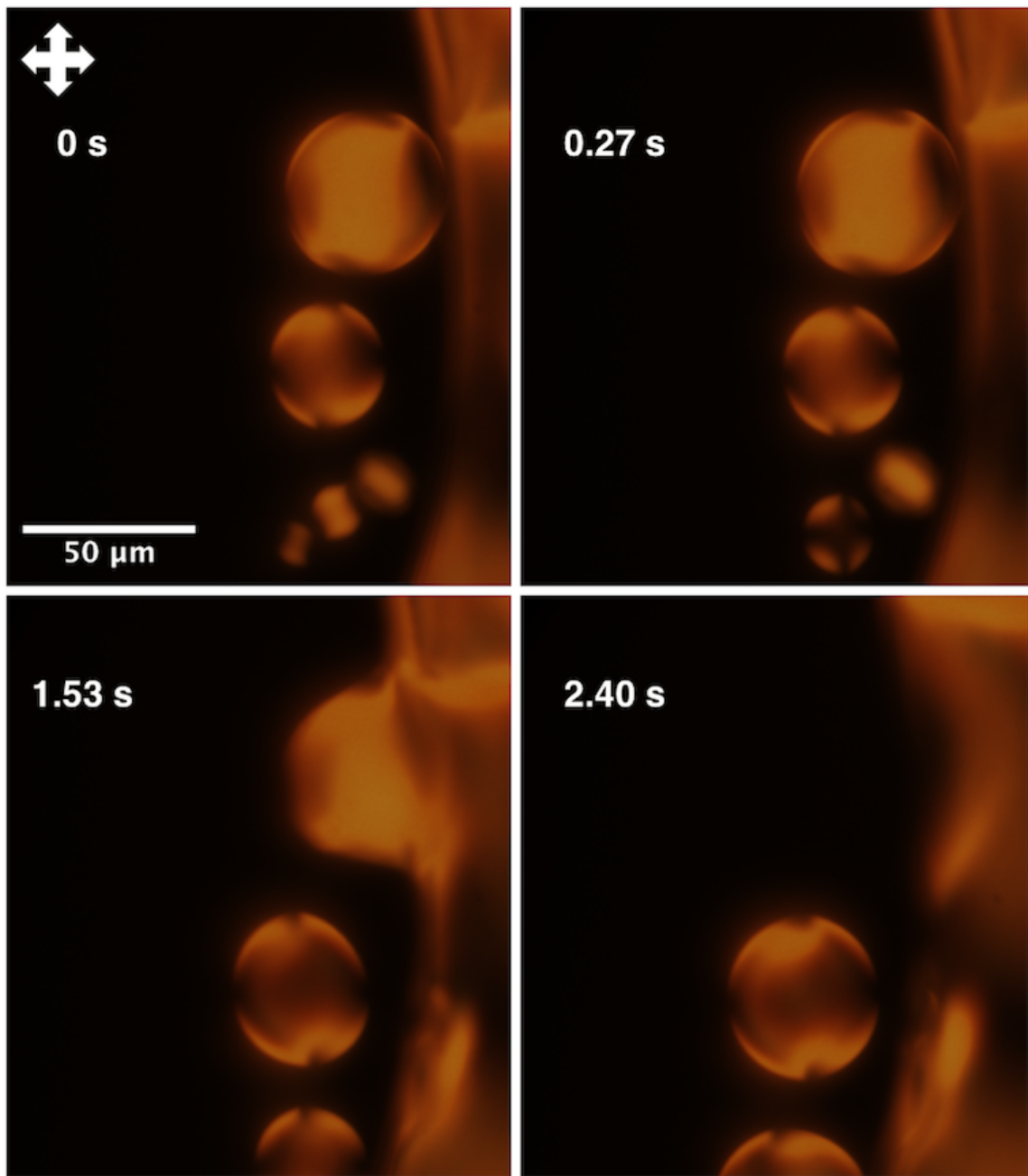


Figure 4.3: At the moving isotropic-nematic phase boundary, nematic tactoids nucleate in the biphasic bulk fluid region near the interface. The tactoids then either coalesce with other tactoids nearby or into the advancing phase boundary. The droplet is viewed by POM and is evaporating under ambient conditions, with an initial concentration of 15% SSY by weight. Between 0 s and 0.27 s, two small nematic tactoids in the lower middle portion of the frame are observed to coalesce into a single larger tactoid. Approximately one second later, at 1.53 s, a larger tactoid is seen to coalesce with the phase boundary. The defects that transfer into the bulk annihilate rapidly, *i.e.*, before 2.40 s.

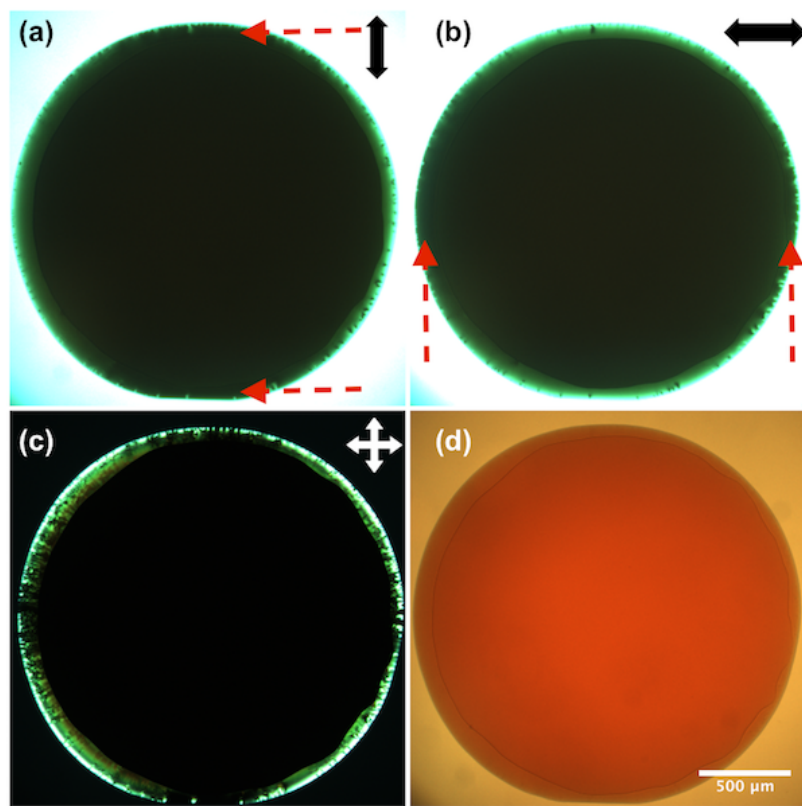


Figure 4.4: A drying drop of SSY on a glass slide initially with 15 % concentration by weight forms a ring of nematic phase near the contact line with director alignment tangential to the contact line. In the top row, the drop is illuminated with polarized light from a halogen bulb light source and a light filter designed to filter out light with wavelengths greater than 500 nm. Linear dichroism of the nematic phase causes greater absorption of polarized light with orientation indicated by the double black arrows. In (a), the top and bottom regions of the drop indicated by the dashed red arrows are darker than the sides, and in (b), the left and right sides of the drop indicated by dashed red arrows are darker than the top and bottom due to alignment of the nematic director. Crossed polarizers (c) and bright field (d) show similar features to those in Fig. 4.3. The columnar and crystalline phases have not yet formed near the drop edges in these images.

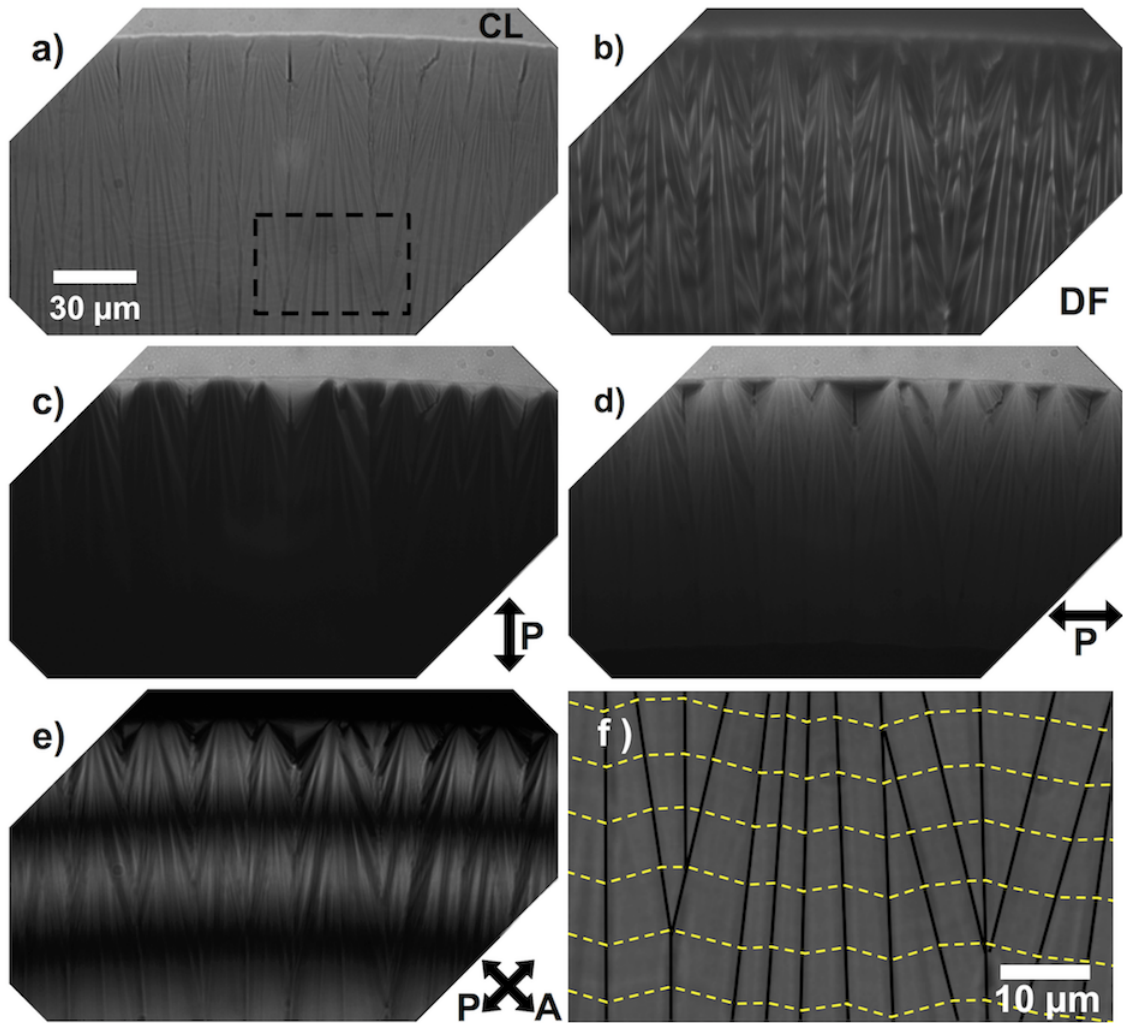


Figure 4.5: An enclosed drying LCLC droplet with initial concentration of 15% SSY by weight on a glass slide is in the columnar phase near the drop edge: (a) Bright field shows dark lines separating columnar domains and the contact line (CL); (b) Bright lines in dark field (DF) transmission are regions where light is scattered by sharp changes in the index of refraction caused by disorder; (c) & (d) Polarized (P) light transmission with  $\lambda = 470 \text{ nm}$  ( $\pm 15 \text{ nm}$  FWHM) is absorbed more when molecular stacking is perpendicular to the light polarization direction. Thus, the data shows columnar alignment is on average tangent to the contact line. (e) Crossed-polarized transmission increases contrast between regions with varying columnar alignment. The large black bands are regions where the polarization of the exiting light is extinguished by the analyzer (A) due to the birefringence and varying thickness of the sample. (f) Schematic of the observed circumferential alignment of the LC from the boxed region in (a). Dashed yellow lines represent SSY director orientation and thick lines are domain walls of alignment discontinuity. See text for details.

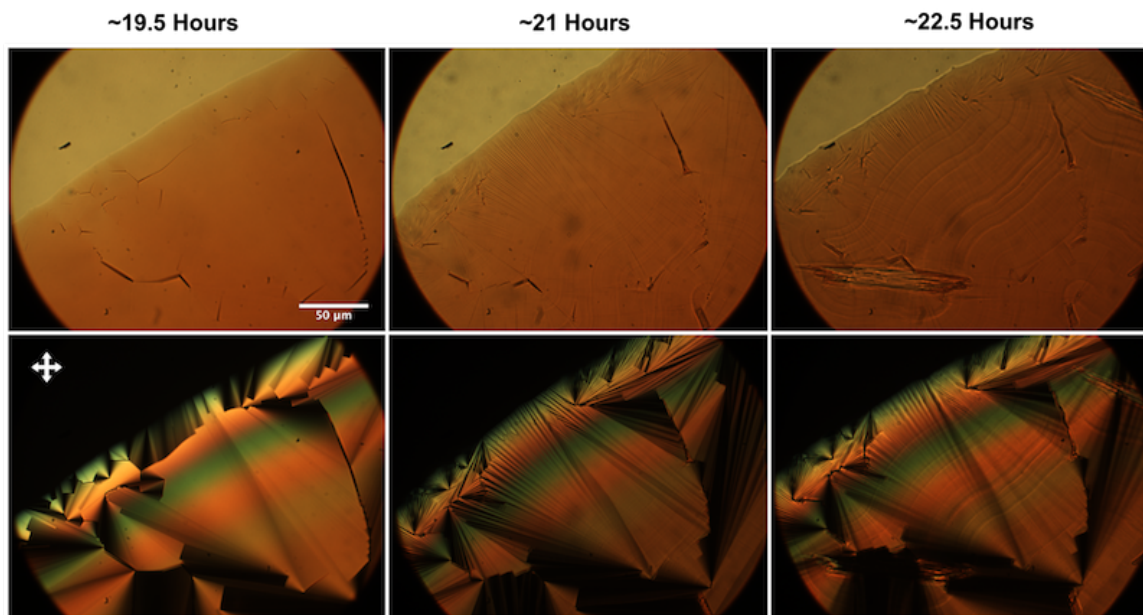


Figure 4.6: Slowly dried drops of SSY on a glass slide show coarsening of the columnar phase as the concentration increases. The top row shows a time series of bright field images and the bottom row shows the corresponding crossed polarized images. Drops were observed once every 1.5 hours. The first observation of the columnar phase was made after  $\sim 19.5$  hours of drying in the humidity chamber. The subsequent observation at  $\sim 21$  hours showed a texture similar to main text Fig. 4.5, but unlike the main text figure, the texture emerges after the columnar phase is present and not at the nematic-columnar phase boundary. In the last observation at  $\sim 22.5$  hours, crystal phase chunks begin to emerge.

[231]. Here we measure the surface height profile of the SSY deposit after evaporation with a Zygo surface profilometer, Fig. 4.7. At low initial concentrations ( $\leq 10$  wt%), a largely traditional coffee-ring-like effect dominates, depositing the SSY near the drop edge as the contact line recedes. This pattern has only a light covering of SSY molecules near the center of the droplet and a broad rim of SSY molecules near the drop edge. At higher initial SSY concentration ( $\geq 10$  wt%), however, more SSY is retained in the droplet’s central isotropic region, *i.e.*, as nematic and columnar phases; along with a surrounding elevated rim, this deposit is akin to a “volcano” or a sunken soufflé [231]. This effect occurs when propagation of the nematic phase front is rapid. Throughout the isotropic phase, flows are present, but at higher concentrations, only a small fraction of the SSY has a chance to be deposited near the edges by the flows during drying. This is because the flow into outer regions is blocked by the comparatively large viscosity of the nematic/columnar LC phases and the moving phase boundaries.

Mesogen orientation within the dried deposits was observed with scanning electron microscopy. When drops are allowed to dry quickly in ambient conditions, as in Fig. 4.7, the central region of the droplet is found to contain small domains, which appear to be turbulent flows frozen in place. Nematic domains arise with various orientations, then merge, and then freeze into the columnar phase. The continued drying and increasing viscosity makes it impossible for the LC to relax to a smooth uniform state during the time before the evaporation finishes. In contrast, the surface of the thicker rim region appears smooth, displaying no signs of trapped local flow. This smoothing is plausible because the SSY near the rim has enough time to anneal to a more homogeneous microstructure. Generally, drops that dried very slowly, *i.e.*, drops in humidity controlled chambers, exhibit greater uniformity of molecular orientations over larger regions compared to deposits from drops that dried quickly.

In summary, the drying of Sunset Yellow FCF containing droplets exhibits peculiarities unique to lyotropic chromonic liquid crystals. Oriented fluid phases form and move within large regions of the drop throughout the drying process, and SSY concentration gradients

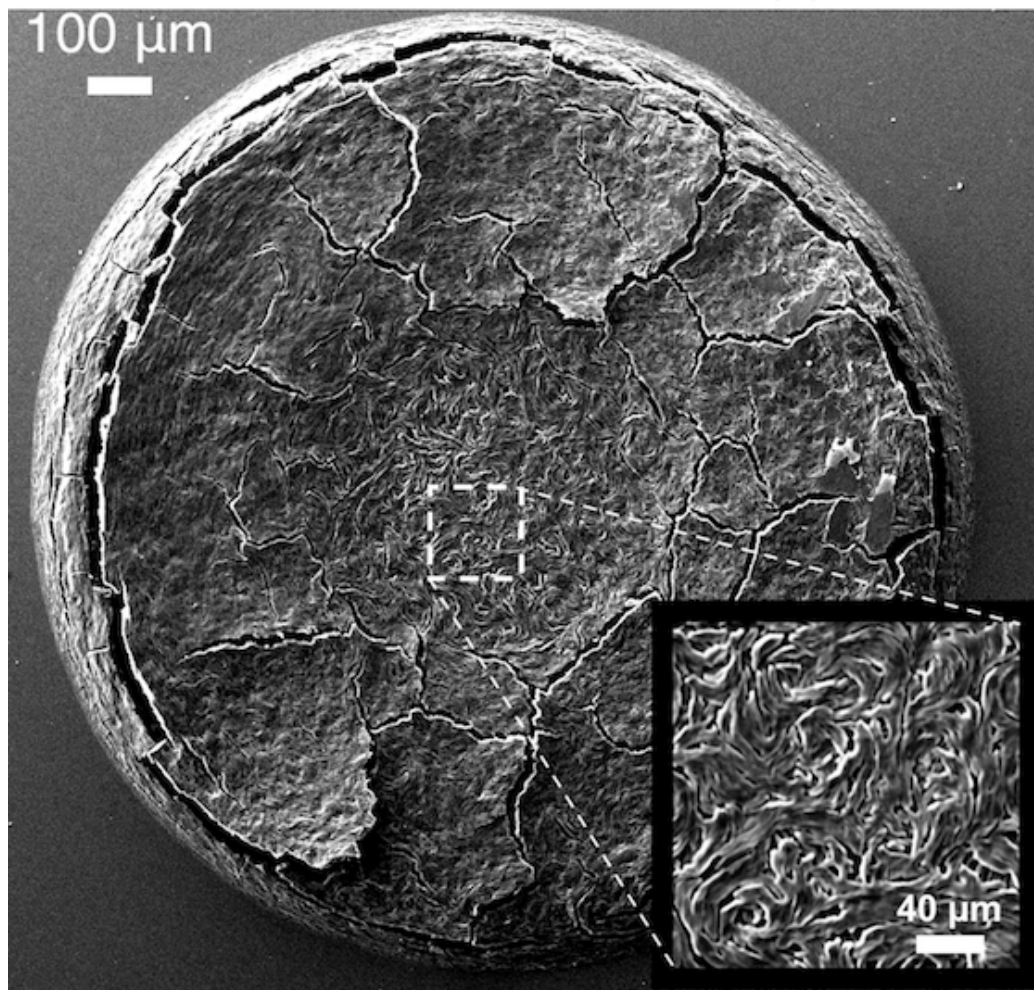
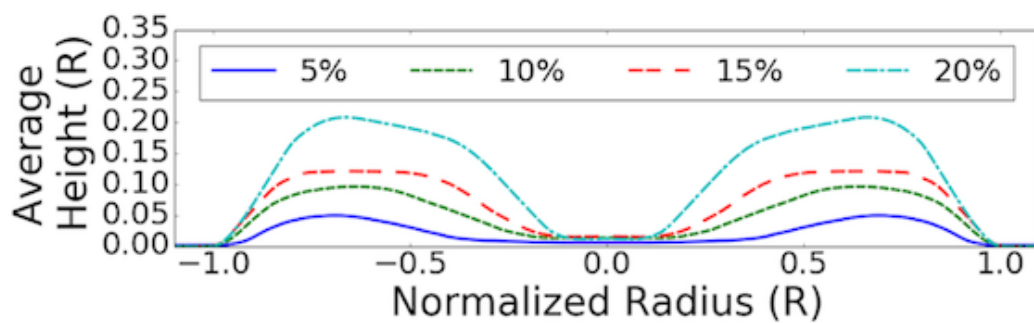


Figure 4.7: Top, Profilometry results of dried droplets with varying initial weight concentrations of SSY. Drop size, or more precisely position within the drop, is normalized by the drop radius due to differences in spreading; all drops had a radius of approximately 0.5 mm. Bottom, a scanning electron microscope image of a droplet of SSY on a coverslip dried in ambient conditions. The droplet had an initial concentration of 15% SSY by weight. The inner region (inset) of the droplet thins due to the convective flows during drying and locks in the turbulent flows present in the drop just before the transition to the more viscous LC phase.

lead to Marangoni flows in the isotropic phase. These SSY-induced convective flows circulate opposite to those induced by conventional surfactants. Finally, the initial concentration and drying rate of the SSY solutions affect their final deposition and even the orientation of assemblies in the dried deposit, and are thus revealed to be essential parameters for creating uniform (or non-uniform) material deposits. Since many molecules with LCLC phases are common among dyes and pharmaceuticals, control of their deposition from solution are informed by our findings. Furthermore, these observations combined with methods of substrate patterning offer a means to control formation of polarizing and light absorbing films based on LCLCs.

## Chapter 5

# A Machine Learning Investigation of Structure and Dynamics of Soft Colloidal Glasses

### 5.1 Introduction

The manner by which crystalline solids respond and deform when strained is well studied and is understood to be closely related to structural defects present in the crystalline lattice [232, 233]. Similarly, properties such as heat capacity, thermal conductivity, and electrical conductivity are also dependent, at least in part, on the distribution and types of defects in the crystalline lattice [233–236]. Notably, point-like structural defects in crystalline lattices, such as vacancies or impurities, are readily identified, and line-like or plane-like structural defects in crystalline lattices, such as dislocations, are readily characterized by geometric parameters (*e.g.*, Burgers vector) [233, 236].

By contrast, in glassy (amorphous) solids and super-cooled liquids, no comparable “simple” methods exist for identifying structural defects. As a result, we have much less understanding about how to predict and control bulk properties of the disordered solids such as their shear response, heat capacity, or conductivity [41, 42, 44]. Of course, this deficiency

presents exciting challenges for the community which have stimulated efforts to identify “defect” candidates in amorphous materials. Indeed, localized rearrangements have been observed in glasses [46, 47, 49, 50, 237], and they are somewhat similar to those that occur within “premelting matter” near defects in crystalline solids . Thus, development of rigorous methods for identifying soft/fragile regions in amorphous solids via structural signatures would represent an appreciable materials advance; such advances would, in turn, offer routes towards understanding the response and failure mechanisms of glassy matter. The preliminary research described in the present chapter takes steps towards these goals.

To date, mean field theory and other system aggregate approaches that ignore local structural heterogeneity have had limited success connecting mechanical response to structural properties [43, 238–240]. By contrast, dynamical and indirect measures of structure have demonstrated some recent success in finding so-called soft spots with a propensity to rearrange [47, 49, 50, 55, 237, 241]. In particular, localized low frequency modes have been shown to be correlated with structural rearrangements during shearing, thermal perturbation, and long duration relaxation [51, 242–247]. Likewise, indirect structural measures with a dynamic component have proven useful for predicting dynamical heterogeneities and local rearrangements [52, 56, 248]. Very recently, a method based on machine learning has successfully demonstrated a direct connection between structure and cage breaking rearrangements (or hops) in simulated atomic systems and in granular material experiment [57, 58, 249, 250].

In the present work, we build on these very recent developments by Schoenholz, et al. [58] and utilize machine learning to predict rearrangement-prone soft spots in colloidal glasses, *i.e.*, to predict where rearrangements will occur. In general, particles in supercooled liquids and in glasses experience dynamic arrest because they are surrounded by neighbors, which form a “cage” [251–253]. Particles move within cages randomly over short time scales,  $t_R$ , called “residence times”. At longer time scales, particles can overcome the local activation barriers with energy,  $E_b$ . These barriers confine the particles to their cages; particles which cross over their local barriers are said to rearrange. In our work, we investigate the

residence times between cage rearrangements, and the activation energy associated with each rearrangement, using a Kramers activation model. The approach takes advantage of the softness concept developed in Ref. [58]. Ultimately, we utilize a support vector machine (SVM) to connect activation energies associated with each particle by considering their local cage structure.

Before reading further, the reader should be warned that the research reported in this chapter is comparatively preliminary compared to the research on liquid crystals in the other chapters of this thesis. The latter form the core of my thesis. Nevertheless, important progress has been made on the rearrangement problem that we felt was sufficient to report herein. We anticipate that completion of this work will occur within the next few months.

## 5.2 Materials and Methods

We employ a 2D binary suspension of soft poly(N-isopropyl acrylamide) (PNIPAM) microgel particles as an amorphous model system to study the structural origin of particle rearrangements [59, 254]. We synthesized both particle species by semi-batch/one-pot method as described in Ref. [59]. Particles are prepared in a deionized water solution at a desired volume fraction and sandwiched into a quasi-2D packing by placing a small amount (0.6  $\mu\text{L}$ ) of solution between two  $18 \times 18 \text{ mm}^2$  glass cover slips, which were first cleaned by an ethanol rinse. The sample is then sealed with Norland 65 optical glue and cured for 30 minutes to prevent evaporation. The two species of colloidal particles, with diameter  $\sigma_1 = 1.4 \text{ }\mu\text{m}$  and  $\sigma_2 = 1.1 \text{ }\mu\text{m}$ , are tracked by video microscopy at 10 frames per second for 90,000 frames using standard methods [255, 256]. The inset of Fig. 5.2a shows a typical cropped image frame of data used for tracking of the particles.

### 5.2.1 Classifying Stable and Rearranging Particles

Each  $i$ -th particle has a trajectory,  $r_i(t)$ , which we use to compute various functions that describe the system dynamics and characterize local caging structures. For example, we can compute the mean-square displacement [257],  $\text{MSD}(\Delta t)$ , and self-overlap function [258–

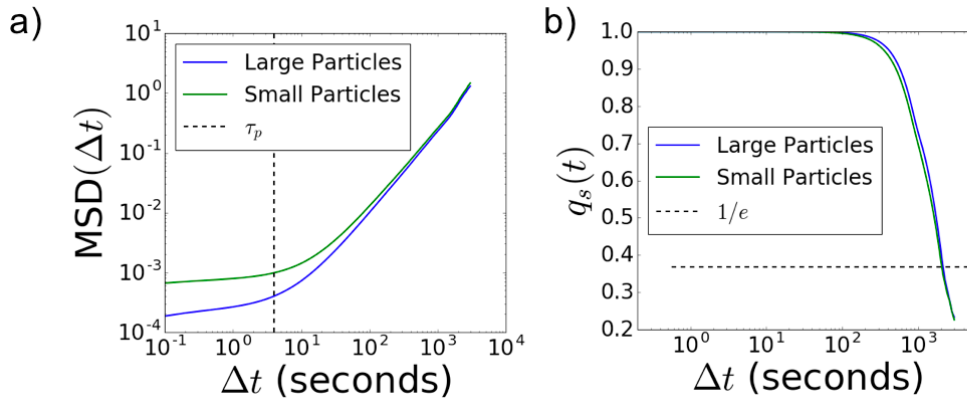


Figure 5.1: Mean square displacement (MSD) and self-overlap function,  $q_s(t)$ , of both large and small particle species. **(a)** We compute the MSD from particle trajectories for each species (large and small) of particles. Small particles are more active at shorter times but longer time scale displacements are similar. The time parameter,  $\tau_p$ , used in the  $P_{\text{Hop}}$  function is chosen from the  $\beta$  relaxation point, *i.e.* when on average particles exhibit cage breaking motion. **(b)** The self-overlap function,  $q_s(t)$ , describes what fraction of particles have been displaced at least a large particle radius ( $0.5\sigma_1$ ). The most stable particles in our sample are those confined such that they are not displaced  $0.5\sigma_1$  for at least  $\sim 2000$  seconds.

260],  $q_s(t)$ , to derive system ensemble characteristics used to set parameters in the machine learning algorithm as in Fig. 5.1. The MSD is the average displacement-squared traveled by a particle in the sample during the time  $\Delta t$ . In Fig. 5.1a, we show MSDs for both large and small particles for a segment of our sample over a time scale that includes particle cage motion and cage breaking. The crossover time between cage motion and cage breaking,  $\tau_p$ , is used later in this work. The self-overlap function is a measure of the fraction of particles that have moved at least a distance equal to half-a-particle-diameter from their initial position. We utilize  $q_s(t)$  to define the minimum amount of time that a particle must “not rearrange” in order to be considered stable. Note, we have scaled all of the particle displacements such that their coordinates are in units of the large particle diameter  $\sigma_1$ .

To characterize particle rearrangements, we utilize the so-called hopping function,  $P_{\text{Hop}}$  [52, 248, 261]. This function enables us to define rearrangement events and to determine the  $i$ -th particle’s residence times (time between rearrangement events). The  $P_{\text{Hop}}$  function also has the advantage of being a single particle method that does not depend on the definition of a local cage, as is often done for other methods that characterize rearrangements such as

$D_{\min}^2$  [45].

$P_{\text{Hop}}$  is defined as

$$P_{\text{Hop}}(t) = \sqrt{\langle (\vec{r}_i(t) - \langle \vec{r} \rangle_B)^2 \rangle_A \langle (\vec{r}_i(t) - \langle \vec{r} \rangle_A)^2 \rangle_B} \quad (5.2.1)$$

where  $A$  and  $B$  are time intervals  $[t - \tau_p, t]$  and  $[t, t + \tau_p]$ , respectively, and the brackets,  $\langle \rangle_A$  and  $\langle \rangle_B$ , indicate time averages over those intervals. The interval window size,  $\tau_p$ , is chosen to be a length of time roughly corresponding to the caging time,  $\beta$ -relaxation, which is found by measuring the sample’s mean square displacement (see Fig. 5.1a). In our experiments we compute  $P_{\text{Hop}}$  for all particles in the sample at all observations times. *Note, though the function is computed for each species independently, for clarity, in the remainder of this chapter we only report on it for the large particles.* The results we find below hold for smaller particles as well but the machine learning procedure is less accurate for them. We believe this is due to data limitations; there are not enough big jumps/rearrangements of small particles or enough very stable particles to carry out the machine learning procedure accurately as described in section 5.2.2 below.

To distinguish particles undergoing rearrangement events from particles that are stable we invoke three parameters: two threshold values on  $P_{\text{Hop}}$  and a so-called minimum stable time  $t_c$ . Two classes of particles (rearranging and stable) define the particle-states selected for the training set used in the SVM algorithm. Specifically, a “high” threshold value,  $P_H$ , is selected so that the 1000 particles with the largest peak values of  $P_{\text{Hop}}$  are labelled as rearranging. The minimum stable time,  $t_c$ , is found by computing the self-overlap function,  $q_s(t) = (1/N) \sum_{i=1}^N H(|r_i(t) - r_i(0)| - 0.5\sigma_1)$  [258–260], for all particles and finding the time when  $q_s(t) = 1/e$  as in Fig 5.1b. Then, a “low” threshold value,  $P_L$ , is chosen such that 1000 particles do not have a  $P_{\text{Hop}}$  value greater than  $P_L$  for at least a time  $t_c$ .

## 5.2.2 Machine Learning Details

The goal of the machine learning approach is to distinguish, based purely on structure, those particles that are likely to rearrange from those that will be stable for a long time. To this

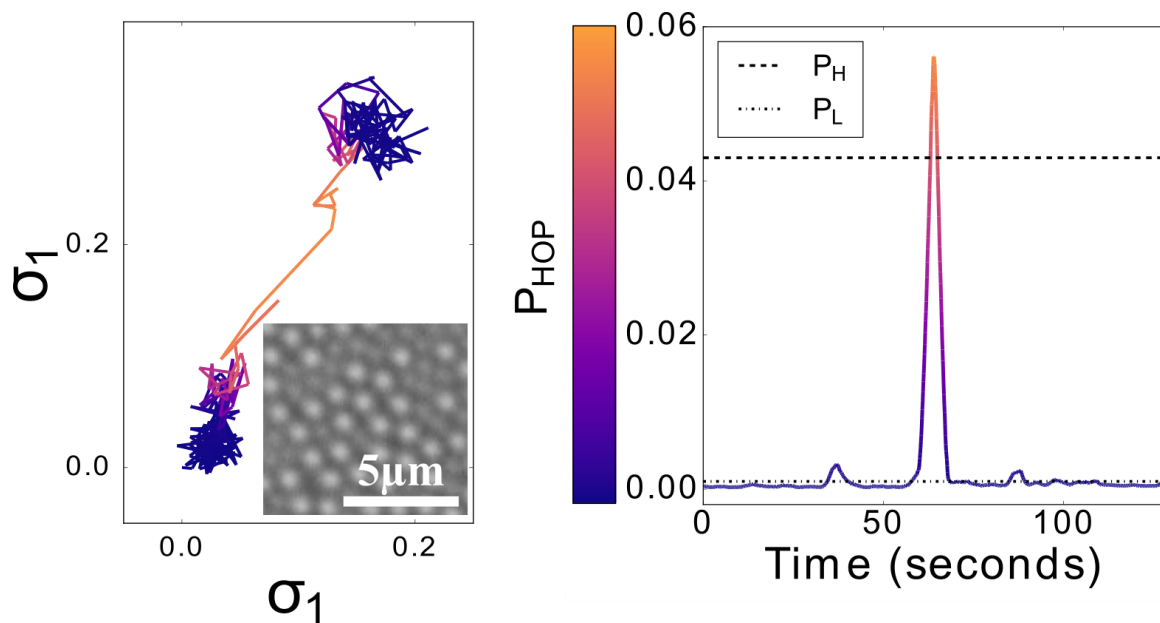


Figure 5.2: Poly(N-isopropyl acrylamide) (PNIPAM) particle trajectory and its corresponding  $P_{\text{Hop}}$  values. (a) A typical trajectory of a particle in the  $xy$ -plane that undergoes a large rearrangement. The  $x$ - and  $y$ -axes (horizontal and vertical, respectively) are scaled to the large particle diameter,  $\sigma_1$ . The inset shows a cropped image of the PNIPAM particles. Large particles appear brighter. (b) The  $P_{\text{Hop}}$  trajectory of the same particle from (a). Because this particle's peak value of  $P_{\text{Hop}}$  is greater than  $P_H$ , this particle is included in the training set class of "rearranging" particles for the machine learning algorithm.

end we employ an SVM [262, 263]. Briefly, we desire structural features that can represent the local caging structure around particles but which are also capable of distinguishing the classes of rearranging and stable particles.

As a hypothetical example, consider two features,  $F_1$  and  $F_2$ , which are computed for every particle. If we compute these features for particles known *a priori* to be rearranging or to be stable, and if we label them as such in the 2-dimensional feature space, then the goal of our algorithm is to show that the labeled groups of particles are well separated as in Fig. 5.3. These two labeled groups are collectively called the SVM’s “training set”. In other words, we seek the line (in the 2-dimensional hyperspace) that best separates rearranging from stable particles in the training set. The fraction of particles in the training set that are correctly divided by the hyperplane is the SVM’s accuracy.

In practice, having selected the particles that make up the training set, we train two SVMs, one for each particle species using generic local 2-point structural features that represent the cages surrounding each ( $i$ -th) particle [264]. The functions we choose are radial correlation functions:

$$G_Y^X(i; \mu) = \sum_{j \neq i} e^{-(R_{ij} - \mu)^2 / l}, \quad (5.2.2)$$

where  $j$  runs over all the particles within  $5\sigma_1$  radius,  $X$  and  $Y$  indicate the species of the  $i$ -th and  $j$ -th particle respectively,  $l = 0.1\sigma_1$ , and  $\mu$  takes all values between 0.3 and 5.0 in increments of 0.1. Thus there are for each neighboring species 47 features that describe the local cage environment of each particle for a total of 94 “structure features”. Note, the features we chose only characterize the radial distribution of the cage forming neighboring particles. We also tested features that characterize bond angle between neighbors, but we did not find them to improve the accuracy of the SVM hyperplane. For the rearranging class of particles, the features are computed at a time-delay ( $\tau_p$ ) prior to when the particle’s  $P_{\text{Hop}}$  value increases above  $P_L$ . For stable particles, the features are computed in the first frame for which the particle’s  $P_{\text{Hop}}$  is less than  $P_L$ . To account for boundaries (edges) in

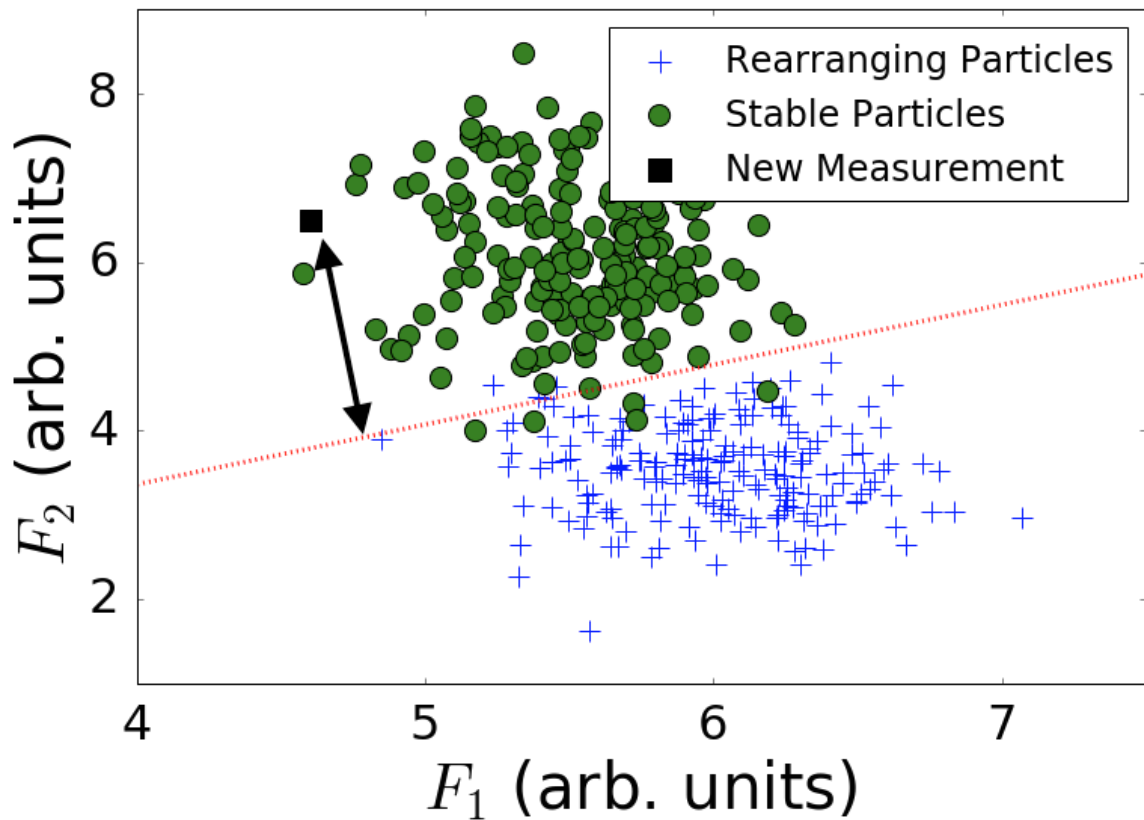


Figure 5.3: Description of support vector machine (SVM) method. Particles are first classified as “rearranging” (blue crosses) or “stable” (green dots) by *e.g.*  $P_{\text{Hop}}$  (see text). Then features that represent their local caging are computed. In this case, the two hypothetical features,  $F_1$  and  $F_2$  are found to well separate the classes of rearranging and stable particles (though not perfectly). The SVM accuracy is the fraction of particles correctly sorted by the hyperplane. The SVM algorithm generates a hyperplane (red dotted line) that best separates the two classes of particles. A measurement of a new particle’s (black square) features  $F_1$  and  $F_2$  then can be used to predict if that particle will rearrange or be stable. We define the particles “softness” as its signed distance (displacement) from the hyperplane (doubled headed arrow).

the sample, we only utilize particles that are at least  $5\sigma_1$  away from the edge of the field of view in the training set and in the results computed below. The SVM training accuracy for large particles and small particles is 85% and 80% respectively.

The trained SVM hyperplane is then employed to characterize the entirety of the observed data (the “test” sample). This process yields softness values of the whole system [58], *i.e.*, for every particle at every instant in time. Briefly, the result of the SVM training is a 93 dimensional hyperplane that best separates the cage structures of rearranging particles from the cage structures of the most stable particles. The cage structures of all other particles in our experiments (the “test” samples) are then computed at all times using the structure features of equation 5.2.2. Finally, the signed distance (displacement) from the hyperplane is then computed for each particle at each time point. This signed distance (displacement) is called the “softness”; positive values of softness indicate a particle is more likely to rearrange, and more negative values indicate a particle is more stable.

Once an SVM is trained on a sufficiently large dataset, the softness parameter can be determined from a purely structural measurement such as an image of the particle ensemble. Given a single image frame, the same hyperplane can be used to compute softness of particles in other colloidal glasses with similar packing conditions and interactions. The goal then is to employ softness, a structural measure of particle packings, to predict dynamics of the particles and ultimately to characterize the properties of the bulk colloidal glass. In the following section, we show that softness is predictive of the residence times that particles will spend in their cages, and thus is predictive of the local activation energy barriers they must overcome to rearrange.

### 5.3 Results

Our preliminary experimental results in the colloidal glasses demonstrate that the softness value of a particle is predictive of that particle’s likelihood to undergo a rearrangement. Specifically, from the  $P_{\text{Hop}}$  trajectories of each particle, we determine the residence times,  $t_R$ , during which the particles’  $P_{\text{Hop}}$  value does not rise above the threshold  $P_L$  (Fig. 5.4a).

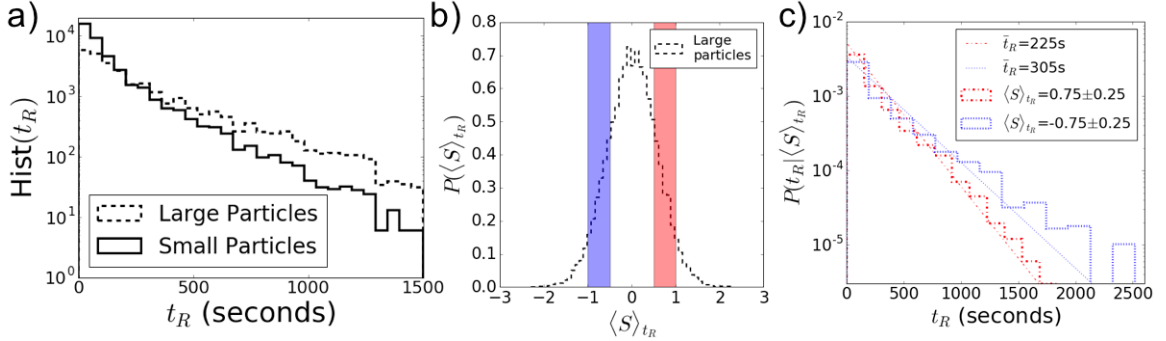


Figure 5.4: Distributions of residence times, softness, and residence times conditioned on softness. **(a)** The total distribution of residence times,  $t_R$ , for both large and small particles. **(b)** The distribution of time averaged softness values,  $\langle S \rangle_{t_R}$ , for all large particles during their residence times. The shaded blue and red regions in **(b)** are used to select residence-times/softness from the total distribution in **(a)**. **(c)** For large particles, the mean residence times of conditioned distributions,  $\bar{t}_R$ , shows a decreasing mean with increasing mean softness,  $\langle S \rangle_{t_R}$ , during residence times.

Put another way, the residence times,  $t_R$ , represent the duration of time between a particle's rearrangements. The average softness,  $\langle S_i(t) \rangle_{t_R}$ , is also computed for each particle during these residence time periods between rearrangement events. Notice that this distribution of average softness over all events is approximately gaussian and is centered near zero (Fig. 5.4b).

We next bin the particles more finely by softness value, and we consider the behaviors of particles within each bin. This strategy for analysis generates two interesting experimental observations. First, the particle residence times within each narrow bin of softness appear to be exponentially distributed. Second, the mean residence time of all particles within each narrow softness bin decreases monotonically as softness increases, as in Fig. 5.4c. To our knowledge, these observations represent new experimental results for thermal colloidal glasses. They also corroborate expectations that the softness parameter is connected to physics of colloidal glasses.

While we do not know of an underlying mechanism to suggest a precise form for the relationship between softness and residence time, we suspect the apparent exponential distributions of residence times within a softness bin may be due to Kramers like activation processes [265]. In particular, each particle cage structure creates an activation energy

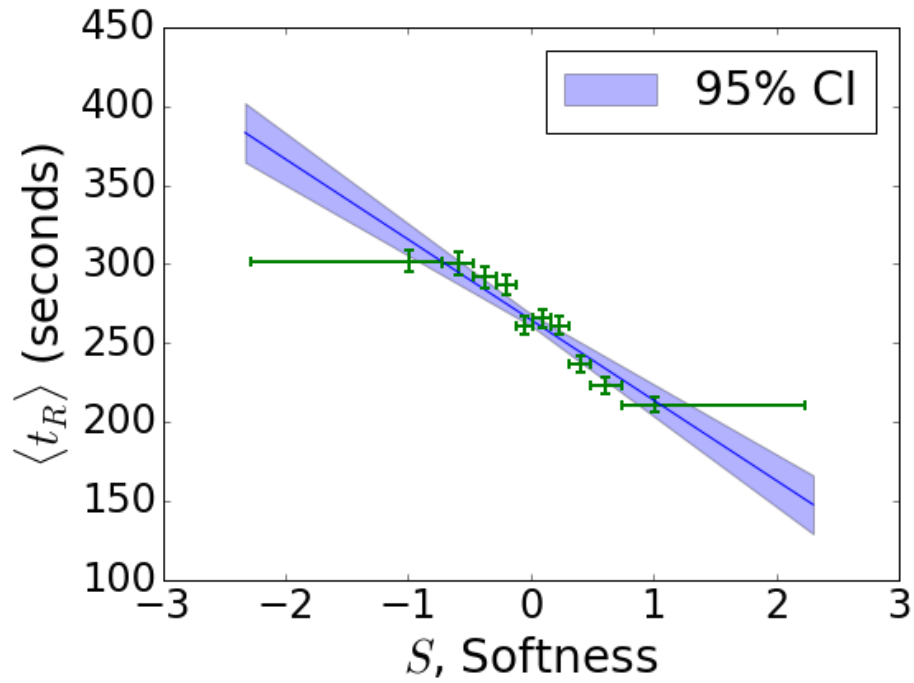


Figure 5.5: Average particle residence times versus average softness of corresponding particle during residence time. The trend line fit is a ordinary least squares linear regression of  $t_{R,i}$  against  $\langle S_i(t) \rangle_{t_{R,i}}$ . The green markers are the result of equal count binning of particles by softness and the averages of the corresponding averages of the logged residence times. The softness error bars indicate the bin range of softness values. The  $\langle t_R \rangle$  error bars are the standard error of the mean residence time, *i.e.*, the standard deviation of residences times within the bin divided by the square root of the number of particles in the bin,  $\sigma_{t_R}/\sqrt{N}$ .

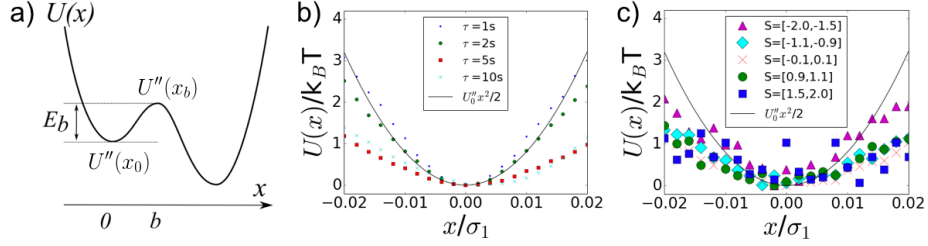


Figure 5.6: Explanation of Kramers reaction rate theory and measurement of average caging potential due to neighboring particles. **(a)** Shows a cartooned energy landscape in one dimension that a particle at  $x = 0$  might experience. The (activation) energy barrier,  $E_b$ , is the energy such a particle would need to overcome to break its cage and complete a rearrangement. The local shape of the energy potential near both average position,  $x = 0$ , and the barrier peak,  $x = b$ , are described by the second derivatives of the potential  $U''(x_0)$  and  $U''(x_b)$  respectively. **(b)** We assume that the confining potential due to caging near a particle's average position is approximately quadratic. Larger displacements at short time scales,  $\tau$ , from an average central position require larger energies. At short enough time scales the fluctuations about a cage do appear quadratic. Larger values of  $\tau$  will include some non-quadratic cage breaking motion. From displacements during  $\tau = 2\text{s}$  averaged over all particles during their residence times we invert the Boltzmann distribution to find  $U''(x = 0) \approx 1.6 \times 10^4 k_B T / \sigma_1^2 = 5 \times 10^{-5} \text{ N/m}$ . **(c)** The local confining potential shape does not appear to vary by particle softness thus we use an average confining potential shape,  $U_0''$  for all particles.

barrier for rearrangement. Furthermore, each cage structure also corresponds to a softness value. We can test this idea by performing an ordinary least squares linear regression of the residence times  $t_{R,i}$  against  $\langle S_i(t) \rangle_{t_{R,i}}$  [266]. The low P-value  $< 0.001$  indicates the effect is real and the model is at least qualitatively meaningful. That is, an increase in particle softness is an indicator that particle's residence time will be shorter, as shown in Fig. 5.5. We note that regressions testing other relationships, *e.g.*, exponential, quadratic, would likewise have similar statistical significance and that a fundamental theoretical description is desirable to further interpret this result.

We next utilize the above relationship and we apply Kramers reaction rate theory to the problem. Briefly, Kramers reaction rate theory describes the relationship between energy barriers and a reaction (activation) rate for how often reactions (activations) will cross that barrier in the presence of thermal Brownian fluctuations. Since our colloidal glass is a thermal system, this approach is reasonable; it would not be justified in a granular system. For our system, we assume the activation rate of cage breaking (the inverse of a residence time) is determined by the energy barrier imposed by each particle's cage structure and the

size of Brownian motion within the cage. In particular, we use the simple barrier-crossing model to calculate the distributions of activation energies,  $E_b$ , in our sample [265, 267], but in place of a reaction rate, we use a measured residence time (or corresponding rate):

$$\frac{\langle t_R \rangle}{t_0} \simeq \nu e^{E_b/k_B T}, \quad (5.3.1)$$

$$\nu = \frac{2\pi k_B T}{(U_0'' U_b'')^{1/2} \lambda^2}. \quad (5.3.2)$$

Here, we measure time in units of the diffusion time,  $t_0 = \lambda^2/D_0$ , where  $D_0 \approx 0.16 \mu\text{m}^2\text{s}^{-1}$  is the short time diffusion constant for the particle. Notice that the hop length,  $\lambda$ , will cancel in the next steps.

To compute the activation energies we must also find the shape (curvature/second-derivative) of the local confining potential,  $U''(x_0)$ , and obtain the same shape information for the cage barrier,  $U''(x_b)$ . We can experimentally derive the local confining potential by assuming a quadratic shape and Boltzmann distribution for the particle deviations from their average position at short times during their residence periods. Figure 5.6 shows energies of particle displacements according to their Boltzmann distributed positions. To fit the shape of the local potential well, we use displacements up to  $\tau = 2\text{s}$ , which is sufficiently less than the  $\tau_p$ , the  $\beta$  relaxation time, but enough to sample the potential well shape. We also checked for a correlation between the local confining potential shape and softness but found no clear correlation, *i.e.* the well shape does not appear to change significantly for different softness values (see Fig. 5.6c). This observation suggests that the particle softness will depend more on activation barrier energy than the local shape of the potential well. Because we cannot measure the barrier shape, we make a common assumption that  $U''(x_b) = -U''(x_0)$ . Note, if we did not make this assumption, the value of  $U''(x_b)$  would enter our result in a log-square root. Thus, from equation 5.3.1, we obtain

$$\frac{E_b}{k_B T} \simeq \ln \left[ \frac{\langle t_R \rangle U''(x_0) D_0}{2\pi k_B T} \right], \quad (5.3.3)$$

which allows us to re-plot Fig. 5.5 with an energy scale in Fig. 5.7.

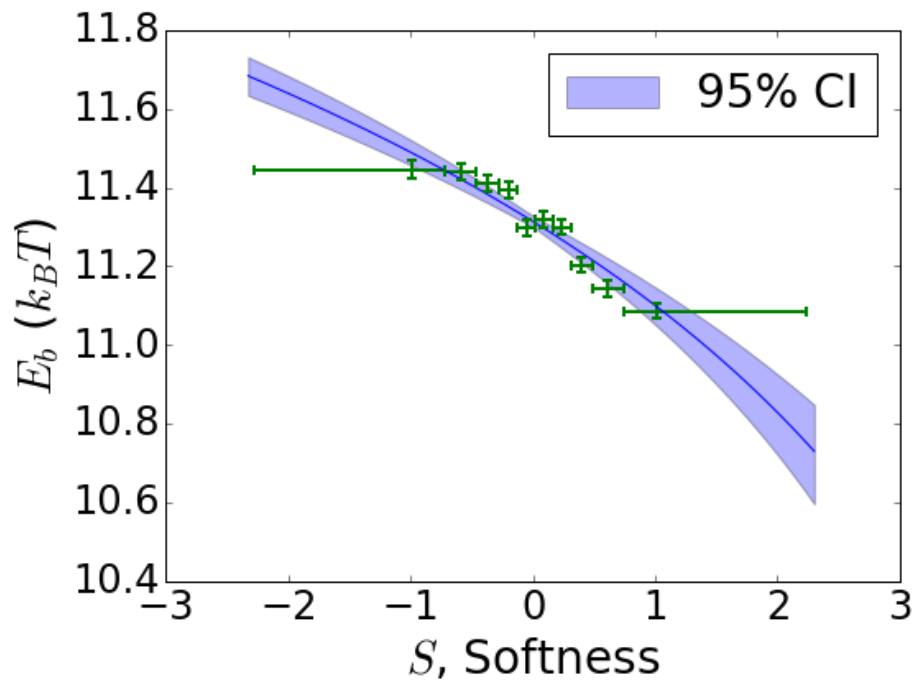


Figure 5.7: Local activation energy versus softness. From measurements of particle residence times and potential well shape (see text) we apply Kramers reaction rate theory to derive activation energies as a function of particle softness. The green markers are the result of equal count binning of particles by softness and the average activation energy of the particles in those bins. The softness error bars indicate the bin range of softness values. The  $E_b$  error bars are the standard error of the mean energy due to variation in residence times within a given softness bin, *i.e.*, the standard deviation of energies within the bin divided by the square root of the number of particles in the bin,  $\sigma_{E_b}/\sqrt{N}$ .

Though residence times (activation rates) are measured accurately, the energy barrier calculation relies on the assumptions made in applying Kramers reaction rate theory. Interestingly, we have now connected a static measure of particle cage structure to activation energy barriers throughout a glassy colloidal system. The distribution of activation energies is inferred from measurements of residence times of particles in their cages via application of Kramers activation theory; this approach enables us to deduce the corresponding energy barrier. Evidently, the combined effects of a distribution of activation energies and a Kramers process is responsible for the heterogeneous activation rates that gives rise to a broad distribution of total residence times in our colloidal glass. We next attempt to interpret which physical characteristics of the cage structure are important for setting the softness and thus the local energy barrier.

### 5.3.1 Interpreting Cage Structure-Softness Relationship

The machine learning algorithm obscures the underlying physical features that describe the local cage structure by reducing the 94 features we use to a single softness value. Ideally we would have an intuitive way to understand cage structure defects like vacancies or geometric measures used to describe defects in crystalline lattices. Therefore, to create a structural interpretation of softness, we examine the average structure feature values of the 3000 softest and 3000 “hardest” particles from Fig. 5.4b. In Fig. 5.8 we plot the average values equation 5.2.2 over all  $\mu$  used in computing the features of large particle.

Apparently, for the softest particles in our sample, the absence of particles, especially large particles, in the first shell of caging particles begins to hint at the structural underpinnings of something like flow defects in crystalline lattices. However, the first shell does not appear to be the only determinant of softness. Other differences between the softest and hardest particles seem important, *e.g.*, the number of smaller particles at distances greater than a particle diameter also seems important in determining softness. Had the presence of particles within one large particle diameter been sufficient to determine particle softness, then local cage volume should have been enough in previous studies to determine energy

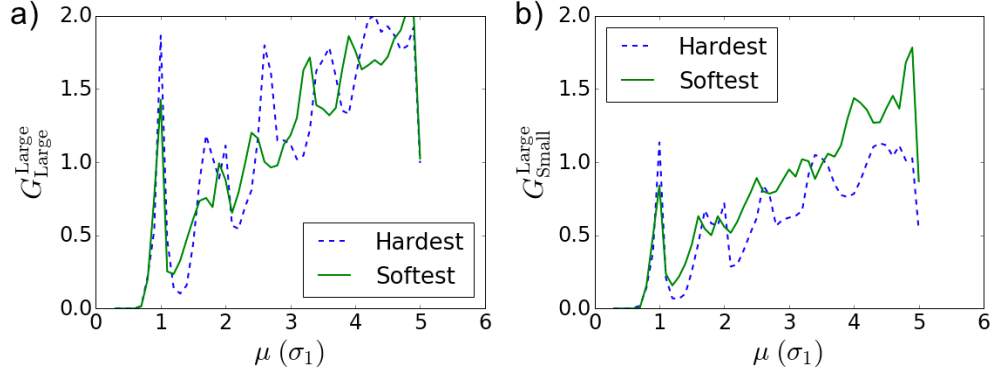


Figure 5.8: Structure features for extreme values of softness. The softest 3000 particles have an average softness of approximately 1.0. The least soft, or “hardest”, 3000 particles have an average softness of approximately -0.87. **(a)** Shows the average values of the 47 structure features between large and small particles. **(b)** Shows the average values of the 47 structure features between large and large particles. The peaks and valleys of the function roughly correspond to the shells at multiples of particle diameter. Higher peaks indicate the presence of more particles of the respective subscript on the  $G_Y^X$  functions at the distance  $\mu$ . Correspondingly, lower valleys indicate fewer particles of the respective subscript at that distance  $\mu$ . Harder particles are likely to have more large particles nearby in their first shell.

barriers like we have done. Adding additional features, such as a measure of bond orientation, might help to further interpret what aspects of local structures determine activation barrier energy.

## 5.4 Discussion

Our preliminary experiments and softness analysis have quantitatively shown that local caging structure of particles is predictive of energy barriers that particles must overcome to rearrange. Of course, the local caging structure also predicts softness, so softness is explicitly correlated with activation barrier too. The energy barrier distribution we have measured is spread over approximately  $1 k_B T$  between  $11.6 k_B T$  and  $10.6 k_B T$ . Interestingly, these experimental numbers are the same order of magnitude found in several simulation works [58, 268, 269]. We have also found that local particle structure can be interpreted using softness and that certain structures, namely the absence of large particles, result if softer particle caging. We expect that careful tuning of local packing structure and thus energy barrier distribution can affect bulk material properties such as shear response

and mechanical failure.

Experiments could test these ideas further, for example by directly shearing a system, such as was done in Ref. [270], then we should be able to use the training with SVM to recognize soft spots particular to that system. Other related advances might connect the softness field and heterogeneity of activation energies directly to the dynamic heterogeneity and the four point correlation function  $\chi_4$ . Finally, testing this method over a range of temperatures (or packing fractions) as in Ref. [58] might prove to be a useful tactic for understanding the glass transition. In particular, at higher temperatures (or lower packing fractions), the predictive value of structural information should degrade and the correlation between softness and residence times ought to diminish, because particles would no longer be caged, *i.e.* they would diffuse freely.

Several theoretical questions remain as well. Our use of the SVM decision function (distance to hyperplane) in a predictive model is a nonstandard method of machine learning. A theoretically derived relation between softness and residence time would also be highly desirable. Nevertheless, the phenomenological result we have presented in this paper demonstrates that there is a connection between structure and dynamics via softness, even though our result does not as yet provide a deep explanation of the connection.

## Chapter 6

# Summary and Future Directions

Liquid crystals and disordered solid materials have proven to be rich systems for soft matter physicists to study. Both systems have yielded theoretical and technological advances through the application of physical principles. My dissertation has furthered both subfields by identifying and examining frontier questions and niches in each. Specifically, in the bulk of this thesis, I have shown that an unusual liquid crystal material, lyotropic chromonic liquid crystals (LCLC), exhibits fascinating chiral structures and assembly due to its large elastic anisotropy and concentration-dependent phase behavior. In a separate set of experiments, I have also shown that a model colloidal glass exhibits structural signatures which are predictive of heterogeneous rearrangements among its constituent particles and, further, that machine learning algorithms can detect those signatures. These results are summarized in more detail below; in addition, new avenues are suggested for further investigation.

### 6.1 Lyotropic Chromonic Liquid Crystals

The experiments I performed explored the effect of confinement on LCLCs. I confined aqueous Sunset Yellow FCF (SSY) solutions to spherical drops in a continuous oil phase, and I confined SSY to cylindrical capillaries. In both cases, the topology imposed by the confining geometry and interfacial boundary conditions produced unusual twisted structures of the nematic phase. Nematic SSY has a strikingly low twist elastic modulus relative to its splay

and bend moduli thus it can preferentially twist to relieve splay and bend deformations. In the case of the SSY droplet, I found that the regions around Boojum defects had concentrated splay and bend energy density. However, a twisted director throughout the drop significantly diminished the total elastic energy by reducing the splay energy – especially near the boojum. A similar effect was at play in cylindrical capillary confinement; however, instead of distortions near defects reducing splay, the homeotropic boundary conditions imposed by the capillary wall produced a twisted- and escaped-radial (TER) configuration. The non-zero  $\alpha(r)$  (see Fig. 2.9) increases twist in the director field, but it also reduces splay such that the total energy is lowered.

Twisting is inherently chiral; thus the twisted configurations, which reduced the system energy, also induced spontaneous mirror symmetry breaking. In droplets, I found that there was no preferred handedness; entire droplets adapted left- and right-handed twisted bipolar configurations with equal frequency. When confined to capillaries with homeotropic anchoring, regions of left- and right-handedness formed with equal probability throughout the capillary and met at defects. Furthermore, when regions of opposite escaping direction met at defects, the handedness across the defect always switched, *i.e.* the defects always joined heterochiral regions. I performed numerical calculations and slow temperature annealing experiments to test for the possibility of homochiral defects, but interestingly, I found such defects to be energetically more costly; the LCLC would add additional domain walls to avoid homochiral defects.

In the second group of experiments, I confined nematic SSY to a cylindrical capillary with planar anchoring. As in the previous experiment where SSY was confined to a capillary with homeotropic anchoring, SSY again spontaneously broke mirror symmetry and adopted an escaped-twisted (ET) director configuration. The ET configuration is distinct from the TER configuration; it involves no splay deformations of the director field. By measuring the twist in the confined ET director field, I found that SSY saddle-splay, the elastic modulus associated with director configurations at the surface, is many times larger relative to the bulk elastic moduli than in typical liquid crystal materials. Saddle-splay,  $K_{24}$ , is in fact

so much larger that I found it violates the Ericksen inequality, which states  $K_{24} < 2K_2$ . This experiment set also introduced a new technique to measure the local orientation of the LC director field in 3D by observing fluctuations within the sample. Lastly, I found that the regions of opposite ET handedness meet to form heterochiral point defects. Thus, understanding the effects of surface elasticity on bulk deformation is essential for use of LCLC in applications.

A final and qualitatively different experiment with SSY found that the concentration-dependent phase behavior of SSY produces unusual drying and deposition phenomena when drops of SSY solution evaporate on a substrate. As water evaporates from the drop solution, the increasing concentration leads to phase separation, viscosity, and surface tension gradients that create circular flows in the opposite direction to those normally found in Marangoni eddies created in surfactant solutions. Additionally, the final deposited LCLC material on the slide is different from usual coffee-ring shapes and depends strongly on the evaporation rate and initial concentration of SSY. At faster evaporation rates and higher initial concentration the SSY material deposits tends to form more of a “volcano” shape. Since LCLC forming materials are common among many dyes, drugs, and biological molecules, the patterns created during the drying of SSY are representative of what can happen in a wide range of similar systems.

Recent results, concurrent with my writing of this dissertation, have made strides toward engineering applications of LCLCs by modifying their underlying chemistry [271] and by learning about their anchoring energies on treated surfaces [272]. Applying these new methods to the experiments/systems described in this dissertation could result in exciting new applications or the ability to probe features of LCLC mesophases with greater care. I describe some of these possibilities in the subsections below.

### **6.1.1 Surface Chemistry and Elastic Effects**

As mentioned in section 3.5, I have found evidence that surface chemistry can in principle exhibit effects that mimic the saddle-splay elastic term found in the Frank free energy for

nematics. If indeed the surface chemistry modification changes the effective saddle-splay modulus, this phenomena should also be present in thermotropic liquid crystals (TLC) such as 5CB. This ability to chemically alter the effective saddle-splay suggests a new method to control the boundary conditions in all nematic liquid crystals. Typically, controlling director orientation at a surface with planar boundary conditions involves rubbing the interface [272]. Our work indicates that, with the right chemical modification and a slight surface curvature, a preferred orientation for the director could be achieved without surface rubbing. Further, a surface chemistry effect may explain the highly variable measurements of the saddle-splay over the years, even among a single LC species [33]. However, it is difficult to imagine the physical mechanism that would create a local (molecular) chemical effect that can sense a radius of curvature of 100  $\mu\text{m}$  or more. Regardless, I have measured an effective  $K_{24}$  and this issue is likely present in other measurements of  $K_{24}$  as well.

### 6.1.2 Origins of Giant Elastic Anisotropy

One of the most striking features of the LCLC nematic phase is their relatively low value of the twist elastic moduli compared to the splay and bend moduli. This unusual feature of both SSY and disodium cromoglycate (DSCG) is responsible for many of the effects observed in this dissertation [20, 21]. An alternative framing of this unusual feature suggests instead that the splay and bend elastic moduli are relatively large. Splay and bend deformations in an LCLC both likely induce some breakage of the mesogens particularly near defects as discussed below in section 6.1.3. The energetic competition between the elastic deformation and breaking of the mesogen molecular stacks could result in higher valued elastic moduli; a complete understanding of these effects would require extending models such as those found in Refs. [273–275].

Perhaps a clue to these phenomena may come from previous studies of discotic liquid crystals, which have found experimentally, numerically and theoretically that in these systems the usual ordering of the elastic moduli is reversed, *i.e.*  $K_2 > K_1 \gtrsim K_3$  [22–24, 276–278]. In rod-like nematic systems, the twist elastic modulus is typically the smallest of the

moduli, but not to the extent found in LCLCs. Stroobants, Lekkerkerker, and Odijk found that polyelectrolytes and ions in nematic liquid crystals can induce an unusual twisting effects too [279]. Thus, the ionic charges and high ion density in SSY and DSCG solutions may play a role in their unusual elastic properties. One possibility for future experiment would be to design an anionic version of the SSY and DSCG molecules and test their elastic constants. Another option might be to use an ion exchange resin to try to remove some of the excess ions in the nematic phase that are not directly associated with the molecular stacks [221] and then test their elastic constants.

### 6.1.3 LCLC Mesogen Structure Near Defects

The recent advance in LCLC chemistry by Kularatne et al. [271] provides an opportunity to probe directly at a defect by cross-linking a director configuration in place. For example, a nematic LCLC sample could be prepared, quenched and crosslinked to lock in defects to a bulk system. Then by cutting open the resulting solid with a locked in director field, one could examine the microscopic structure by electron or atomic force microscopy. A similar technique in a thermotropic liquid crystal, combined with scanning electron microscopy, has enabled direct mapping of the director field and its study near defects [280]. Unlike traditional nematic liquid crystals, LCLC mesogens can also fracture and shorten when highly deformed as can happen near topological defects. Understanding the role this phenomena plays in affecting the structure of LCLC director fields in nematics involves higher order terms, in either the Landau-De Gennes or Frank theories, because it would directly couple the order parameter to the typical elastic moduli terms. It may be possible to inspect defect structure by using a fluctuation method similar to that used in section 3.3.1. For instance, near defects in capillaries, I noticed that thermal fluctuations of the birefringence appeared more intense. These fluctuations can be used to measure the local variability in the order parameter, which is also coupled to the birefringence.

#### 6.1.4 LCLC Optical Guiding

Nematic lyotropic chromonic liquid crystals, such as SSY and DSCG, have a negative birefringence, or in other words  $\Delta n = n_e - n_o < 0$ . For prolate uniaxial nematics, the ordinary index of refraction,  $n_o$ , is the index of refraction for light with polarization perpendicular to the long axis of the mesogens. In LCLCs,  $n_o > n_e$ ; this means the index of refraction for light polarized along the assembled stacks of molecules is greater than in the plane of the stacks. This characteristic offers an interesting result for the index of refraction gradient in a cylindrical capillary confinement for both homeotropic and planar anchoring scenarios. That is, for light polarized perpendicular to the capillary axis, the twisted escaped radial (TER) configuration and escaped twisted (ET) configuration both have a higher index of refraction at the capillary center than at the capillary boundaries and thus provide a possibility for wave-guiding. Similar liquid crystal systems have been studied before, but the twisted configurations found in capillary confined LCLCs add an interesting *twist* to this classic problem [281, 282].

## 6.2 Summary of and Future Experiments with Disordered Colloidal Glasses

The experiments and analysis I performed in soft disordered colloidal glasses set about probing the fundamental question: what is the relationship between structure and dynamics of the constituent particles? I found, via a machine learning algorithm, that the local packing structure of particles (caging) is predictive of those particles' dynamics, and the relationship between structure and dynamics provides an interesting theoretical insight into the nature of heterogeneous dynamics in glassy materials. The various local caging structures that confine particle movements produced a distribution of activation energies of the confined particles. The energy barriers of these different cages were, in turn, deduced by applying Kramers reaction rate theory to the exponentially distributed residence times that the particles experience within their cages. This apparent relationship between softness

and residence time seems like a promising new direction for identifying the disordered solid equivalent of flow defects in crystalline materials.

### 6.2.1 Bridging Softness and Ensemble Properties in Disordered Colloidal Glasses

Because local structural features can predict residence times and activation heterogeneity, it may be possible to explicitly connect softness to other average properties such as the self-overlap function, mean square displacement, and dynamic heterogeneity ( $\chi_4$ ). In addition to predicting residence times between rearrangements, it may also be possible to predict displacements during rearrangements. These ensemble measures are key tests of many theories of the glass transition that assume homogeneous structure of the underlying particles. Bridging properties of the underlying structural heterogeneity with ensemble measured properties, especially those that can be measured in metallic glasses or other atomic and molecular glasses, would represent a significant advance in understanding the bulk properties of these materials. By tuning the underlying structure's constituents, the bulk properties could then be tuned in a predictable way.

I also began to examine what local features of particle cages are most predictive of the softness and residence time. I found that the presence of small particles nearby was a major signifier of particle softness and the likelihood of rearrangements. This same feature was apparent in determining the softness of both small and large particles and is most pronounced within the first shell of surrounding particles. Better understanding of the exact features that cause greater softness may assist in selecting particle types and ratios to design disordered solid materials with varying fragility.

It may also be possible to detect aging by measuring the evolution of particle softness values. Particle dynamics in glasses slow over long time scales [283–285], *e.g.*, residence times between rearrangements can grow. Softness and perhaps changes in the softness value between rearrangements may give microscopic clues to the physical processes that result in aging phenomena. There are several possible routes to this in a colloidal system.

For example, colloidal samples, like those in my dissertation, age naturally thus “simply” observing a sample for a very extended period may reveal aging. Alternatively, it may be possible to heat and rapidly quench a sample while recording particle dynamics on a microscope.

### **6.2.2 Predicting Fracture in Sheared or Thermally Shocked Colloidal Glass**

By identifying the softer cages, those with shorter residence times, I may be able to predict flow defects wherein non-affine, plastic, rearrangements will occur in sheared disordered solids. After training an SVM and identifying soft spots in a particle packing, it would be interesting to see if shear as in Ref. [270], or thermal shock as in Ref. [242] induced rearrangements in the softest areas first. These experiments would offer a test of how the presence of structure can determine flow defects in a disordered solid.

# Bibliography

- [1] J. Jeong, Z. S. Davidson, P. J. Collings, T. C. Lubensky, and A. G. Yodh, PNAS **111**, 1742 (2014).
- [2] J. Jeong, L. Kang, Z. S. Davidson, P. J. Collings, T. C. Lubensky, and A. G. Yodh, PNAS , 201423220 (2015).
- [3] Z. S. Davidson, L. Kang, J. Jeong, T. Still, P. J. Collings, T. C. Lubensky, and A. G. Yodh, Phys. Rev. E **91**, 050501 (2015).
- [4] M. A. Lohr, T. Still, R. Ganti, M. D. Gratale, Z. S. Davidson, K. B. Aptowicz, C. P. Goodrich, D. M. Sussman, and A. G. Yodh, Phys. Rev. E **90**, 062305 (2014).
- [5] M. D. Gratale, X. Ma, Z. S. Davidson, T. Still, P. Habdas, and A. G. Yodh, Phys. Rev. E **94**, 042606 (2016).
- [6] M. D. Gratale, T. Still, C. Matyas, Z. S. Davidson, S. Lobel, P. J. Collings, and A. G. Yodh, Phys. Rev. E **93**, 050601 (2016).
- [7] T. Still, P. J. Yunker, K. Hanson, Z. S. Davidson, M. A. Lohr, K. B. Aptowicz, and A. G. Yodh, Adv. Mater. Interfaces **2**, n/a (2015).
- [8] P. G. de Gennes, J. Prost, and R. Pelcovits, Physics Today **48**, 70 (1995).
- [9] P. Oswald and P. Pieranski, *Smectic and Columnar Liquid Crystals: Concepts and Physical Properties Illustrated by Experiments* (CRC Press, 2005).

- [10] H.-S. Park and O. D. Lavrentovich, in *Liquid Crystals Beyond Displays: Chemistry, Physics, and Applications*, edited by Q. Li (John Wiley & Sons, Hoboken, N.J., 2012) p. 449.
- [11] F. Reinitzer, *Monatshefte für Chemie* **9**, 421 (1888).
- [12] G. J. T. Tiddy, *Physics Reports* **57**, 1 (1980).
- [13] Z. Dogic and S. Fraden, *Philosophical Transactions of the Royal Society of London A: Mathematical, Physical and Engineering Sciences* **359**, 997 (2001).
- [14] A. Modlińska, A. M. Alsayed, and T. Gibaud, *Scientific Reports* **5**, 18432 (2015).
- [15] C. Zakri, C. Blanc, E. Grelet, C. Zamora-Ledezma, N. Puech, E. Anglaret, and P. Poulin, *Philosophical Transactions of the Royal Society of London A: Mathematical, Physical and Engineering Sciences* **371**, 20120499 (2013).
- [16] M. U. Araos and G. G. Warr, *J. Phys. Chem. B* **109**, 14275 (2005).
- [17] P. V. Braun, P. Osenar, V. Tohver, S. B. Kennedy, and S. I. Stupp, *Journal of the American Chemical Society* **121**, 7302 (1999).
- [18] G. Scalia, C. von Bühler, C. Hägele, S. Roth, F. Giesselmann, and J. P. F. Lagerwall, *Soft Matter* **4**, 570 (2008).
- [19] J. Lydon, *Liquid Crystals Today* **16**, 13 (2007).
- [20] S. Zhou, Y. A. Nastishin, M. M. Omelchenko, L. Tortora, V. G. Nazarenko, O. P. Boiko, T. Ostapenko, T. Hu, C. C. Almasan, S. N. Sprunt, J. T. Gleeson, and O. D. Lavrentovich, *Phys. Rev. Lett.* **109**, 037801 (2012).
- [21] S. Zhou, K. Neupane, Y. A. Nastishin, A. R. Baldwin, S. V. Shiyankovskii, O. D. Lavrentovich, and S. Sprunt, *Soft Matter* **10**, 6571 (2014).
- [22] A. P. Singh and A. D. Rey, *Journal of Non-Newtonian Fluid Mechanics* **94**, 87 (2000).

- [23] T. Sato and A. Teramoto, *Macromolecules* **29**, 4107 (1996).
- [24] P. G. D. Gennes, *Molecular Crystals and Liquid Crystals* **34**, 177 (1976).
- [25] S. Sivakumar, K. L. Wark, J. K. Gupta, N. L. Abbott, and F. Caruso, *Adv. Funct. Mater.* **19**, 2260 (2009).
- [26] I.-H. Lin, D. S. Miller, P. J. Bertics, C. J. Murphy, J. J. de Pablo, and N. L. Abbott, *Science* **332**, 1297 (2011).
- [27] M. Humar and I. Mušević, *Opt. Express*, OE **18**, 26995 (2010).
- [28] G. P. Crawford and S. Žumer, *Int. J. Mod. Phys. B* **09**, 2469 (1995).
- [29] R. D. Polak, G. P. Crawford, B. C. Kostival, J. W. Doane, and S. Žumer, *Phys. Rev. E* **49**, R978 (1994).
- [30] J. C. Knight, *Nature* **424**, 847 (2003).
- [31] K. Nayani, R. Chang, J. Fu, P. W. Ellis, A. Fernandez-Nieves, J. O. Park, and M. Srinivasarao, *Nature Communications* **6**, 8067 (2015).
- [32] N. V. Madhusudana and R. Pratibha, *Molecular Crystals and Liquid Crystals* **89**, 249 (1982).
- [33] A. A. Joshi, J. K. Whitmer, O. Guzmán, N. L. Abbott, and J. J. de Pablo, *Soft Matter* **10**, 882 (2014).
- [34] M. Nakata, G. Zanchetta, B. D. Chapman, C. D. Jones, J. O. Cross, R. Pindak, T. Bellini, and N. A. Clark, *Science* **318**, 1276 (2007).
- [35] J. Lydon, *J. Mater. Chem.* **20**, 10071 (2010).
- [36] S.-W. Tam-Chang and L. Huang, *Chem. Commun.* , 1957 (2008).
- [37] P. J. Collings, A. J. Dickinson, and E. C. Smith, *Liquid Crystals* **37**, 701 (2010).

- [38] V. R. Horowitz, L. A. Janowitz, A. L. Modic, P. A. Heiney, and P. J. Collings, *Phys. Rev. E* **72**, 041710 (2005).
- [39] C. K. McGinn, L. I. Laderman, N. Zimmermann, H.-S. Kitzerow, and P. J. Collings, *Phys. Rev. E* **88**, 062513 (2013).
- [40] H.-S. Park, S.-W. Kang, L. Tortora, Y. Nastishin, D. Finotello, S. Kumar, and O. D. Lavrentovich, *J. Phys. Chem. B* **112**, 16307 (2008).
- [41] P. Chaudhari, A. Levi, and P. Steinhardt, *Phys. Rev. Lett.* **43**, 1517 (1979).
- [42] J. J. Gilman, *Journal of Applied Physics* **46**, 1625 (1975).
- [43] G. Parisi and F. Zamponi, *Rev. Mod. Phys.* **82**, 789 (2010).
- [44] L. Berthier, *Dynamical Heterogeneities in Glasses, Colloids, and Granular Media* (OUP Oxford, 2011) google-Books-ID: n2Kn2Xx9rU8C.
- [45] M. L. Falk and J. S. Langer, *Phys. Rev. E* **57**, 7192 (1998).
- [46] E. R. Weeks and D. A. Weitz, *Phys. Rev. Lett.* **89**, 095704 (2002).
- [47] P. Schall, D. A. Weitz, and F. Spaepen, *Science* **318**, 1895 (2007).
- [48] A. M. Alsayed, M. F. Islam, J. Zhang, P. J. Collings, and A. G. Yodh, *Science* **309**, 1207 (2005).
- [49] A. S. Argon, *Acta Metallurgica* **27**, 47 (1979).
- [50] A. S. Argon and H. Y. Kuo, *Materials Science and Engineering* **39**, 101 (1979).
- [51] K. Chen, T. Still, S. Schoenholz, K. B. Aptowicz, M. Schindler, A. C. Maggs, A. J. Liu, and A. G. Yodh, *Phys. Rev. E* **88**, 022315 (2013).
- [52] R. Candelier, A. Widmer-Cooper, J. K. Kummerfeld, O. Dauchot, G. Biroli, P. Harrowell, and D. R. Reichman, *Phys. Rev. Lett.* **105**, 135702 (2010).

- [53] G. M. Hocky and D. R. Reichman, *The Journal of Chemical Physics* **138**, 12A537 (2013).
- [54] K. Chen, M. L. Manning, P. J. Yunker, W. G. Ellenbroek, Z. Zhang, A. J. Liu, and A. G. Yodh, *Phys. Rev. Lett.* **107**, 108301 (2011).
- [55] A. Widmer-Cooper, P. Harrowell, and H. Fynewever, *Phys. Rev. Lett.* **93**, 135701 (2004).
- [56] R. L. Jack, A. J. Dunleavy, and C. P. Royall, *Phys. Rev. Lett.* **113**, 095703 (2014).
- [57] E. D. Cubuk, S. S. Schoenholz, J. M. Rieser, B. D. Malone, J. Rottler, D. J. Durian, E. Kaxiras, and A. J. Liu, *Phys. Rev. Lett.* **114**, 108001 (2015).
- [58] S. S. Schoenholz, E. D. Cubuk, D. M. Sussman, E. Kaxiras, and A. J. Liu, *Nat Phys* **12**, 469 (2016).
- [59] T. Still, K. Chen, A. M. Alsayed, K. B. Aptowicz, and A. G. Yodh, *Journal of Colloid and Interface Science* **405**, 96 (2013).
- [60] S. Pakhomov, R. P. Hammer, B. K. Mishra, and B. N. Thomas, *PNAS* **100**, 3040 (2003).
- [61] L. Pérez-García and D. B. Amabilino, *Chem. Soc. Rev.* **36**, 941 (2007).
- [62] L. E. Hough, M. Spannuth, M. Nakata, D. A. Coleman, C. D. Jones, G. Dantlgraber, C. Tschierske, J. Watanabe, E. Körblová, D. M. Walba, J. E. MacLennan, M. A. Glaser, and N. A. Clark, *Science* **325**, 452 (2009).
- [63] M. M. Green, N. C. Peterson, T. Sato, A. Teramoto, R. Cook, and S. Lifson, *Science* **268**, 1860 (1995).
- [64] M. M. Green and V. Jain, *Orig Life Evol Biosph* **40**, 111 (2010).
- [65] Y. Hatwalne and M. Muthukumar, *Phys. Rev. Lett.* **105**, 107801 (2010).

- [66] R. Viswanathan, J. A. Zasadzinski, and D. K. Schwartz, *Nature* **368**, 440 (1994).
- [67] A. John McKinnon and D. P. Harland, *Journal of Structural Biology* **173**, 229 (2011).
- [68] J. Pang and N. A. Clark, *Phys. Rev. Lett.* **73**, 2332 (1994).
- [69] L. E. Hough, H. T. Jung, D. Krüerke, M. S. Heberling, M. Nakata, C. D. Jones, D. Chen, D. R. Link, J. Zasadzinski, G. Heppke, J. P. Rabe, W. Stocker, E. Körblova, D. M. Walba, M. A. Glaser, and N. A. Clark, *Science* **325**, 456 (2009).
- [70] D. R. Link, G. Natale, R. Shao, J. E. MacLennan, N. A. Clark, E. Körblova, and D. M. Walba, *Science* **278**, 1924 (1997).
- [71] X. Qiu, J. Ruiz-Garcia, K. J. Stine, C. M. Knobler, and J. V. Selinger, *Phys. Rev. Lett.* **67**, 703 (1991).
- [72] C. J. Eckhardt, N. M. Peachey, D. R. Swanson, J. M. Takacs, M. A. Khan, X. Gong, J.-H. Kim, J. Wang, and R. A. Uphaus, *Nature* **362**, 614 (1993).
- [73] J. V. Selinger, Z.-G. Wang, R. F. Bruinsma, and C. M. Knobler, *Phys. Rev. Lett.* **70**, 1139 (1993).
- [74] E. Hendry, T. Carpy, J. Johnston, M. Popland, R. V. Mikhaylovskiy, A. J. Laphorn, S. M. Kelly, L. D. Barron, N. Gadegaard, and M. Kadodwala, *Nat Nano* **5**, 783 (2010).
- [75] T. Ohzono, T. Yamamoto, and J.-i. Fukuda, *Nature Communications* **5**, 3735 (2014).
- [76] C. M. Soukoulis and M. Wegener, *Nat Photon* **5**, 523 (2011).
- [77] S. Zhang, Y.-S. Park, J. Li, X. Lu, W. Zhang, and X. Zhang, *Phys. Rev. Lett.* **102**, 023901 (2009).
- [78] S. Vignolini, N. A. Yufa, P. S. Cunha, S. Guldin, I. Rushkin, M. Stefik, K. Hur, U. Wiesner, J. J. Baumberg, and U. Steiner, *Adv. Mater.* **24**, OP23 (2012).

- [79] S. H. Kang, S. Shan, W. L. Noorduin, M. Khan, J. Aizenberg, and K. Bertoldi, *Adv. Mater.* **25**, 3380 (2013).
- [80] M. M. Green, M. P. Reidy, R. D. Johnson, G. Darling, D. J. O’Leary, and G. Willson, *J. Am. Chem. Soc.* **111**, 6452 (1989).
- [81] L. Brunsveld, J. a. J. M. Vekemans, J. H. K. K. Hirschberg, R. P. Sijbesma, and E. W. Meijer, *PNAS* **99**, 4977 (2002).
- [82] D. Zerrouki, J. Baudry, D. Pine, P. Chaikin, and J. Bibette, *Nature* **455**, 380 (2008).
- [83] M. A. Lohr, A. M. Alsayed, B. G. Chen, Z. Zhang, R. D. Kamien, and A. G. Yodh, *Phys. Rev. E* **81**, 040401 (2010).
- [84] G. Wu, Y. Xia, and S. Yang, *Soft Matter* **10**, 1392 (2014).
- [85] S. H. Kang, S. Shan, A. Košmrlj, W. L. Noorduin, S. Shian, J. C. Weaver, D. R. Clarke, and K. Bertoldi, *Phys. Rev. Lett.* **112**, 098701 (2014).
- [86] Y. Snir and R. D. Kamien, *Science* **307**, 1067 (2005).
- [87] B. Pokroy, S. H. Kang, L. Mahadevan, and J. Aizenberg, *Science* **323**, 237 (2009).
- [88] F. Lonberg and R. B. Meyer, *Phys. Rev. Lett.* **55**, 718 (1985).
- [89] R. Williams, *Phys. Rev. Lett.* **21**, 342 (1968).
- [90] O. D. Lavrentovich, *Phys. Rev. A* **46**, R722 (1992).
- [91] O. D. Lavrentovich and E. M. Terentjev, *JETP* **64**, 1237 (1986).
- [92] D.-K. Yang, K.-U. Jeong, and S. Z. D. Cheng, *J. Phys. Chem. B* **112**, 1358 (2008).
- [93] G. Volovik and O. Lavrentovich, *Journal of Experimental and Theoretical Physics* **58**, 1159 (1983).
- [94] R. D. Williams, *J. Phys. A: Math. Gen.* **19**, 3211 (1986).

- [95] O. D. Lavrentovich and V. V. Sergan, *Il Nuovo Cimento D* **12**, 1219 (1990).
- [96] L. Tortora and O. D. Lavrentovich, *PNAS* **108**, 5163 (2011).
- [97] P. Prinsen and P. van der Schoot, *Phys. Rev. E* **68**, 021701 (2003).
- [98] P. Prinsen and P. van der Schoot, *J. Phys.: Condens. Matter* **16**, 8835 (2004).
- [99] M. J. Press and A. S. Arrott, *Phys. Rev. Lett.* **33**, 403 (1974).
- [100] L. Tortora, H.-S. Park, S.-W. Kang, V. Savaryn, S.-H. Hong, K. Kaznatcheev, D. Finotello, S. Sprunt, S. Kumar, and O. D. Lavrentovich, *Soft Matter* **6**, 4157 (2010).
- [101] E. Pairam, J. Vallamkondu, V. Koning, B. C. van Zuiden, P. W. Ellis, M. A. Bates, V. Vitelli, and A. Fernandez-Nieves, *PNAS* **110**, 9295 (2013).
- [102] V. Koning, B. C. van Zuiden, R. D. Kamien, and V. Vitelli, *Soft Matter* **10**, 4192 (2014).
- [103] O. D. Lavrentovich and V. M. Pergamenschik, *Molecular Crystals and Liquid Crystals Incorporating Nonlinear Optics* **179**, 125 (1990).
- [104] P. S. Drzaic and T. J. Scheffer, *Journal of the Society for Information Display* **5**, 413 (1997).
- [105] C. Williams and Y. Bouligand, *J. Phys. France* **35**, 589 (1974).
- [106] J. Lydon, *Liquid Crystals* **38**, 1663 (2011).
- [107] P. Mariani and L. Saturni, *Biophysical Journal* **70**, 2867 (1996).
- [108] Y. A. Nastishin, H. Liu, T. Schneider, V. Nazarenko, R. Vasyuta, S. V. Shiyankovskii, and O. D. Lavrentovich, *Phys. Rev. E* **72**, 041711 (2005).
- [109] A. F. Kostko, B. H. Cipriano, O. A. Pinchuk, L. Ziserman, M. A. Anisimov, D. Danino, and S. R. Raghavan, *J. Phys. Chem. B* **109**, 19126 (2005).

- [110] D. J. Edwards, J. W. Jones, O. Lozman, A. P. Ormerod, M. Sinyureva, and G. J. T. Tiddy, *J. Phys. Chem. B* **112**, 14628 (2008).
- [111] H.-S. Park, S.-W. Kang, L. Tortora, S. Kumar, and O. D. Lavrentovich, *Langmuir* **27**, 4164 (2011).
- [112] Y. A. Nastishin, K. Neupane, A. R. Baldwin, O. D. Lavrentovich, and S. Sprunt, arXiv:0807.2669 [cond-mat] (2008), arXiv:0807.2669 [cond-mat] .
- [113] R. C. Jones, *Journal of the Optical Society of America* **31**, 488 (1941).
- [114] J. Ding and Y. Yang, *Japanese Journal of Applied Physics* **31**, 2837 (1992).
- [115] F. Xu, H.-S. Kitzerow, and P. P. Crooker, *Phys. Rev. E* **49**, 3061 (1994).
- [116] L. Kang, Dissertations available from ProQuest , 1 (2015).
- [117] J. H. Erdmann, S. Žumer, and J. W. Doane, *Phys. Rev. Lett.* **64**, 1907 (1990).
- [118] P. Poulin, H. Stark, T. C. Lubensky, and D. A. Weitz, *Science* **275**, 1770 (1997).
- [119] O. D. Lavrentovich, *Liquid Crystals* **24**, 117 (1998).
- [120] A. Fernández-Nieves, V. Vitelli, A. S. Utada, D. R. Link, M. Márquez, D. R. Nelson, and D. A. Weitz, *Phys. Rev. Lett.* **99**, 157801 (2007).
- [121] J. Gupta, S. Sivakumar, F. Caruso, and N. Abbott, *Angewandte Chemie International Edition* **48**, 1652 (2009).
- [122] T. Lopez-Leon and A. Fernandez-Nieves, *Colloid Polym Sci* **289**, 345 (2011).
- [123] T. Lopez-Leon, V. Koning, K. B. S. Devaiah, V. Vitelli, and A. Fernandez-Nieves, *Nat Phys* **7**, 391 (2011).
- [124] J. Jeong and M. W. Kim, *Phys. Rev. Lett.* **108**, 207802 (2012).
- [125] B. Senyuk, Q. Liu, S. He, R. D. Kamien, R. B. Kusner, T. C. Lubensky, and I. I. Smalyukh, *Nature* **493**, 200 (2013).

- [126] J. W. Doane, N. A. Vaz, B.-G. Wu, and S. Žumer, *Appl. Phys. Lett.* **48**, 269 (1986).
- [127] K. A. Simon, P. Sejwal, R. B. Gerecht, and Y.-Y. Luk, *Langmuir* **23**, 1453 (2007).
- [128] K. A. Simon, P. Sejwal, E. R. Falcone, E. A. Burton, S. Yang, D. Prashar, D. Bandyopadhyay, S. K. Narasimhan, N. Varghese, N. S. Gobalasingham, J. B. Reese, and Y.-Y. Luk, *J. Phys. Chem. B* **114**, 10357 (2010).
- [129] F. Xu and P. P. Crooker, *Phys. Rev. E* **56**, 6853 (1997).
- [130] P. Yeh and C. Gu, *Optics of Liquid Crystal Displays* (John Wiley & Sons, 2010).
- [131] P. S. Drzaic, *Liquid Crystals* **26**, 623 (1999).
- [132] A. A. Verhoeff and H. N. W. Lekkerkerker, *Soft Matter* **8**, 4865 (2012).
- [133] M. Kleman, *J. Phys. France* **41**, 737 (1980).
- [134] S. Chandrasekhar, *Molecular Crystals* **2**, 71 (1966).
- [135] C. Rottman and M. Wortis, *Physics Reports* **103**, 59 (1984).
- [136] R. K. Shah, H. C. Shum, A. C. Rowat, D. Lee, J. J. Agresti, A. S. Utada, L.-Y. Chu, J.-W. Kim, A. Fernandez-Nieves, C. J. Martinez, and D. A. Weitz, *Materials Today* **11**, 18 (2008).
- [137] A. J. Dickinson, N. D. LaRacuenta, C. B. McKitterick, and P. J. Collings, *Molecular Crystals and Liquid Crystals* **509**, 9/[751] (2009).
- [138] D. Goldfarb, Z. Luz, N. Spielberg, and H. Zimmermann, *Molecular Crystals and Liquid Crystals* **126**, 225 (1985).
- [139] D. M. Agra-Kooijman, G. Singh, A. Lorenz, P. J. Collings, H.-S. Kitzerow, and S. Kumar, *Phys. Rev. E* **89**, 062504 (2014).
- [140] R. Ondris-Crawford, G. Crawford, S. Zumer, and J. Doane, *Physical Review Letters* **70**, 194 (1993).

- [141] H.-S. Kitzerow, B. Liu, F. Xu, and P. P. Crooker, *Phys. Rev. E* **54**, 568 (1996).
- [142] M. Ambrožič and S. Žumer, *Phys. Rev. E* **59**, 4153 (1999).
- [143] M. Ambrožič and S. Žumer, *Phys. Rev. E* **54**, 5187 (1996).
- [144] P. E. Cladis, A. E. White, and W. F. Brinkman, *J. Phys. France* **40**, 325 (1979).
- [145] J. Jeong, G. Han, A. T. C. Johnson, P. J. Collings, T. C. Lubensky, and A. G. Yodh, *Langmuir* **30**, 2914 (2014).
- [146] S. Zhou, A. Sokolov, O. D. Lavrentovich, and I. S. Aranson, *PNAS* **111**, 1265 (2014).
- [147] P. C. Mushenheim, R. R. Trivedi, H. H. Tuson, D. B. Weibel, and N. L. Abbott, *Soft Matter* **10**, 88 (2013).
- [148] P. E. Cladis and M. Kléman, *J. Phys. France* **33**, 591 (1972).
- [149] C. Williams, P. Pierański, and P. E. Cladis, *Phys. Rev. Lett.* **29**, 90 (1972).
- [150] R. B. Meyer, *Philosophical Magazine* **27**, 405 (1973).
- [151] D. Melzer and F. R. N. Nabarro, *Philosophical Magazine* **35**, 901 (1977).
- [152] P. E. Cladis, *Philosophical Magazine* **29**, 641 (1974).
- [153] I. Vilfan, M. Vilfan, and S. Žumer, *Phys. Rev. A* **43**, 6875 (1991).
- [154] G. P. Crawford, D. W. Allender, and J. W. Doane, *Phys. Rev. A* **45**, 8693 (1992).
- [155] D. Allender, G. Crawford, and J. Doane, *Physical Review Letters* **67**, 1442 (1991).
- [156] J. M. Ribó, J. Crusats, F. Sagués, J. Claret, and R. Rubires, *Science* **292**, 2063 (2001).
- [157] N. Petit-Garrido, J. Ignés-Mullol, J. Claret, and F. Sagués, *Phys. Rev. Lett.* **103**, 237802 (2009).
- [158] M. Schadt and W. Helfrich, *Applied Physics Letters* **18**, 127 (1971).

- [159] M. Škarabot, M. Ravnik, S. Žumer, U. Tkalec, I. Poberaj, D. Babič, and I. Muševič, *Phys. Rev. E* **77**, 061706 (2008).
- [160] L. Rao, Z. Ge, S.-T. Wu, and S. H. Lee, *Applied Physics Letters* **95**, 231101 (2009).
- [161] T. Gibaud, E. Barry, M. J. Zakhary, M. Henglin, A. Ward, Y. Yang, C. Berciu, R. Oldenbourg, M. F. Hagan, D. Nicastro, R. B. Meyer, and Z. Dogic, *Nature* **481**, 348 (2012).
- [162] C. Jones, in *Handbook of Visual Display Technology*, edited by J. Chen, W. Cranton, and M. Fihn (Springer Berlin Heidelberg, 2012) pp. 1507–1543.
- [163] H. Hakemi, E. F. Jagodzinski, and D. B. DuPré, *J.Chem.Phys.* **78**, 1513 (1983).
- [164] F. Giavazzi, S. Crotti, A. Speciale, F. F. Serra, G. Zanchetta, V. Trappe, M. Buscaglia, T. Bellini, and R. Cerbino, *Soft Matter* (2014), 10.1039/C4SM00145A.
- [165] A. Sparavigna, O. D. Lavrentovich, and A. Strigazzi, *Phys. Rev. E* **49**, 1344 (1994).
- [166] V. Fréedericksz and V. Zolina, *Trans. Faraday Soc.* **29**, 919 (1933).
- [167] P. P. Karat and N. V. Madhusudana, *Molecular Crystals and Liquid Crystals* **36**, 51 (1976).
- [168] P. P. Karat and N. V. Madhusudana, *Molecular Crystals and Liquid Crystals* **40**, 239 (1977).
- [169] A. Bogi and S. Faetti, *Liquid Crystals* **28**, 729 (2001).
- [170] J. Nehring and A. Saupe, *The Journal of Chemical Physics* **54**, 337 (1971).
- [171] V. H. Schmidt, *Phys. Rev. Lett.* **64**, 535 (1990).
- [172] P. Palffy-Muhoray, *Phys. Rev. Lett.* **65**, 1828 (1990).
- [173] P. G. de Gennes and J. Prost, *The Physics of Liquid Crystals* (Clarendon Press, 1995).

- [174] G. P. Alexander, B. G.-g. Chen, E. A. Matsumoto, and R. D. Kamien, *Rev. Mod. Phys.* **84**, 497 (2012).
- [175] M. Schadt, K. Schmitt, V. Kozinkov, and V. Chigrinov, *Jpn. J. Appl. Phys.* **31**, 2155 (1992).
- [176] V. G. Nazarenko, O. P. Boiko, H.-S. Park, O. M. Brodyn, M. M. Omelchenko, L. Tortora, Y. A. Nastishin, and O. D. Lavrentovich, *Phys. Rev. Lett.* **105**, 017801 (2010).
- [177] N. Zimmerman, G. Jünnemann-Held, P. Collings, and H. Kitzrow, *Soft Matter* (2015), 10.1039/C4SM02579B.
- [178] B.-w. Lee and N. A. Clark, *Science* **291**, 2576 (2001).
- [179] E. Willman, L. Seddon, M. Osman, A. Bulak, R. James, S. E. Day, and F. A. Fernandez, *Phys. Rev. E* **89**, 052501 (2014).
- [180] Z. S. Davidson, L. Kang, J. Jeong, T. Still, P. J. Collings, T. C. Lubensky, and A. G. Yodh, *Phys. Rev. E* **92**, 019905 (2015).
- [181] J. L. Ericksen, *Physics of Fluids* **9**, 1205 (1966).
- [182] Z. Davidson, J. Jeong, M. Lohr, P. Collings, T. Lubensky, and A. Yodh, *Bull.Am.Phys.Soc.* **59** (2014).
- [183] Z. S. Davidson, J. Jeong, L. Kang, P. J. Collings, T. C. Lubensky, and A. Yodh, *Bull.Am.Phys.Soc.* **60** (2015).
- [184] R. Chang, K. Nayani, J. Fu, E. Reichmanis, J. O. Park, and M. Srinivasarao, *Bull.Am.Phys.Soc.* **60** (2015).
- [185] P. Biscari and E. M. Terentjev, *Phys. Rev. E* **73**, 051706 (2006).
- [186] W. D. Ristenpart, P. G. Kim, C. Domingues, J. Wan, and H. A. Stone, *Physical Review Letters* **99** (2007), 10.1103/PhysRevLett.99.234502.

- [187] P. J. Yunker, T. Still, M. A. Lohr, and A. G. Yodh, *Nature* **476**, 308 (2011).
- [188] T. Kajiya, C. Monteux, T. Narita, F. Lequeux, and M. Doi, *Langmuir* **25**, 6934 (2009).
- [189] A. Crivoi and F. Duan, *Langmuir* **29**, 12067 (2013).
- [190] T. Still, P. J. Yunker, and A. G. Yodh, *Langmuir* **28**, 4984 (2012).
- [191] V. X. Nguyen and K. J. Stebe, *Phys. Rev. Lett.* **88**, 164501 (2002).
- [192] A. P. Sommer and N. Rozlosnik, *Crystal Growth & Design* **5**, 551 (2005).
- [193] L. Cui, J. Zhang, X. Zhang, Y. Li, Z. Wang, H. Gao, T. Wang, S. Zhu, H. Yu, and B. Yang, *Soft Matter* **8**, 10448 (2012).
- [194] J. Z. Wang, Z. H. Zheng, H. W. Li, W. T. S. Huck, and H. Siringhaus, *Nat Mater* **3**, 171 (2004).
- [195] V. Dugas, J. Broutin, and E. Souteyrand, *Langmuir* **21**, 9130 (2005).
- [196] J. R. Trantum, M. L. Baglia, Z. E. Eagleton, R. L. Mernaugh, and F. R. Haselton, *Lab Chip* **14**, 315 (2013).
- [197] X. Yang, C. Y. Li, and Y. Sun, *Soft Matter* **10**, 4458 (2014).
- [198] R. D. Deegan, O. Bakajin, T. F. Dupont, G. Huber, S. R. Nagel, and T. A. Witten, *Phys. Rev. E* **62**, 756 (2000).
- [199] Y. Shimokawa, T. Kajiya, K. Sakai, and M. Doi, *Phys. Rev. E* **84**, 051803 (2011).
- [200] M. Anyfantakis, Z. Geng, M. Morel, S. Rudiuk, and D. Baigl, *Langmuir* **31**, 4113 (2015).
- [201] S. J. Gokhale, J. L. Plawsky, and P. C. Wayner, *Langmuir* **21**, 8188 (2005).
- [202] T. Kajiya, W. Kobayashi, T. Okuzono, and M. Doi, *J. Phys. Chem. B* **113**, 15460 (2009).

- [203] H. Tan, C. Diddens, P. Lv, J. G. M. Kuerten, X. Zhang, and D. Lohse, PNAS **113**, 8642 (2016).
- [204] H. Kim, F. Boulogne, E. Um, I. Jacobi, E. Button, and H. A. Stone, Phys. Rev. Lett. **116**, 124501 (2016).
- [205] D. Kaya, V. A. Belyi, and M. Muthukumar, The Journal of Chemical Physics **133**, 114905 (2010).
- [206] N. Shahidzadeh, M. F. L. Schut, J. Desarnaud, M. Prat, and D. Bonn, Sci. Rep. **5** (2015), 10.1038/srep10335.
- [207] F. Parisse and C. Allain, Journal de Physique II **6**, 1111 (1996).
- [208] R. D. Deegan, O. Bakajin, T. F. Dupont, G. Huber, S. R. Nagel, and T. A. Witten, Nature **389**, 827 (1997).
- [209] T. Kajiyama, D. Kaneko, and M. Doi, Langmuir **24**, 12369 (2008).
- [210] V. R. Dugyala and M. G. Basavaraj, J. Phys. Chem. B **119**, 3860 (2015).
- [211] W. Sempels, R. De Dier, H. Mizuno, J. Hofkens, and J. Vermant, Nat Commun **4**, 1757 (2013).
- [212] H. B. Eral, D. M. Augustine, M. H. G. Duits, and F. Mugele, Soft Matter **7**, 4954 (2011).
- [213] H. Minemawari, T. Yamada, H. Matsui, J. Tsutsumi, S. Haas, R. Chiba, R. Kumai, and T. Hasegawa, Nature **475**, 364 (2011).
- [214] I. I. Smalyukh, O. V. Zribi, J. C. Butler, O. D. Lavrentovich, and G. C. L. Wong, Phys. Rev. Lett. **96**, 177801 (2006).
- [215] S. Zhang, Q. Li, I. A. Kinloch, and A. H. Windle, Langmuir **26**, 2107 (2010).
- [216] J. Park and J. Moon, Langmuir **22**, 3506 (2006).

- [217] T. P. Bigioni, X.-M. Lin, T. T. Nguyen, E. I. Corwin, T. A. Witten, and H. M. Jaeger, *Nat Mater* **5**, 265 (2006).
- [218] T. Bellini, G. Zanchetta, T. P. Fraccia, R. Cerbino, E. Tsai, G. P. Smith, M. J. Moran, D. M. Walba, and N. A. Clark, *PNAS* **109**, 1110 (2012).
- [219] R. Duggal, F. Hussain, and M. Pasquali, *Advanced Materials* **18**, 29 (2006).
- [220] L. Joshi, S.-W. Kang, D. M. Agra-Kooijman, and S. Kumar, *Phys. Rev. E* **80**, 041703 (2009).
- [221] F. Chami and M. R. Wilson, *J. Am. Chem. Soc.* **132**, 7794 (2010).
- [222] F. Li, T. Xu, D.-H. T. Nguyen, X. Huang, C. S. Chen, and C. Zhou, *J. Biomed. Opt* **19**, 016006 (2014).
- [223] S. Manukyan, H. M. Sauer, I. V. Roisman, K. A. Baldwin, D. J. Fairhurst, H. Liang, J. Venzmer, and C. Tropea, *Journal of Colloid and Interface Science* **395**, 287 (2013).
- [224] H. Hu and R. G. Larson, *The Journal of Physical Chemistry B* **106**, 1334 (2002).
- [225] H. Hu and R. G. Larson, *J. Phys. Chem. B* **110**, 7090 (2006).
- [226] P. K. Weissenborn and R. J. Pugh, *Journal of Colloid and Interface Science* **184**, 550 (1996).
- [227] T. Ostapenko, Y. A. Nastishin, P. J. Collings, S. N. Sprunt, O. D. Lavrentovich, and J. T. Gleeson, *Soft Matter* **9**, 9487 (2013).
- [228] Y.-K. Kim, S. V. Shiyankovskii, and O. D. Lavrentovich, *J. Phys.: Condens. Matter* **25**, 404202 (2013).
- [229] F. Livolant and Y. Bouligand, *Journal de Physique* **47**, 1813 (1986).
- [230] W. Xiao, C. Hu, D. J. Carter, S. Nichols, M. D. Ward, P. Raiteri, A. L. Rohl, and B. Kahr, *Crystal Growth & Design* **14**, 4166 (2014).

- [231] Y. Jung, T. Kajiyama, T. Yamaue, and M. Doi, *Jpn. J. Appl. Phys.* **48**, 031502 (2009).
- [232] G. I. Taylor, *Proceedings of the Royal Society of London A: Mathematical, Physical and Engineering Sciences* **145**, 362 (1934).
- [233] N. W. Ashcroft and N. D. Mermin, *Solid State Physics* (Holt, Rinehart and Winston, 1976).
- [234] J. G. Dash, H. Fu, and J. S. Wettlaufer, *Rep. Prog. Phys.* **58**, 115 (1995).
- [235] H. Löwen, *Physics Reports* **237**, 249 (1994).
- [236] C. Kittel, *Introduction to Solid State Physics* (Wiley, 2004) google-Books-ID: kym4QgAACAAJ.
- [237] A. S. Keys, L. O. Hedges, J. P. Garrahan, S. C. Glotzer, and D. Chandler, *Phys. Rev. X* **1**, 021013 (2011).
- [238] M. Goldstein, *The Journal of Chemical Physics* **51**, 3728 (1969).
- [239] L. Berthier and G. Biroli, *Rev. Mod. Phys.* **83**, 587 (2011).
- [240] J.-P. Bouchaud and G. Biroli, *Phys. Rev. B* **72**, 064204 (2005).
- [241] D. Coslovich and G. Pastore, *The Journal of Chemical Physics* **127**, 124504 (2007).
- [242] K. Chen, W. G. Ellenbroek, Z. Zhang, D. T. N. Chen, P. J. Yunker, S. Henkes, C. Brito, O. Dauchot, W. van Saarloos, A. J. Liu, and A. G. Yodh, *Phys. Rev. Lett.* **105**, 025501 (2010).
- [243] S. S. Schoenholz, A. J. Liu, R. A. Riggleman, and J. Rottler, *Phys. Rev. X* **4**, 031014 (2014).
- [244] M. L. Manning and A. J. Liu, *Phys. Rev. Lett.* **107**, 108302 (2011).
- [245] J. Rottler, S. S. Schoenholz, and A. J. Liu, *Phys. Rev. E* **89**, 042304 (2014).
- [246] A. Ghosh, V. Chikkadi, P. Schall, and D. Bonn, *Phys. Rev. Lett.* **107**, 188303 (2011).

- [247] A. Smessaert and J. Rottler, *Soft Matter* **10**, 8533 (2014).
- [248] R. Candelier, O. Dauchot, and G. Biroli, *Phys. Rev. Lett.* **102**, 088001 (2009).
- [249] D. M. Sussman, S. S. Schoenholz, E. D. Cubuk, and A. J. Liu, arXiv:1610.03401 [cond-mat] (2016), arXiv:1610.03401 [cond-mat] .
- [250] E. D. Cubuk, S. S. Schoenholz, E. Kaxiras, and A. J. Liu, *J. Phys. Chem. B* **120**, 6139 (2016).
- [251] C. Patrick Royall, S. R. Williams, T. Ohtsuka, and H. Tanaka, *Nat Mater* **7**, 556 (2008).
- [252] C. P. Royall and S. R. Williams, *Physics Reports The role of local structure in dynamical arrest*, **560**, 1 (2015).
- [253] A. S. de Wijn, D. M. Miedema, B. Nienhuis, and P. Schall, *Phys. Rev. Lett.* **109**, 228001 (2012).
- [254] P. J. Yunker, K. Chen, M. D. Gratale, M. A. Lohr, T. Still, and A. G. Yodh, *Rep. Prog. Phys.* **77**, 056601 (2014).
- [255] J. C. Crocker and D. G. Grier, *Journal of Colloid and Interface Science* **179**, 298 (1996).
- [256] D. Allan, T. Caswell, N. Keim, and C. van der Wel, (2016), 10.5281/zenodo.60550.
- [257] E. R. Weeks, J. C. Crocker, A. C. Levitt, A. Schofield, and D. A. Weitz, *Science* **287**, 627 (2000).
- [258] A. S. Keys, A. R. Abate, S. C. Glotzer, and D. J. Durian, *Nat Phys* **3**, 260 (2007).
- [259] J.-P. Hansen and I. R. McDonald, *Theory of Simple Liquids* (Academic Press, 2006) google-Books-ID: Uhm87WZBnxEC.

- [260] P. Chaudhuri, L. Berthier, S. Sastry, and W. Kob, in *Diffusion Fundamentals III*, edited by C. Chmelik, N. Kanellopoulos, J. Kärger, and D. Theodorou (Leipziger Universitätsverlag, Leipzig, 2009).
- [261] A. Smessaert and J. Rottler, *Phys. Rev. E* **88**, 022314 (2013).
- [262] C. Bishop, *Pattern Recognition and Machine Learning* (Springer, New York, 2007).
- [263] F. Pedregosa, G. Varoquaux, A. Gramfort, V. Michel, B. Thirion, O. Grisel, M. Blondel, P. Prettenhofer, R. Weiss, V. Dubourg, J. Vanderplas, A. Passos, D. Cournapeau, M. Brucher, M. Perrot, and É. Duchesnay, *Journal of Machine Learning Research* **12**, 2825 (2011).
- [264] J. Behler and M. Parrinello, *Phys. Rev. Lett.* **98**, 146401 (2007).
- [265] P. Hänggi, P. Talkner, and M. Borkovec, *Rev. Mod. Phys.* **62**, 251 (1990).
- [266] S. Seabold and J. Perktold (2010) pp. 57–61.
- [267] X.-g. Ma, P.-Y. Lai, and P. Tong, *Soft Matter* **9**, 8826 (2013).
- [268] G. L. Hunter and E. R. Weeks, *Phys. Rev. E* **85**, 031504 (2012).
- [269] X. Du and E. R. Weeks, *Phys. Rev. E* **93**, 062613 (2016).
- [270] N. C. Keim and P. E. Arratia, *Soft Matter* **9**, 6222 (2013).
- [271] R. S. Kularatne, H. Kim, M. Ammanamanchi, H. N. Hayenga, and T. H. Ware, *Chem. Mater.* **28**, 8489 (2016).
- [272] P. J. Collings, P. van der Asdonk, A. Martinez, L. Tortora, and P. H. J. Kouwer, *Liquid Crystals* (2016).
- [273] M. P. Taylor and J. Herzfeld, *MRS Online Proceedings Library Archive* **177** (1989), 10.1557/PROC-177-135.
- [274] M. P. Taylor and J. Herzfeld, *Langmuir* **6**, 911 (1990).

- [275] M. P. Taylor and J. Herzfeld, *Phys. Rev. A* **43**, 1892 (1991).
- [276] J. Stelzer, M. A. Bates, L. Longa, and G. R. Luckhurst, *The Journal of Chemical Physics* **107**, 7483 (1997).
- [277] K. Singh and N. S. Pandey, *Liquid Crystals* **25**, 411 (1998).
- [278] P. A. de Castro, A. J. Palangana, and L. R. Evangelista, *Phys. Rev. E* **60**, 6195 (1999).
- [279] A. Stroobants, H. N. W. Lekkerkerker, and T. Odijk, *Macromolecules* **19**, 2232 (1986).
- [280] Y. Xia, F. Serra, R. D. Kamien, K. J. Stebe, and S. Yang, *PNAS* **112**, 15291 (2015).
- [281] J. A. Reyes and R. F. Rodríguez, *Optics Communications* **134**, 349 (1997).
- [282] K. Peddireddy, V. S. R. Jampani, S. Thutupalli, S. Herminghaus, C. Bahr, and I. Muševič, *Opt. Express*, *OE* **21**, 30233 (2013).
- [283] S. Jabbari-Farouji, D. Mizuno, M. Atakhorrami, F. C. MacKintosh, C. F. Schmidt, E. Eiser, G. H. Wegdam, and D. Bonn, *Phys. Rev. Lett.* **98**, 108302 (2007).
- [284] K. Chen and K. S. Schweizer, *Phys. Rev. Lett.* **98**, 167802 (2007).
- [285] J. M. Lynch, G. C. Cianci, and E. R. Weeks, *Phys. Rev. E* **78**, 031410 (2008).